Saltwater detection and monitoring using metal cased boreholes as long electrodes

vorgelegt von
Diplom Ingenieur (Geophysik)
Mathias Ronczka
geb. in Neuruppin

der Fakultät VI Planen Bauen Umwelt
der Technischen Universität Berlin
zur Erlangung des akademischen Grades

Doktor der Naturwissenschaften
- Dr. rer. nat. -

genehmigte Dissertation

Promotionsausschuss:

Vorsitzender: Prof. G. Franz
Berichter: Prof. U. Yaramanci
Berichter: Prof. A. Binley
Berichter: Dr. T. Günther

Tag der wissenschaftlichen Aussprache: 22.Dezember.2015

Berlin 2016
D83

Abstract

Contaminations of freshwater aquifers by saltwater are a well-known problem in coastal regions, as well as on inland sites. They can be detected by electrical resistivity tomography (ERT) as recent widespread investigations show. The three-dimensional application is limited to small scales due to the enormous effort required by field surveys. This thesis presents an approach that uses the metal casing of boreholes as long electrodes for ERT surveys (LE-ERT) to detect and monitor saltwater intrusions.
Three different approaches for modelling long electrodes exist: The complete electrode model (CEM) and the conductive cell model (CCM) lead to comparable results but are numerically expensive, while the shunt electrode model (SEM) has the lowest numerical effort for the same accuracy.
Simulations reveal that the low vertical model resolution due to long electrodes can be enhanced by using electrodes of different length or additional surface electrodes. Three-dimensional inversion of synthetic data supports this assumption. They also show that varying contact impedances along metal casings are of secondary importance.
Laboratory 2D and 3D experiments were conducted to monitor different scenarios of saltwater intrusions. Optimised data sets showed that dipole combinations with a high geometric factor and low voltage often possess a high information content. Due to their low signal strength, these combinations are difficult to measure and prone to noise. This can be considered by excluding or downweighting data prior to the optimisation process.
Field measurements were conducted on medium- and large-scaled test sites. Reduced data sets were generated to control the effort for the surveys. Inversion results of the medium-scaled site showed good agreement with geology, ERT profiles and in-situ fluid conductivity measurements. LE-ERT monitoring over a period of two years could sufficiently resolve small resistivity changes in the upper aquifer, validated by fluid conductivities. The feasibility of LE-ERT as a large-scale application was proved on a 7×7 km test site. The general vertical resistivity trend is in good agreement with electro-logs of three different boreholes. LE-ERT is an applicable cost-efficient method covering large areas.

Zusammenfassung

Salzwasserintrusionen in Frischwasser führende Aquifere sind sowohl in Küstenregionen, als auch im Landesinneren ein bekanntes Problem. Zur Detektierung können elektrische Verfahren wie ERT (electrical resistivity tomography) eingesetzt werden. Da die 3D Anwendung dieser Methode selbst auf kleinen Skalen enormen Aufwand erfordert, wurde in dieser Arbeit der Ansatz untersucht, stahlverrohrte Bohrlöcher als lange Elektroden für Geoelektrikmessungen (LE-ERT) zu verwenden.
Um lange Elektroden zu diskretisieren, existieren drei Ansätze. Das Complete Electrode Model (CEM) und das Conductive Cell Model (CCM) sind zwei ähnliche Methoden, die vergleichbare Ergebnisse erzielen, jedoch nummerisch aufwändig sind. Das Shunt Electrode Modell (SEM) bietet eine Alternative mit geringem nummerischen Aufwand.
Modellierungen zeigen, dass die vertikale Auflösung erhöht werden kann, indem verschieden lange Elektroden oder zusätzliche Punktelektroden verwendet werden, was durch Auflösungsanalysen unterstützt wird. Simulationen zeigten, dass der Einfluss von Kontaktimpedanzen eine untergeordnete Rolle spielt.
Verschiedene Salzwasserszenarien wurden in 2D/3D Laborexperimenten simuliert. Während der Generierung optimierter Datensätze wurde herausgefunden, dass Kombinationen mit geringer Messspannung und hohem Geometriefaktor einen hohen Informationsgehalt besitzen. Diese müssen aufgrund der schweren messtechnischen Erfassung entweder vor dem Optimierungsprozess ausge-schlossen oder mit einem Fehlermodell gewichtet werden.
Messungen auf mittel- und großskaligen Testfeldern zeigten, dass nur reduzierte Datensätze realisierbar sind. Inversionsergebnisse eines mittelskaligen Testfeldes stimmten mit 2D ERT Profilen, der Geologie und in situ Fluidleitfähigkeiten überein. Ein zweijähriges Monitoring konnte selbst kleine Widerstandsänderungen hinreichend auflösen. Die Machbarkeit von LE-ERT als großskalige Anwendung konnte auf dem zweiten $7 \times 7\,\mathrm{km}$ Testfeld gezeigt werden. Der generelle Widerstandstiefenverlauf stimmt gut mit Elektrologs aus 3 Bohrlöchern überein. LE-ERT ist damit eine Methode, welche auf großen Flächen, wie Brunnenfeldern eingesetzt werden kann.

Contents

1 Introduction

Freshwater aquifers are the main source of drinking water supply in many regions, which has to be protected from different kinds of threat. One well-known problem is saltwater intrusion. They mainly occur at coastal regions, were seawater is the reason for saline contamination. Nevertheless, saltwater intrusions can also appear inland. Widespread investigations on different scales have been done in order to understand saltwater movements and to predict their spreading direction. Recent hydrogeological investigations of Werner et al. (2009) and Shi et al. (2011) analyse the saltwater-freshwater interface. Most hydrogeological measurements like pumping tests and well sampling provide only local information about subsurface conditions. Geophysical methods in contrast can provide information in 2D or even 3D using hydrogeological results as calibration and are able to interpolate between point observations.
Electrical or electromagnetic methods are often the method of choice, since imaging electrical resistivity is an indicator for both clay content and groundwater mineralisation. The spectrum of methods extends from electrical resistivity tomography (ERT) to electromagnetic methods in time and frequency domains. Several examples of large scale geophysical surveys exist trying to delineate the saltwater-freshwater interface. Wiederhold et al. (2013) used multiple geophysical methods including ground-penetrating radar (GPR), ERT, seismics and airborne electromagnetic surveys to characterize the freshwater lens below the island of Borkum. Based on these data sets, Sulzbacher et al. (2012) developed a hydrological model predicting impacts of climate change on the freshwater lens of Borkum. Particularly, ERT monitoring of resistivity changes is capable of revealing complex transport processes (Kemna et al., 2002). Electrical resistivity is usually mapped two- or three-dimensional as summarized by Loke et al. (2013). The advantage of ERT compared to other methods that image the resistivity distribution lies in measurement speed and model resolution properties. The simple field set-up makes is perfect for long-term monitoring of near surface resistivity anomalies like saltwater. Laboratory experiments simulating a cross-hole ERT monitoring in 2D and 3D were conducted to image a saline tracer in heterogeneous material (Slater et al., 2000; Slater et al., 2002).

Recent investigation deal with the development of automated monitoring systems (Kuras et al., 2009). Ogilvy et al. (2009) used 2D ERT for monitoring saltwater inundations of coastal aquifer. They showed that time-lapse ERT images are able to determine saltwater intrusions with improved confidence and efficiency compared to common well sampling. Nguyen et al. (2009) also showed that saltwater intrusion into a coastal aquifer is well resolvable by ERT, but concluded that higher mass fractions of chlorine at larger depths are still poorly resolved due to a limited investigation depth. Besides saltwater intrusions, ERT can also be applied on different kinds of contamination that cause resistivity changes. For example, LaBrecque et al. (1996) monitored environmental remediation processes involving temperature effects or the separation of high and low resistive areas due to electrokinetic soil decontamination.

Large-scale three-dimensional ERT imaging using surface electrodes can be limited, as the investigation depth and lateral extension can often not cover the target appropriately. To overcome these limitations, some recent publications investigate the use of boreholes as long electrodes to conduct ERT surveys, so-called long-electrode ERT (LE-ERT). Early studies of long electrode ERT (LE-ERT) use metal-cased boreholes only for current transmission to investigate electrical properties of hydrocarbons (Rocroi and Koulikov, 1985). Later applications use long electrodes for both current transmission and potential measurements. Ramirez et al. (1996) monitored tracer movements using a tank and boreholes as electrodes. An application with geothermal background was done by Ushijima et al. (1999), where fluid flow was monitored. In the context of CO_2 injection, Ramirez et al. (2003) did sensitivity studies comparing long electrode with vertical point electrode surveys. For the characterization of oil and gas fields, Daily et al. (2004) suggested using metal casings as electrodes to detect reservoir changes during the production. Another near-surface application involving contamination was presented in Rucker et al. (2011b). They conducted rather small-scaled monitoring measurements using long electrodes for characterizing a highly conductive leakage into a resistive host soil. Further information about long-electrode studies and applications can be found in Rucker et al. (2010), Rucker et al. (2011a) or Rucker (2012).

This thesis investigates the possibility of using metal casings in order to develop a cost-efficient application for monitoring near-surface saltwater intrusions. Although the intrusion of saltwater into freshwater aquifers is a typical problem for a coastal region, in can appear on inland sites as well. For testing the developed measurement schemes, two inland test sites were chosen where freshwater aquifers are contaminated by saltwater. An overview of typical conditions that lead to inland saltwater intrusions is shown in Figure 1.1. All scenarios are based on geological conditions that occur in northern Germany.

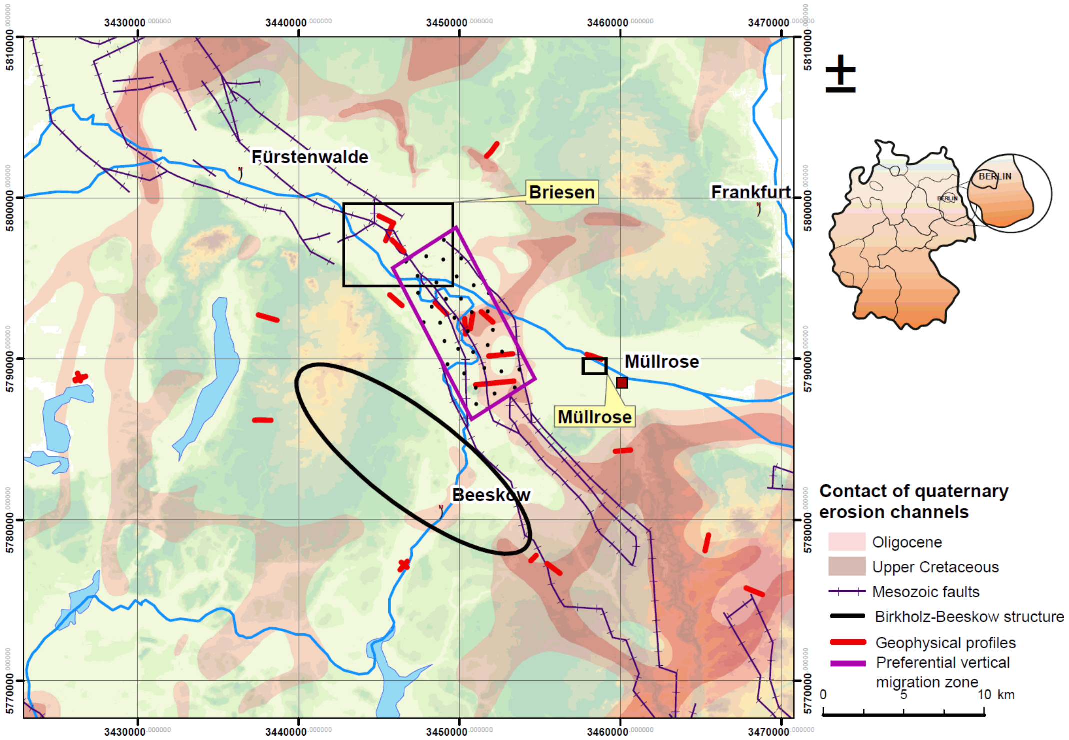

Figure 1.1: Geologic condition of south-east Brandenburg (fault zones and erosion channels). Both test-sites (Müllrose and Briesen) are marked with black rectangles. The assumed zone with where saltwater rises is marked with a purple rectangle (Kempka et al., 2015).

From a geological point of view, the chosen test-sites (Müllrose and Briesen) are part of the Berlin-Warsaw glacial valley. The uppermost layer consists of fluviatile sandy deposits of the Weichselian glaciation with thicknesses varying between 20 m and 40 m, followed by Pleistocene silts, sandy silts or tills down to ~100 m. Below ~100 m Miocene coal seams and clays are deposited, which are interbedded with thin fine sand layers. A 40-50 m thick quartz- and mica-sand aquifer follows, which is a regionally important groundwater resource. This aquifer is underlain by the ~50 m thick Rupelian clay. The Rupelian clay is an important impervious layer that separates freshwater from deep saline aquifers. The NW–SE striking Fürstenwalde-Guben fault zone (FGFZ) has led to a post-sedimentary subsidence of the basement. In this area, the FGFZ is divided into smaller blocks that moved separately from each other, which led to different depth levels of the Rupelian clay. Additionally, the Rupelian clay is partially or completely eroded by glacial events in some areas, which are marked with a brown colour in Figure 1.1. Gaps in the clay formation either

caused by a vertical shift over its whole thickness or by glacial erosion forms gaps in the Rupelian clay and opens flow-paths, which enables vertical fluid transport.
In conjunction with fault zones in upper Cretaceous formations as shown in Figure 1.1 and a vertical hydraulic gradient, an upward surge of saltwater is possible. This can be additionally accelerated or sustained by anthropogenic factors like an extensive groundwater extraction. All circumstances are present in southern Brandenburg, which is the reason why two test sites were chose here for conducting ERT monitoring.

After a short theoretical overview in chapter 2, different models for discretising long electrodes are presented in chapter 3. Synthetic studies investigate sensitivity distributions and model resolution properties to point out possible improvements for LE-ERT layouts. The influence of parameters like contact impedances and accuracy investigations concerning long electrode discretisation are also taken into account in the synthetic study. Chapter 4 shows 2D and 3D laboratory experiments. These were designed to simulate different saltwater intrusion scenarios, investigate the performance of ERT time-lapse inversion and to test algorithms that generate an optimised set of dipole combinations, by means of a maximal information content. Finally, the chapters 5 and 6 present two field cases. LE-ERT monitoring experiments are presented, which were conducted on the medium-scale $500\,\mathrm{m} \times 500\,\mathrm{m}$ test site. Two surveys were conducted on the second large-scaled test site covering an area of about $5\,\mathrm{m} \times 5\,\mathrm{km}$ each. Afterwards both data sets were combined to cover an even larger area of about $7\,\mathrm{km} \times 7\,\mathrm{km}$. Finally, chapter 7 summarises all synthetic studies and conducted experiments and gives a general conclusion including a short outlook.

Two chapters of this thesis have already been submitted in scientific journals. Results of synthetic studies shown in chapter 3 are published in Ronczka et al. (2015a) and synthetic studies and inversion results of the first field case, presented in chapter 5, are published in Ronczka et al. (2015b).

2 Theory

2.1 Electrical properties of natural material

An electrical current that flows through a conductor can be described by equation 2.1, which is known as Ohm's law.

$$U = RI \tag{2.1}$$

It expresses that the current is directly proportional to the potential difference, which is measured between two points, with the current I [A] and the potential difference or voltage U [V]. The proportionality constant R [Ω] is called resistance. Equation 2.2 shows another form of Ohm's law, seen from a local point of view.

$$\mathbf{j} = \sigma \mathbf{E} \tag{2.2}$$

It states that the current density $\mathbf{j}$ [A/m^2] at a given location in a conductive material is directly proportional to the electrical field $\mathbf{E}$ [V/m] at the same location. The proportionality constant σ is a material-dependent parameter and called electrical conductivity, which is the inverse of the resistance. In the given form, the scalar σ describes isotropic materials, which is usually assumed. For non-isotropic material σ becomes the tensor $\underline{\sigma}$. The electrical conductivity is a highly dynamical physical material property with a range over 25 orders of magnitude, (Lange, 2005). In porous media, different conductivity mechanisms occur, which are connected in parallel. At first, the electrical properties of the matrix have to take into account. In case of natural material these are combinations of silicates, carbonates or sulphites. As the **matrix conductivity** σ_m is very low, it has in most cases a negligible influence on the overall conductivity. The only exception is, if the matrix is formed by ores or graphite. In this case, electronic conduction takes place as a special form of the matrix conductivity. Generally, a lattice of metal ions is surrounded by a cloud of electrons, which can move freely. The electronic conductivity has a significant effect if present.

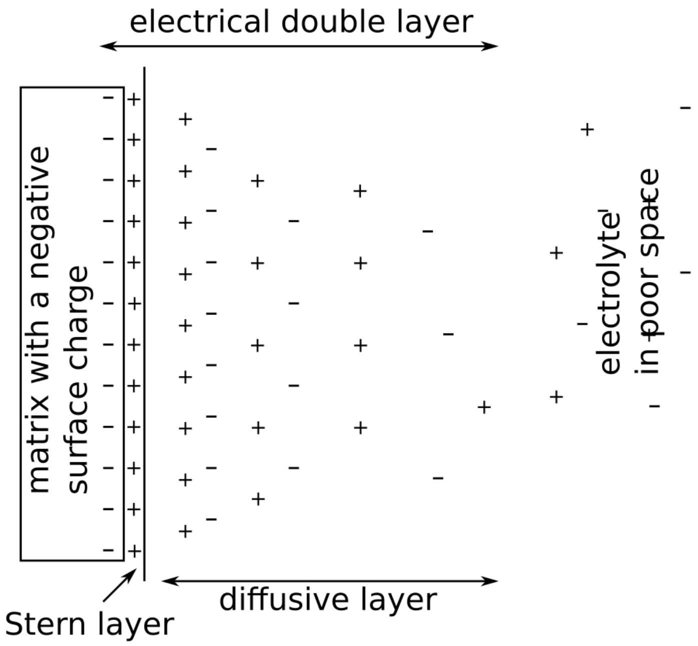

Figure 2.1: Schematic illustration of the electrical double layer (after Radic and Weller (2007)).

If pores are filled with an electrolyte, the electrolytic or **fluid conductivity** σ_f becomes important. In a pore fluid the electrical current is a result of anions and cations moving in opposite directions. The fluid conductivity is directly proportional to the amount of ions in the fluid that transport charges and to the temperature of the fluid. Pore fluids with higher ion content, i.e. salinity, have an increased electrical fluid conductivity σ_f. Higher mineralisation can occur for example due to solution processes of salt formations or the intrusion of saltwater in coastal regions. If the temperature is increased, the viscosity of the fluid decreases, which leads to a higher σ_f. In most field cases, the temperature effect on the electrical conductivity is only important for the shallow subsurface, because temperature variation decreases rapidly with depth.

The third mechanism in porous media is the **surface conductivity** σ_s. Due to the negative surface charge of the matrix, interactions with anions and cations of the fluid occur, which forms the electrical double layer. Cations are absorbed at the surface and build up the Stern layer, which has an overall negative charge and attracts cations from the pore fluid. As a result, the concentration of cations in the pore fluid decreases slightly. This forms the diffusive layer, directly on the pore side of the Stern layer. The ions that form the diffusive layer are considered to be mobile, whereas the ions of the Stern layer are not. The electrical double layer is schematically shown in Figure 2.1.

In general the surface conductivity is also connected with the cation exchange capacity of clay (Waxman and Smits, 1986). All significant conductivity mechanisms together form the bulk electric conductivity σ_b.
An important petro-physical part are mixing models that bring all conductivity mechanism together in a mathematical expression. Beyond the various physical and empirical models that exist, just one is mentioned that is based on Archie's law. All models based on Archie's law, make the assumption that each conductivity mechanism is considered independently. The second Archie equation states that the ratio of the electrical fluid- and bulk-conductivity is constant and indirectly proportional to the porosity (Φ) and saturation (S).

$$\frac{\sigma_f}{\sigma_b} = \frac{a}{\Phi^m S^n} = F \tag{2.3}$$

In which F is the formation factor [-], a a proportional constant, m the cementation exponent and n the saturation exponent. By extending Archies formula (Archie, 1942) with the surface conductivity, the bulk conductivity σ_b can be calculated according to equation 2.4.

$$\sigma_b = \frac{1}{F}\sigma_f S^n + \sigma_s \tag{2.4}$$

If the pores of the material are completely saturated with fluid, the saturation S equals 1. For a partially saturated medium σ_b will be reduced due to the presence of air in the pores. If the saturation of a porous medium with a fluid constantly decreases, the overall conductivity is more and more dominated by σ_s as long as a coherent double layer exist. Electrical resistivities for common geologic materials are given in table 2.1 after Seidel and Lange (2007).

Material	Resistivity [Ωm]	
	min.	max.
gravel	50 (saturated)	$>10^4$ (dry)
sand	50 (saturated)	$>10^4$ (dry)
silt	20	50
loam	30	100
clay (wet)	5	30
clay (dry)	-	>1000
sandstone	<50 (wet,jointed)	$>10^5$ (compact)
limestone	100 (wet,jointed)	$>10^5$ (compact)
natural water	10	300
salt water (35 ‰)	0.25	-

Table 2.1: Resistivity ranges for different consolidated and unconsolidated materials after Seidel and Lange (2007).

If a temporal shift appears between the transmitted current and measured voltage, the electrical resistivity can be described be an amplitude and phase or by a complex number. The real part is called effective resistance and the imaginary part reactance. As only direct current methods are used in this thesis, all frequency effects are neglected.

2.2 Measurement of electrical properties

2.2.1 Principles

According to Ohm's law in equation 2.1, the resistance R of a material can be determined by applying a known current I and measuring the voltage U. Assuming the simple case of a homogeneous half-space, which is assigned with a certain resistivity, the current transmission can be realised with two electrodes. As the voltage can only be measured between two points, the current electrodes or two additional electrodes can be used. For an arbitrary inhomogeneous resistivity distribution, the measured voltage depends on the electrode positions. In this case, more sophisticated approaches have to be used that describe the complex physics.

All electric and electromagnetic fields can be described by four partial differential equations (PDE) known as Maxwell equations. For direct current methods like geoelectric measurements, all temporal derivatives can be omitted. The electric field $\mathbf{E}$ can be described by a scalar field with $\mathbf{E} = -\nabla U$, which agrees with the second Maxwell equation ($\nabla \times \mathbf{E}$=0). By combining $\mathbf{E} = -\nabla U$ with equation 2.2 and applying the divergence $\nabla \cdot \mathbf{F} = \sum_i \partial / \partial x_i \mathbf{F}$ leads to

$$\nabla \cdot (\sigma \nabla(U)) = -\nabla \cdot \mathbf{j} \text{ in } \Omega \tag{2.5a}$$

$$\sigma \left(\frac{\partial U}{\partial \mathbf{n}} + \beta U \right) = \mathbf{j} \cdot \mathbf{n} \text{ on } \partial\Omega \tag{2.5b}$$

The governing geoelectrical boundary value problem is given by the differential equation 2.5a of Poisson type and the mixed boundary condition (equation 2.5b), as described by, e.g., Dey and Morrison (1979) or Rücker et al. (2006). They describe the potential $U(\mathbf{r})$ at a location $\mathbf{r}$ for a given conductivity distribution $\sigma(\mathbf{r})$ as a result of the current density $\mathbf{j}$ in the domain Ω or its boundary $\partial\Omega$ with the normal vector $\mathbf{n}$. Different types of boundary conditions can be incorporated by choosing β accordingly. For example, if $\beta = 0$ and $\mathbf{j} = 0$, the

homogeneous Neumann condition demands equipotential lines parallel to the boundary, which is needed for the interface towards an insulator like the earth's surface for example.
For a homogeneous domain and if no additional charges appear or disappear, equation 2.5b transforms into a Laplace-type PDE of the form $\nabla^2 U = 0$. Its solution for a homogeneous half-space is given in equation 2.6 and describes the potential distribution for a single point electrode at the surface with a current transmission at r_0.

$$U = \frac{I\rho}{2\pi r} \text{ with } r = |\mathbf{r} - \mathbf{r}_0| \tag{2.6}$$

The potential U decreases with $1/r$ and has only a radial component, thus forming spherical equipotential surfaces. The gradient of the potential $grad(U)$ or ∇U equals the electric field $\mathbf{E}$, which decreases radial with $1/\mathrm{r}^2$ according to equation 2.6. The potential drop $U_1 - U_2$ between two point electrodes P1 and P2 with distances r_1 and r_2 from the current transmission can be calculated by integrating the potential gradient $-\frac{\partial U}{\partial r} = \frac{I\rho}{2\pi r^2}$ from r_1 to r_2, (Wenner, 1916). The potential drop between two electrodes is given in equation 2.7.

$$U_1 - U_2 = \frac{I\rho}{2\pi} \int_{r_1}^{r_2} r^{-2} dr = \frac{I\rho}{2\pi} \left[\frac{1}{r_1} - \frac{1}{r_2} \right] \tag{2.7}$$

The four-point method for estimating the electrical resistivity was first suggested by Wenner (1916). The key point is the separation of the current transmission from the voltage measurement circuit. Due to the high internal resistance of the voltage circuit, almost no current flows and thus no additional voltage drop appears. Thus, the influence of contact impedances on the voltage measurement is negligible. A schematic 4-point measurement is shown in Figure 2.2.

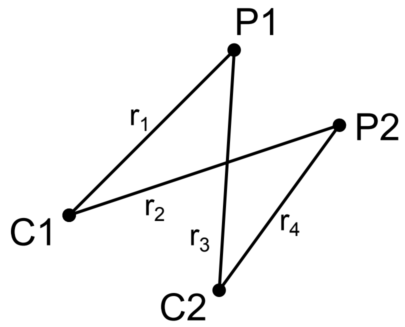

Figure 2.2: Schematic sketch of an ERT 4-point measurement with the current dipole C1–C2, the potential dipole P1–P2 and the electrode distances r_1–r_4 (plan view).

The voltage, i.e. potential difference ΔU for a 4-point measurement can be calculated according to equation 2.9, which is simply the superposition of the single potentials. The indices of the potentials $U_{1,2}$ and $U_{3,4}$ are referred to the distances r_1–r_4 in Figure 2.2. According to this, $U_{1,2}$ is the potential difference between P1 and P2 with the source C1 and $U_{3,4}$ the potential difference between P1 and P2 with the source C2.

$$U_{1,2} = \frac{I\rho}{2\pi}\left(\frac{1}{r_1} - \frac{1}{r_2}\right) \qquad U_{3,4} = \frac{I\rho}{2\pi}\left(\frac{1}{r_3} - \frac{1}{r_4}\right) \tag{2.8}$$

$$\Delta U = U_{1,2} - U_{3,4} = I\rho\left[\frac{1}{2\pi}\left(\frac{1}{r_1} - \frac{1}{r_2} - \frac{1}{r_3} + \frac{1}{r_4}\right)\right] \tag{2.9}$$

By transposing equation 2.9 and replacing the term in parentheses with $1/K$ the electrical resistivity ρ can be calculated for a homogeneous half-space by:

$$\begin{aligned} \rho &= K\frac{\Delta U}{I} \\ with\quad K &= \left[\frac{1}{2\pi}\left(\frac{1}{r_1} - \frac{1}{r_2} - \frac{1}{r_3} + \frac{1}{r_4}\right)\right]^{-1} \end{aligned} \tag{2.10}$$

The geometric factor K in equation 2.10 can be simply calculated for all common configurations used for ERT measurements. Configurations and corresponding analytic formulas for calculating the geometric factor is given in Figure 2.3 Nevertheless, K can only be calculated analytically if the point electrode approximation is valid. Otherwise, it has to be estimated numerically on the base of a homogeneous half-space.

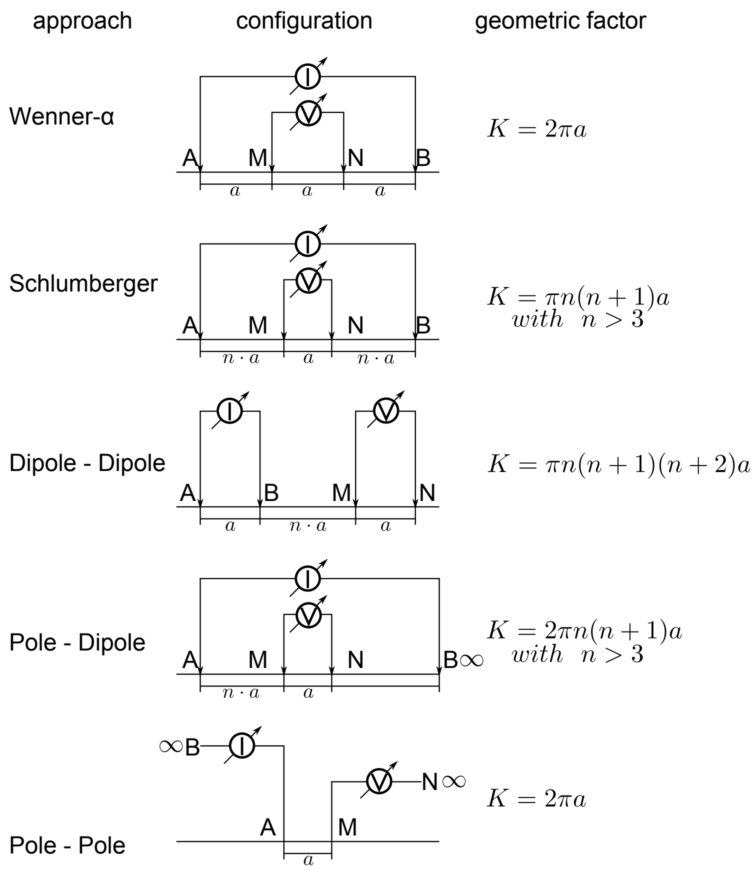

Figure 2.3: Commonly used configurations for ERT measurements with analytic formulas for calculating the geometric factor after Lange (2005).

2.2.2 Electrical resistivity tomography (ERT)

The measured resistivity ρ (equation 2.10) is independent from the electrode positions for a homogeneous half-space. In contrast, for heterogeneous media, the measured resistivity depends on the electrode configuration as well as the positions on the surface. Hereby, the investigation depth of a single measurement is controlled by the distance between electrodes. Most commonly 2D ERT measurements are carried out along profiles, to image a heterogeneous resistivity distribution. Several electrodes are placed along a profile line, which are wired and controlled by an apparatus that automatically transmits the current and measures the voltage following a pre-defined scheme shown in Figure 2.3 for example.

The geometry of each measurement is considered by multiplying each resistivity with its geometric factor K. The obtained data are called apparent resistivities ρ_a, because they are an integral value and not assigned to a specific depth. In order to estimate a resistivity distribution that explains the measured data within a realistic error model an inversion is needed that uses numerical methods such as the finite element method (FEM).

2.3 Finite element method for ERT forward modelling

Most partial differential equations cannot be solved analytically, or only for simple cases. Several numerical approaches exist to solve equations (2.5a) and (2.5b) using the Finite Difference (FD) or Finite Element Methods (FEM). As one of the first, Coggon (1971) used FEM for electromagnetic and electrical modelling using the variational method. We follow the approach based on the Galerkin method described in Pridmore et al. (1981) or Rücker et al. (2006) using FEM on unstructured tetrahedral or triangle prism grids with linear or quadratic shape functions. A set of local trial functions is used, each approximating the solution $\phi(x, y, z)$ of a differential equation on a small part of the domain Ω.

Every $\phi(x, y, z)$ is defined zero outside. A simple and common form are linear trial functions given in equation 2.11 depending on node positions x, y and z.

$$\phi(x, y, z) = \alpha_1 + \alpha_2 x + \alpha_3 y + \alpha_4 z \tag{2.11}$$

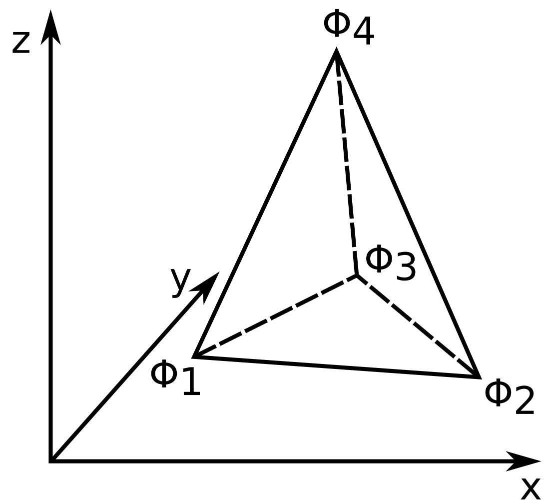

Figure 2.4: Tetrahedral element with the trial functions ϕ_i with i = 1 ... 4 at the nodes, to approximate the solution of a differential equation.

Equation 2.11 with the coefficients α_1–α_4 describes a tetrahedral element as it is shown in Figure 2.4. For all four nodes of the tetrahedron the matrix form of equation 2.11 leads to:

$$\begin{bmatrix} \phi_1 \\ \phi_2 \\ \phi_3 \\ \phi_4 \end{bmatrix} = \begin{bmatrix} 1 & x_1 & y_1 & z_1 \\ 1 & x_2 & y_2 & z_2 \\ 1 & x_3 & y_3 & z_3 \\ 1 & x_4 & y_4 & z_4 \end{bmatrix} \begin{bmatrix} \alpha_1 \\ \alpha_2 \\ \alpha_3 \\ \alpha_4 \end{bmatrix} \tag{2.12}$$

Let the matrix in equation 2.12 be $\mathbf{B}$ with the inverse $\mathbf{C} = \mathbf{B}^{-1}$ containing the elements $c_{i,j}$. The coefficients α_i with i=1...4 can be determined by solving the system of equations given above. By substituting α_i in equation 2.11 and reorganizing with respect to ϕ_i the following expression for $\phi(x, y, z)$ is obtained:

$$\begin{aligned} \phi(x, y, z) =& (c_{1,1} + c_{2,1}x + c_{3,1}y + c_{4,1}z)\phi_1 + \\ & (c_{1,2} + c_{2,2}x + c_{3,2}y + c_{4,2}z)\phi_2 + \\ & (c_{1,3} + c_{2,3}x + c_{3,3}y + c_{4,3}z)\phi_3 + \\ & (c_{1,4} + c_{2,4}x + c_{3,4}y + c_{4,4}z)\phi_4 \, , \end{aligned} \tag{2.13}$$

with the shape functions $N_k(x, y, z) = (c_{1,k} + c_{2,k}x + c_{3,k}y + c_{4,k}z)$ for k=1...4. Hat-functions had proven to be useful and thus are commonly chosen as $N_k(x, y, z)$, which build up triangles in 2D or tetrahedrons in 3D as shown schematically in Figure 2.4. Equation 2.13 can be summarized to $\phi(x, y, z) = \sum_{k=1}^{4} N_k(x, y, z)\phi_k$. To solve for the unknown ϕ_k, the weighted-residual method is used. For a geoelectrical problem, a potential distribution is sought to solve equation 2.5a, which means that the trial functions are set to the potential, i.e. $\phi(x, y, z) = U(x, y, z)$. As the second derivative is not defined for hat-functions, the weak formulation of equation 2.5a has to be used. It allows an approximation of the potential without the requirement of a second derivative.

$$\begin{aligned} &\int_\Omega \sigma \cdot \nabla v \nabla U \, d\Omega + \int_\Gamma \sigma \alpha v U \, d\Gamma = \\ &\int_\Omega v(\nabla \cdot \mathbf{j}) \, d\Omega + \int_\Gamma v(\mathbf{j} \cdot \mathbf{n}) \, d\Gamma \end{aligned} \tag{2.14}$$

The weak formulation given in equation 2.14 using the weighting functions v has to be solved for the area Ω with its boundaries Γ. For more information, the detailed derivation is given in Zienkiewicz (1977). By using the Galerkin-method, the weighting functions v in equation 2.14 are substituted with the shape functions $N_k(x, y, z)$. As described in Rücker et al. (2006) the finite element formulation than can be written as follows:

$$\begin{aligned} &\sum_{k=1}^{N} \left(\int_\Omega \sigma \nabla N_k \cdot \nabla N_l \, d\Omega + \int_\Gamma \sigma \alpha N_k N_l \, d\Gamma \right) \mathbf{u} = \\ &\sum_{i=1}^{E} \int_\Omega N_k(\nabla \cdot \mathbf{j}) \, d\Omega + \sum_{i=1}^{B} \int_\Gamma N_k(\mathbf{n} \cdot \mathbf{j}) \, d\Gamma \end{aligned} \tag{2.15}$$

Equation 2.15 can be written in matrix form like $\mathbf{K}_{k,l}\mathbf{u}_l = \mathbf{b}_k$, whereas the matrix $\mathbf{K}$ contains the integrals on the left-hand side and is called stiffness matrix. The right-hand side integrals of equation 2.15 are summarised to $\mathbf{b}$, which is called load vector. As local trial functions are just defined for a single element and are zero elsewhere, the integral in the stiffness matrix decomposes into integrals over single elements, with constant derivatives of the hat-functions within each single element. By using mixed boundary conditions, which defines the solution u at specific nodes and boundaries, the system of equations given above is always solvable.

2.4 Inversion

Inversion of geophysical data describes the process of estimating a model whose forward response, i.e. synthetic data, fits observed data under predefined conditions. For non-linear problems like ERT, data are related to model parameter by the system of equations $\mathbf{d} = \mathbf{f}(\mathbf{m})$, whereas $\mathbf{d}$ denotes a data vector and $\mathbf{m}$ the model parameter vector. The inversion of non-linear problems is an iterative process with a starting model $\mathbf{m}^0$, which is modified by model updates $\mathbf{\Delta m}$ until the forward response $\mathbf{f}(\mathbf{m})$ fits the observed data. A new model is calculated in each iteration step n with $\mathbf{m}^{n+1} = \mathbf{m}^n + \Delta\mathbf{m}^n$. As described in Günther (2004) a Taylor-approximation of the forward response is used for the linearisation. The truncation after the first term leads to:

$$\mathbf{f}(\mathbf{m}^n + \Delta\mathbf{m}^n) \approx \mathbf{f}(\mathbf{m}^n) + \frac{\partial \mathbf{f}(\mathbf{m}^n)}{\partial \mathbf{m}} \Delta\mathbf{m^n} = \mathbf{f}(\mathbf{m}^n) + \mathbf{J}\Delta\mathbf{m^n}\,. \tag{2.16}$$

The partial derivative $\frac{\partial \mathbf{f}_i(\mathbf{m}^n)}{\partial m_j} = \mathbf{J}_{i,j}(\mathbf{m}^n)$ is called sensitivity or Jacobian matrix. If the data $\mathbf{d}$ are set equal to the new model response, the linearised inverse problem is given as:

$$\mathbf{J}\Delta\mathbf{m} = \mathbf{d} - \mathbf{f}(\mathbf{m})\,. \tag{2.17}$$

In order to find a set of model parameters whose forward response fit the observed data, equation 2.18 has to be minimised. In general, different norms can be used that minimise the misfit, for example the L_1-norm ($\|\|_1$), which is robust, if data outliers occur. Another norm that is commonly used for inversion is the L_2-norm ($\|\|_2$) that leads to a least squares solution.

$$\mathbf{\Phi}_d(\mathbf{m}) = \sum_{i=1}^{N} \left| \frac{d_i - f_i(\mathbf{m})}{\epsilon_i} \right|^2 \tag{2.18}$$

As described in Günther (2004), ϵ_i in equation 2.18 is an estimated error for the data point d_i. Errors can be used for a weighting operator by collecting them as diagonal elements in a matrix $\mathbf{D} = \mathrm{diag}(1/\epsilon_i)$. Thus, the matrix form of the error weighted misfit in equation 2.18 is simply $\mathbf{\Phi}_d = \|\mathbf{D}(\mathbf{d} - \mathbf{f}(\mathbf{m}))\|^2$, which can be written as:

$$\mathbf{\Phi}_d = (\mathbf{d} - \mathbf{f}(\mathbf{m}))^T \mathbf{D}^T \mathbf{D} (\mathbf{d} - \mathbf{f}(\mathbf{m})) \tag{2.19}$$

An indicator for data fitting is the χ^2 value, which is calculated after equation 2.20. Because it is independent of the data amount, the fit from different data sets can be compared.

$$\chi^2 = \mathbf{\Phi}_d / N \tag{2.20}$$

The objective function that has to be minimised in every iteration step can be calculated by several methods, for example steepest decent, conjugate gradient or Newton-type methods, described in detail in Günther (2004). For Newton-type methods, a Taylor series of equation 2.19 for the model update $\mathbf{m} + \Delta\mathbf{m}$ is done with respect to the model parameters. This leads to $(\nabla^2\mathbf{\Phi})\Delta\mathbf{m}^n = -\nabla\mathbf{\Phi}$, which has to be solved for estimating the model update. The functional $\mathbf{\Phi}_d$ then reads:

$$H_d^n = \nabla\nabla^T \mathbf{\Phi}_d = \mathbf{J}^T\mathbf{D}^T\mathbf{D}\mathbf{J} + (\nabla^T\mathbf{J}^T)\mathbf{D}^T\mathbf{D}(\mathbf{f}(\mathbf{m}^n) - \mathbf{d})\,, \tag{2.21}$$

where H_d^n is the Hessian matrix with $H_d^n = (\nabla^2\mathbf{\Phi}_d)_{ij} = \frac{\partial^2\mathbf{\Phi}_d}{\partial m_i \partial m_j}$. The Gauss-Newton approach uses, as described in Günther (2004), the Hessian approximation, reducing the right hand side of equation 2.21 to $H_d^n = \mathbf{J}^T\mathbf{D}^T\mathbf{D}\mathbf{J}$.
The inverse problem of ERT is generally under-determined, which means that more model parameters exist than observed data, resulting in better and worse resolved parts of the parameter domain. Poorly resolved model parameters can lead to artefacts, disturbing the parameter domain. These can be damped, if the norm of the model parameter vector $\mathbf{m}$, i.e. its length, is sought to be minimal.

$$\mathbf{\Phi}_m = \sum_{j=1}^{M} m_j^2 = \mathbf{m}^T\mathbf{m} \tag{2.22}$$

The cost function consists of L_2-norms for an error-weighted data misfit $\mathbf{\Phi}_d$ and a model roughness $\mathbf{\Phi}_m$, weighted by the regularization parameter λ:

$$\mathbf{\Phi} = \Phi_d + \lambda\Phi_m = \sum_{i=1}^{N} \mid \frac{d_i - f_i(\mathbf{m})}{\epsilon_i} \mid^2 + \lambda \parallel \mathbf{C}(\mathbf{m} - \mathbf{m^0}) \parallel_2^2 \,. \tag{2.23}$$

The model $\mathbf{m}$ holds the logarithms of the cell resistivities, $\mathbf{C}$ is a derivative matrix and $\mathbf{m^0}$ the reference model (Günther et al., 2006). The regularization parameter is chosen such that the data d_i are fitted by the forward responses f_i statistically within their error levels ϵ_i, i.e. $\chi^2 = 1$ is reached. The functional 2.21 for a Gauss-Newton scheme that has to be solved in every iteration step is extended by a damping part and reads:

$$\left(\mathbf{J}^T\mathbf{D}^T\mathbf{D}\mathbf{J} + \lambda\mathbf{C}^T\mathbf{C}\right)\mathbf{\Delta m} = \mathbf{D}^T\mathbf{D}\mathbf{J}\left(\mathbf{d} - \mathbf{f}(\mathbf{m})\right) - \lambda\mathbf{C}^T\mathbf{C}\mathbf{m}\,, \tag{2.24}$$

where $\mathbf{D}$ is a diagonal weighting matrix (Günther et al., 2006). These inversion schemes are used to image a resistivity distribution at a certain time. It is not possible to observe subsurface processes that change the resistivity.

2.4.1 Time lapse inversion

For observing temporal variations of the subsurface electrical resistivity the time-lapse inversion has gained much attention. Different transport processes can be imaged that influence the resistivity like temperature changes, the movement of contaminants, saltwater intrusions or remediation processes that use the injection or extraction of fluids. For time-lapse measurements, a number of k surveys, i.e. time steps, are conducted on a test site over a specified time span. Ideally, the first time steps should be conducted during undisturbed resistivity distribution. Nevertheless, a vital point is a good quality of the base-line measurement, which is used as the reference for following data sets. For subsequent time steps (k) in time-lapse inversion, the second term in equation (2.23) is changed to minimise the smoothness of the model differences:

$$\begin{aligned} &\lambda\Phi_m \Rightarrow \lambda_t\Phi_m^k \\ &\text{with } \Phi_m^k = \| \mathbf{C}(\mathbf{m}^{(k)} - \mathbf{m}^{(ref)}) \|_2^2 \,, \end{aligned} \tag{2.25}$$

where λ_t controls the strength of the temporal smoothness between the time steps. Two common time-lapse approaches exist that use different base-line models $\mathbf{m^{(ref)}}$. In the first one, the base-line is fixed to a single model, for example the first or one of the first time steps. The second approach, known as time-lapse-step model (TLS) uses the previous time step $k-1$ as base-line to minimise the difference to the kth model. Depending on which data-set is less corrupted by noise, the order in which the time steps are fitted can be reversed. All forward and inverse calculations in this work are done with the open-source software BERT (Boundless Electrical Resistivity Tomography) package (Günther et al., 2006).

2.5 Model and data resolution for quality assessment

To estimate resolution properties of an electrode set-up, an approach after Friedel (2003) can be used. The model resolution matrix $\mathbf{R}^M$ and the data resolution matrix $\mathbf{R}^D$ can be calculated using the singular value decomposition (SVD) of the Jacobian matrix $\mathbf{J}$. Generally, ill-conditioned least-square problems can be solved by the SVD (Aster et al., 2005). Nonetheless, it is only used for calculating the model and data resolution matrices in this work, because of its simple implementation. The matrix $\mathbf{F}$ of the size $m \times n$ in $\mathbf{d} = \mathbf{Fm}$ can be written as

$$\mathbf{F} = \mathbf{U}\hat{\mathbf{\Lambda}}\mathbf{V}^T \,, \tag{2.26}$$

where the columns of the $n \times n$-matrix $\mathbf{U}$ is spanning the data space. The columns of the $m \times m$ matrix $\mathbf{V}$ is spanning the model space and $\hat{\mathbf{\Lambda}}$ is a diagonal matrix of the size $m \times n$ containing the singular values as diagonal elements, (Aster et al., 2005). The diagonal elements of $\hat{\mathbf{\Lambda}}$ decrease from $\hat{\lambda}_1 \geq \hat{\lambda}_2 \geq ... \geq 0$. Thus, $\hat{\mathbf{\Lambda}}$ can be decomposed in

$$\hat{\mathbf{\Lambda}} = \begin{bmatrix} \hat{\mathbf{\Lambda}}_p & 0 \\ 0 & 0 \end{bmatrix} \tag{2.27}$$

with the $p \times p$ diagonal matrix $\hat{\mathbf{\Lambda}}_p$. As the last $m - p$ columns of $\mathbf{U}$ and $n - p$ columns of $\mathbf{V}$ can be omitted due to the multiplication with the zeros of $\hat{\mathbf{\Lambda}}$, equation 2.26 can be modified to $\mathbf{F} = \mathbf{U}_p\hat{\mathbf{\Lambda}}_p\mathbf{V}_p^T$. The remaining $m - p$ and $n - p$ columns of $\mathbf{U}$ and $\mathbf{V}$ are often called data- (U_0) or model-null space (V_0). It can be shown that equation $\mathbf{d} = \mathbf{Fm} = \mathbf{U}_p\hat{\mathbf{\Lambda}}_p\mathbf{V}_p^T\mathbf{m}$ has no components in the data- and model-null spaces $\mathbf{U}_0$ and $\mathbf{V}_0$, (Menke, 1989). Thus, the inverse problem can be written as,

$$m^{est} = \mathbf{V}_p\hat{\mathbf{\Lambda}}_p^{-1}\mathbf{U}_p^T\mathbf{d} \tag{2.28}$$

As stated in Menke (1989) the natural generalized inverse for a mixed-determined problem is given by $F^{-g} = \mathbf{V}_p\hat{\mathbf{\Lambda}}_p^{-1}\mathbf{U}_p^T$. The corresponding model resolution $\mathbf{R}^M$ and data resolution $\mathbf{R}^D$ can be calculated following equation 2.29 and equation 2.30.

$$\mathbf{R}^M = \mathbf{F}^{-g}\mathbf{F} = \{\mathbf{V}_p\hat{\mathbf{\Lambda}}_p^{-1}\mathbf{U}_p^T\}\{\mathbf{U}_p\hat{\mathbf{\Lambda}}_p\mathbf{V}_p^T\} = \mathbf{V}_p\mathbf{V}_p^T \tag{2.29}$$

$$\mathbf{R}^D = \mathbf{F}\mathbf{F}^{-g} = \{\mathbf{U}_p\hat{\mathbf{\Lambda}}_p\mathbf{V}_p^T\}\{\mathbf{V}_p\hat{\mathbf{\Lambda}}_p^{-1}\mathbf{U}_p^T\} = \mathbf{U}_p\mathbf{U}_p^T \tag{2.30}$$

The model parameter and data are perfectly resolved, if $\mathbf{R}^M$ and $\mathbf{R}^D$ are identity matrices $\mathbf{R}^M = \mathbf{R}^D = \mathbf{I}$. Normally, both matrices $\mathbf{R}^M \neq \mathbf{I}$ and $\mathbf{R}^D \neq \mathbf{I}$ are not diagonal matrices due to errors, linear dependencies or poorly resolved parts of the model space. Generally, the more $\mathbf{R}^M$ differs from $\mathbf{I}$ the worse the model parameter are resolved. The more $\mathbf{R}^D$ differs from $\mathbf{I}$, the more pronounced are dependencies between different data points.

3 Numerical study of long electrode ERT - accuracy, sensitivity and resolution

Main part of this chapter is published as follows:

Ronczka, M., C. Rücker and T. Günther, 2015a, Numerical study of long-electrode electric resistivity tomography - Accuracy, sensitivity and resolution: Geophysics, 80(6), E317-E328

3.1 Introduction

Several approaches exist that incorporate long electrodes for modelling and inversion. One analytical solution for the potential field of half-elliptical electrodes in a homogeneous half-space is derived in Igel (2007). However, it can be used only for point measurements; i.e., potential electrodes are point-like. Furthermore, three different numerical approaches have been presented in the geophysical literature for simulating long electrodes. The first method, described by Tan et al. (2004) and Zhu and Feng (2010), approximates the borehole by a line source (LS). However, Zhang et al. (2014) showed that the method assumes a constant current injection along the borehole and can thus not appropriately handle boreholes in non-homogeneous media. In Rucker et al. (2010), a conductive vertical grid column in conjunction with a point electrode at the surface is used. This model is referred to as the conductive cell model (CCM).

A third method to incorporate arbitrarily shaped electrodes in geoelectrical models is the complete electrode model (CEM), introduced by Rücker and Günther (2011). The electrode surface is discretised and coupled with the subsurface via contact impedances (z_L). For low impedance values, the electrode shape appears as an equipotential surface, which also results from a large conductivity contrast in the CCM. Hence, the results of the CCM and the CEM are expected to be similar if the same electrode shape is used. The difference is that the CEM does not discretise the interior of the electrode, thus reducing the numerical effort.

Typical steel-cased boreholes in environmental investigations exhibit a large length-width ratio. A discretisation that includes long electrodes will consequently lead to a large number of nodes and high numerical effort. To date, there has been no documented investigation of modelling errors related to the borehole radius. An alternative modelling strategy for perfectly coupled electrodes is shorting the involved mesh nodes in the matrix representation of the partial differential equation. This can be conducted by removing rows and columns (Wang et al., 1999) or, more easily, by increasing the conductance values in the matrix (Ramirez et al., 2003).

The historical usage of long electrodes is related to a few more limitations. First, as stated in Ramirez et al. (2003) and Rucker et al. (2011b), by using only equally long boreholes, the vertical resolution completely vanishes between the surface and electrode depth. It could be shown that an anomaly is horizontally detectable, but its exact depth is not. Nevertheless, more practical issues influencing LE-ERT measurements must be taken into account. Larger corroded parts of a metal casing lead to high contact impedances that possibly disturb electrical fields and thus measurements. Severe corrosion may also create gaps in the metal casing, thereby affecting electrical continuity along the casing. Casings can also be destroyed by being divided into separated parts, which may lead to wrong geometric factors.

Following the first modelling and resolution studies of Ramirez et al. (2003) and Rucker (2012), we carry out systematic synthetic simulations to obtain parameter sets that lead to sufficiently accurate numerical routines and to demonstrate the ability of the method in the context of saltwater intrusion. Discretisation parameters (electrode diameter, number of facets) were varied to appraise numerical error and effort. Sensitivity and resolution studies investigating the influence of electrode length and/or contact impedances are conducted to note the improvements and limitations of LE-ERT. Synthetic two-layer cases with a conductive anomaly representing a saltwater intrusion were constructed. LE-ERT measurements were simulated with long electrodes equidistantly arranged in three rows, each with 5 electrodes. Smoothness-constrained inversions were performed to investigate the imaging capabilities of LE-ERT with electrodes of different lengths.

3.2 Numerical modelling

To approximate the commonly used steel rod electrodes with a point at the location $\mathbf{r}_\mathrm{s}$, a singular current density function is chosen with $\mathbf{j} = \delta(\mathbf{r} - \mathbf{r}_\mathrm{s})$, called the point electrode model (PEM). PEM is valid if the spatial extension of the electrodes is small in comparison to the distance between electrodes (Rücker and Günther, 2011). To handle electrodes with a non-negligible extent, different strategies are necessary.

Rucker et al. (2010) simulates long electrodes by a column of cells which are assigned with a small resistivity. The current is transmitted by a surface point-electrode on top of the low resistive body. This highly conductive body of limited width shows a vanishing potential drop along its length and lets its surface appear to be an equipotential surface. A more sophisticated method for modelling long electrodes, CEM, was presented by Rücker and Günther (2011), a technique borrowed from medical imaging (Cheng et al., 1989). It adds the equations (3.1a) and (3.1b) to the boundary value problem:

$$z_L \sigma \frac{\partial u}{\partial \mathbf{n}} + u = U_L \text{ on } \partial\Omega_{\mathrm{E}_L} \tag{3.1a}$$

$$\int_{\partial\Omega_{\mathrm{E}_L}} \sigma \frac{\partial u}{\partial \mathbf{n}} ds = I \tag{3.1b}$$

Equation (3.1a) defines the potential distribution at the electrode surface $\partial\Omega_{\mathrm{E}_L}$ depending on the contact impedance z_L in $\Omega\mathrm{m}^2$. If z_L is negligible, the potential at the electrode surface is constant and equals the measured value U_L. If z_L has a significant influence, the potential changes along the electrode, influencing the electrical field in the vicinity of the electrode. Equation (3.1b) defines the total current I entering the subsurface through the whole connected electrode surface. A schematic display of differences in long electrode discretisation with CCM and CEM is shown in Figure 3.1.

To apply CEM or CCM, a discrete approximation of the electrode shape is necessary. For a higher flexibility in mesh generation, unstructured meshes for the finite element modelling are required. An unstructured mesh has been shown to have the best performance of numerical effort vs. accuracy in other geoelectrical scenarios (Rücker et al., 2006). Alternatively, Wang et al. (1999) simulate electrodes of negligible width but vary the contact impedance using the Shunt Electrode Model (SEM). In any FD or FE discretisation, a system of linear equations of the form $\mathbf{Ax} = \mathbf{b}$ is solved, where the vector $\mathbf{x}$ contains the voltages at the mesh nodes, $\mathbf{b}$ expresses the current distribution, and the

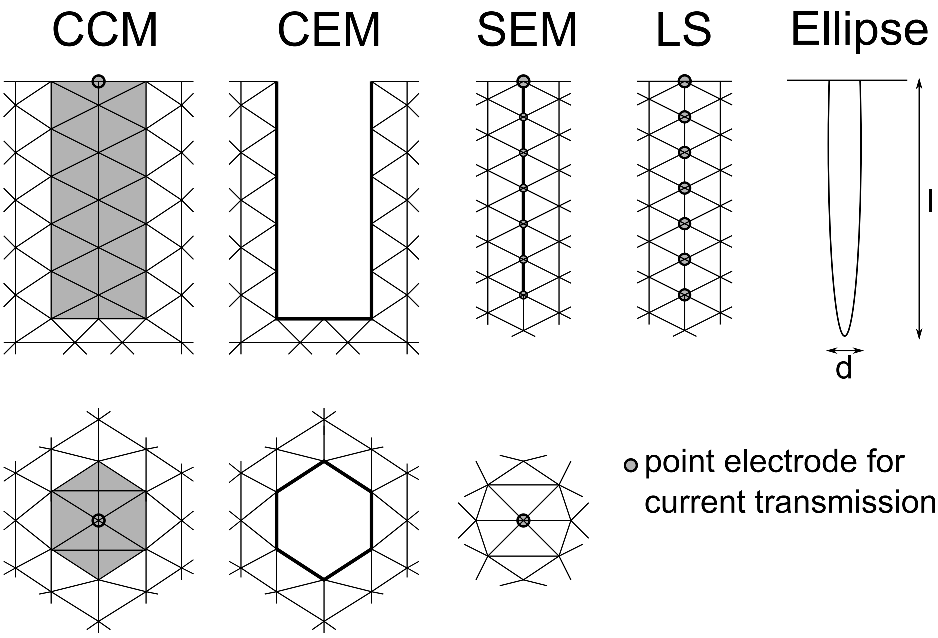

Figure 3.1: Schematic sketches (side view and top view) for electrode discretisations using CCM, CEM (with 6 faces each), SEM, LS (line source after Zhang et al. (2014)) and the analytical model that simulate an elliptic electrode. Grey triangles mark a mesh part assigned with a high conductivity and point electrodes are marked by large grey circles. The thick lines in CEM represent boundary conditions. For SEM, shunts between nodes (small circles) are indicated by thick lines.

matrix $\mathbf{A}$ represents a network of resistors (Zhang et al., 1995). The off-diagonal elements contain the negative conductances between the corresponding nodes, and the main diagonal contains the sum of adjacent conductances to ensure that the divergence of u is zero. To implement the SEM, we assume a number of nodes $\mathcal{N} = \{N_j\}$ that are part of the finite element mesh to represent the spatial extent but not the electrode geometry itself. All nodes are connected via shunt conductors of resistance R_{shunt} with the formal PEM node N_{PEM} by updating the system matrix $\mathbf{A}$ with:

$$\mathbf{A} = \mathbf{A} + \mathbf{A}_{\text{SEM}} \tag{3.2}$$

$$\mathbf{A}_{\text{SEM}} = \sum_{N_j \in \mathcal{N}} \frac{1}{R_{\text{shunt}}} \begin{bmatrix} 1 & -1 \\ -1 & 1 \end{bmatrix}_{i,j} \quad \text{with, } i = \text{constant} = N_{\text{PEM}} \; . \tag{3.3}$$

Zhang et al. (2014) compared two basic methods (line source and CCM) for two synthetic cases with an analytical solution. The line source model (LS) consists simply of a certain amount of point electrodes arranged in a line, as schematically shown in Figure 3.1. The current is transmitted using all point electrodes simultaneously. They found that the solution for the LS model (equally distributing the current on the electrode nodes) works well for the homogeneous case, but it fails for heterogeneous media, whereas CCM works well for both. We repeated the simulations, replacing the LS model with SEM and CEM and added the analytical solution for a half-ellipse shaped electrode. According to Igel (2007) and Sommerfeld (1967) the potential field of a half-elliptical electrode is given by:

$$\Phi = \frac{I}{4\pi\sigma e} \ln \left| \frac{z + e + \sqrt{x^2 + y^2 + (z+e)^2}}{z - e + \sqrt{x^2 + y^2 + (z-e)^2}} \right| , \tag{3.4}$$

with the coordinates x, y, z and $e = \sqrt{l^2 - \frac{d^2}{4}}$ containing the length l and the diameter d of the electrode. To compare all possibilities for discretising long electrodes, two models according to Zhang et al. (2014) were used. The first model consists of a $l = 44\,\text{m}$ long electrode with a diameter of $d = 0.2\,\text{m}$ in a homogeneous half-space with $\rho = 1\,\Omega\text{m}$. For the second model, a three-layered medium (a $10\,\Omega\text{m}$ layer embedded in a $30\,\Omega\text{m}$ half-space) with a thickness of 300 m each was simulated. The electrode length was set to $l = 800\,\text{m}$ and the diameter to $d = 2\,\text{m}$, referring to Zhang's model layout. A schematic sketch is shown in Figure 3.2.

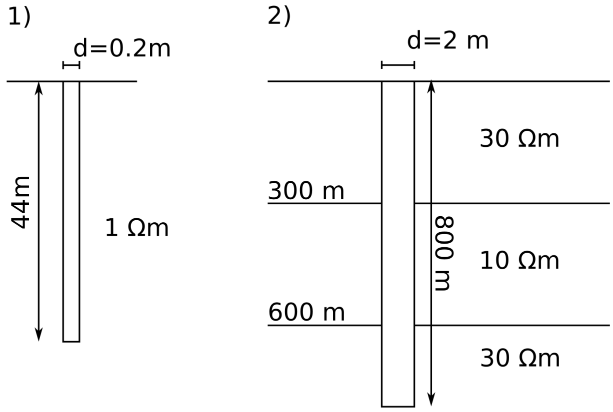

Figure 3.2: Synthetic models used by Zhang et al. (2014) to compare different approaches for long electrode discretisation. Model 1 simulates a homogeneous halfspace and model 2 a three-layer case.

The vertical distribution of the current density was observed at a lateral distance of 1 m (model 1) and 2.5 m (model 2) from the electrode centre, respectively. To ensure a sufficient accuracy, the node electrodes for SEM were set every 12.5 cm, whereas the CEM and CCM used regular cylinders. The resistivity of the conductive body that approximates the borehole for CCM was set to $\rho = 10^{-6}\,\Omega\text{m}$ to ensure a high contrast towards the surrounding. The calculated current densities are shown in Figure 3.3 for the three numerical approaches. For the first case, the analytical solution for a half-ellipse (Igel, 2007) using l and d as half-axes is additionally plotted.
Generally, all three electrode models show the same behaviour for both model cases. CEM and CCM are practically identical, which is not surprising because the same geometry and a large conductivity contrast are used. The result of SEM is slightly different, but in contrast to the line source (Zhang et al., 2014), it appears to handle the conductivity dependency of the transmitted current strength. All three electrode models show an increasing current density towards the bottom of the electrode, which is less pronounced for SEM. The half-ellipse solution does not show this behaviour, resulting from a significantly different geometry; i.e., the effective horizontal radius and thus the relative contact area decrease with depth. Thus, the increased distance to the electrode surface lowers the current density. The results lead to the conclusion that the half-ellipse solution does not describe the cylindrical borehole geometry sufficiently accurately and should not be used for long electrode modelling. CEM and CCM produce comparable results, whereas CEM is the most sophisticated model. By including contact impedances and using surfaces for current transmission it closest to physical reality. As the inner domain of the electrode is not discretised,

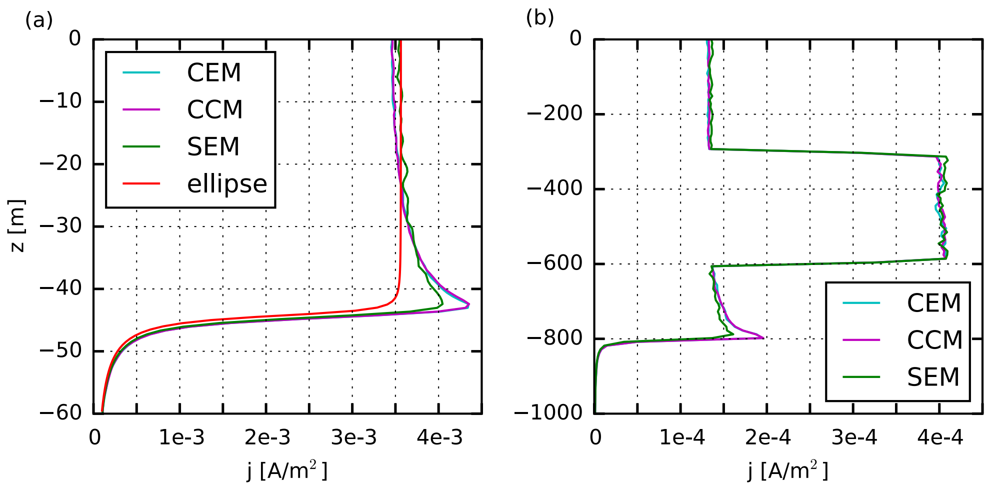

Figure 3.3: Absolute value of current density in the vicinity of the injection borehole as a function of depth, computed for three different electrode models for the cases of Zhang et al. (2014): (a) homogeneous half-space and (b) a 3-layer case. Distances from the electrode centre are 1 m and 2.5 m, respectively. For (a), the analytical solution of an half-elliptic electrode is added.

it is numerically more efficient and will be used for all forward calculations henceforth. SEM can be used for modelling if the borehole diameter is negligible or for inverse modelling to avoid an unnecessary high discretisation, i.e. model parameter (ill-posed problems).

3.2.1 Discretization and numerical accuracy

Boreholes are approximated by regular cylinder faces (CEM) or a number of coupled points (SEM), as depicted in Figure 3.1. For the accurate and efficient modelling of 4-point LE measurements, the influence of the mesh quality and the electrode geometry (diameter and number of facets) needs to be investigated. We conduct systematic simulations to improve the performance for LE-ERT. If CEM electrodes with realistic borehole diameters are used, meshes with a large number of elements occur, leading to memory exhaustion during simulations. Thus, varying diameters together with different mesh qualities and refinements should note the limitations of electrode discretisation that lead to (a) acceptable errors, (b) the negligible loss of accuracy and (c) a good numerical performance. We consider four 100 m long electrodes with a 100 m spacing in between and a radial dipole-dipole array (Figure 3.4a). The mesh generator TetGen (Si, 2008) is used to generate unstructured tetrahedral meshes. The model space is extended by 3000 m in each direction to prevent influences of the boundary conditions (Rücker et al., 2006). CEM electrodes are included as hollow prisms

with a certain number of facets, for example 6 facets as shown in Figure 3.1. The mesh quality q describes the radius-edge ratio of a tetrahedron. If R is the radius of a unique circumsphere and l the length of the shortest edge of a tetrahedron, then the quality can be calculated by $q = \frac{R}{L}$. Large q-values indicate badly shaped tetrahedrons and thus has to keep small. In the following investigation, q is varied from 1.2 to 1.4. For every q, the electrode diameter is set in a range of 0.05 - 5 m, whereas the number of facets (see Figure 3.1) increases from 3 to 10. A contact impedance of $10^{-6}\,\Omega\mathrm{m}^2$ is assigned to every electrode by equation (3.1a), to ensure a negligible influence of z_L.
A reference model that reflects realistic geometries of metal-cased boreholes available in Northern Germany is chosen. In this case, standard metal-cased groundwater wells with a diameter of $d = 0.05\,\mathrm{m}$ are simulated as a reference. With a mesh quality of $q = 1.2$ and a refinement using quadratic shape functions, a maximum of three facets can be realized. Figures 3.4b and c show the relative deviation of the geometric factor K for different borehole diameters and facets (local refinements) for CEM with linear and quadratic shape functions. The deviations were calculated by:

$$\text{deviation} = \frac{K(d, N_\mathrm{f}) - K_0}{K_0} \cdot 100\%\,, \tag{3.5}$$

where K_0 denotes the reference, and $K(d, N_\mathrm{f})$ denotes the geometric factor for a given diameter d and number of facets N_f.
The modelling shows that the deviations increase with a growing electrode diameter. A slight improvement in the number of facets appears only for the highest d=5 m. Models with smaller diameter show no dependencies on the number of facets; i.e., further local refinement is unnecessary. Even the models with the smallest electrode diameter show deviations of approximately 2% for the finest mesh quality ($q = 1.2$) in Figure 3.4b. By using quadratic shape functions (see Figure 3.4d), the deviation level is reduced for all electrode diameters, and no influence of the number of facets remains.
By varying the mesh quality and using quadratic shape functions, models with the same electrode diameter lead to equal deviation levels; hence, it can be assumed that the deviations for each electrode diameter are dominated by geometric effects. Large electrode diameters reduce the distance between the electrodes and thus decrease the measured potential difference. High deviations of models without a refinement by quadratic shape functions are caused by coarse discretisation. However, small electrode diameters together with a large number of long electrodes lead to meshes that are difficult to handle due to an enormous number of elements.

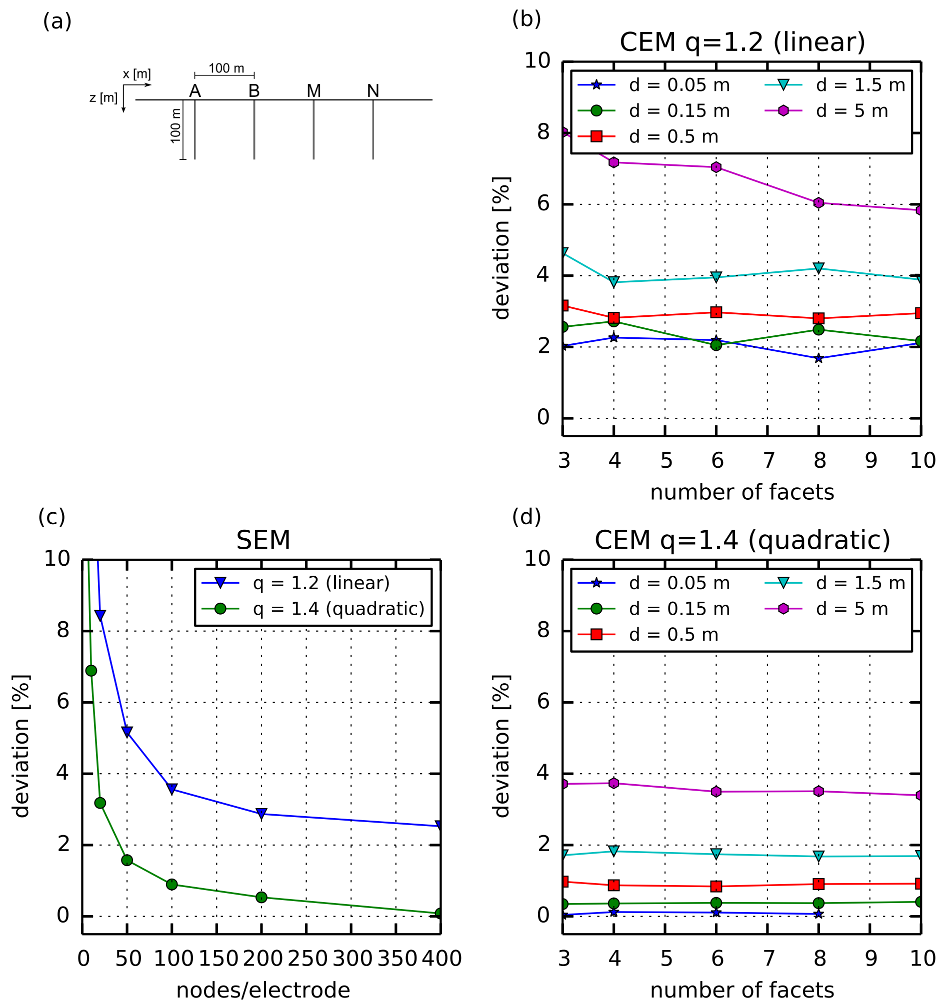

Figure 3.4: Relative deviation of geometric factors for a dipole-dipole array using scheme (a). The electrode diameter d and number of facets are varied using CEM with linear shape functions (b) and quadratic shape functions (d). Deviations depending on the z-discretisation for SEM are given in (c) for linear (blue) and quadratic (green) shape functions.

If SEM is used for modelling, long electrodes (see Figure 3.4c) with a very dense node discretisation in the z-direction (approximately 1 node per meter) is required to achieve errors below 1%. Generally, if numerical errors below 2% are demanded, quadratic shape functions must be used. To avoid errors above 1% due to geometric effects, the electrode diameter should not exceed 0.5 m. Because the results depend on the electrode spacing, the diameter or z-discretisation (in case of SEM) can be increased, as further modelling results show.

3.2.2 Effect of different contact impedances

The contact impedance z_L in Ωm^2 describes how an electrode is galvanically coupled with the subsurface (Rücker and Günther, 2011). Poorly coupled electrodes are usually associated with increased contact impedances; i.e., a higher transmitter voltage is needed to transmit a desired current strength. When conducting four-point measurements, the contact impedance is usually neglected due to the separation of the current and voltage circuits. Nevertheless, for long electrodes, the electric field and thus the measured signal can be significantly influenced by the variation of the contact impedance along the electrodes (Rücker and Günther, 2011).

A current injection using two 100 m long electrodes is simulated to investigate the effect of different contact impedance. Potential distributions and current densities are plotted as 2D slices along the symmetry plane. A homogeneous half-space with a resistivity of $\rho = 1\,\Omega\text{m}$ is assumed. The left electrode is divided into parts assigned with different contact impedances, whereas the other electrode includes one part with a single z_L over the whole length. In Figure 3.5a and Figure 3.5b, a constant low-contact impedance of $z_L = 10^{-6}\,\Omega\text{m}^2$ leads to a constant potential along the electrodes surface, as demonstrated by Rücker and Günther (2011). Accordingly, the current strength is constant, with a primarily horizontal current flow next to the electrode.

The effect of heterogeneous contact impedances along the electrode is shown in Figure 3.5c - Figure 3.5f. The first case in Figure 3.5c and Figure 3.5d, is motivated by an unsaturated zone followed by a groundwater layer. Thus, the electrode is divided into two parts of equal length with different z_L. By increasing z_L up to $10^{-1}\,\Omega\text{m}^2$, almost no current enters the subsurface at the upper part of the electrode. As a result, the current lines are modified in the vicinity of the electrode, which possibly affects the measurement.

The case of a poorly coupled borehole section, caused, e.g., by corrosion along a 10 m portion of the casing, is investigated. The section between 40 - 50 m depth is assigned z_L=10 Ωm^2, whereas z_L remains low (z_L=$10^{-6}\,\Omega\text{m}^2$) for the rest of the casing. As Figure 3.5e and Figure 3.5f show, the effect on potential and current lines is very small. Therefore, small corroded zones with respect to the borehole length do not significantly affect measurement.

Effect of contact impedances on four-point measurements

Because the effect of changing contact impedances depends on the resistivity distribution, a two-layer case with a first-layer thickness of 120 m is considered.

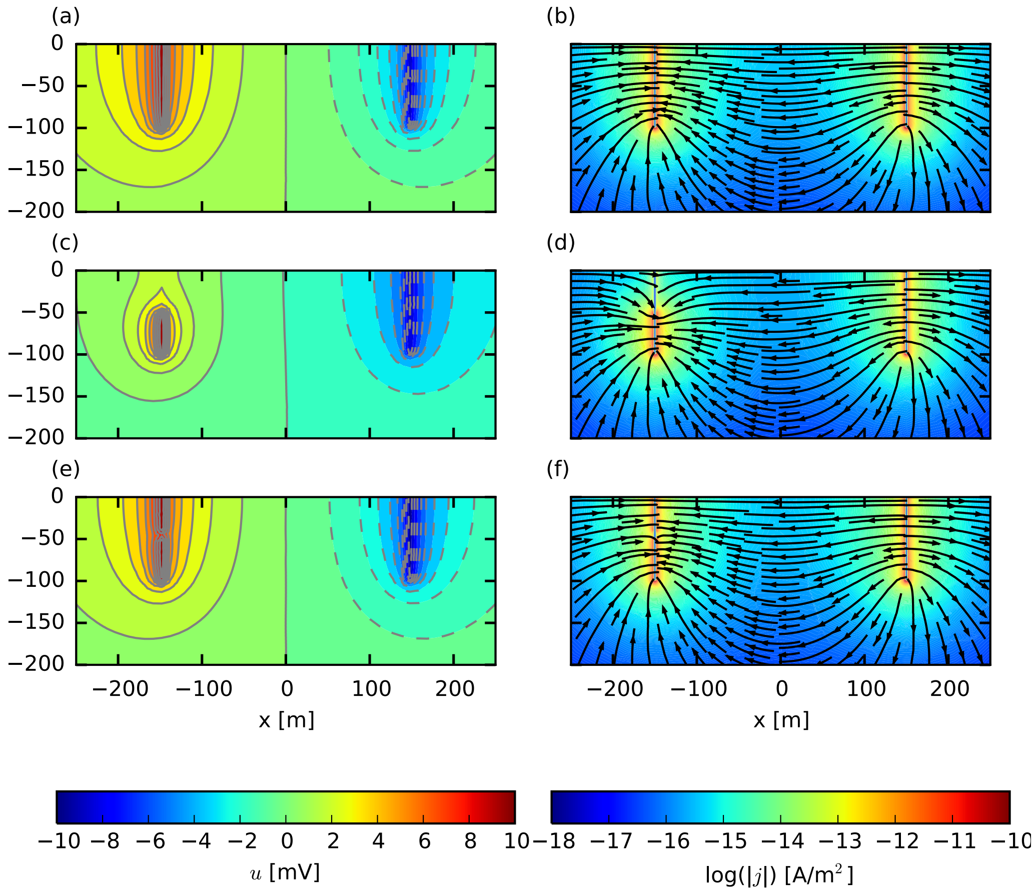

Figure 3.5: Potential distribution (left) and current density (right) for a current injection into a homogeneous half-space with different contact impedances (z_L) for the left electrode. In (a/b) constantly low z_L, (c/d) high z_L between 0 and 50 m depth, (e/f) high z_L between 40 and 50 m depth.

Simulations for a radial Wenner-β array using four 100 m deep electrodes with a 100 m separation are shown in Figure 3.6a. First, the resistivity of the top layer is fixed to 100 Ωm, and the resistivity of the bottom layer increases from 1 Ωm to 10, 20, 50 and 100 Ωm. Second, the resistivities of both layers are exchanged; i.e., the second-layer resistivity is fixed, whereas the top-layer resistivity is varying.

For each model, the red-marked part of electrode A in Figure 3.6a is varied in the range $10^{-6} \leq z_L \leq 10^{6}\,\Omega\text{m}^2$. Because no experiences for the contact impedances of spatially extended electrodes exist, a large z_L range is used, assuming that the actual values are included. The deviation of apparent resistivities by changing z_L towards a reference model, using $z_L = 10^{-6}\,\Omega\text{m}^2$ for electrode A, is observed. Figure 3.6b shows the relative deviation of calculated ρ_a towards the reference model for the given z_L-range.

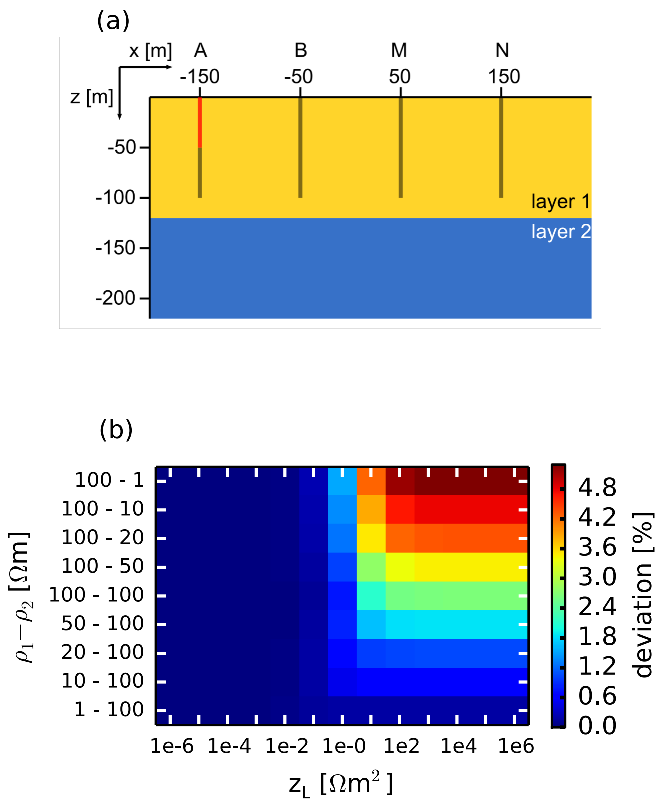

Figure 3.6: The two-layer model used is shown in (a). The relative deviation of simulated voltages for different contact impedances of the upper part (marked red) of the first current electrode for a Wenner-β array. The resistivity of one of the layers in (b) changes between 1, 10, 20, 50 and 100 Ωm, whereas the other one is fixed to 100 Ωm.

The results clarify that deviations for $z_L \leq 10^{-2}\,\Omega\text{m}^2$ are negligible. Regardless of the resistivity contrast, the deviations increase to a maximum level for an increasing z_L. For $z_L > 10^3\,\Omega\mathrm{m}^2$ the deviation towards the reference model remain constant. For low resistivities of the top layer and high contrasts towards the bottom layer, the deviations remain small even for large contact impedances. If the resistivity of the top layer increases and ρ of the bottom layer decreases, the deviations increase up to values of approximately 5%. Generally, the effect of high-contact impedances on LE-ERT measurements becomes more distinct if the resistivity of the subsurface surrounding long electrodes increases.

3.3 Sensitivity of four-point data

To evaluate how resistivity changes in the subsurface affect measurements, sensitivities can be visualized. To derive these dimensionless parameters, we use resistivities as model parameter (m_j), and for the forward response (f_i), we use the apparent resistivity $\rho_{a,i} = K\,U_i/I_i$ by scaling with the geometric factor K. The sensitivity is computed using local element matrices from the finite element formulation, as described by Günther et al. (2006).
Two-dimensional sensitivity slices along the symmetry axis of a dipole-dipole array for different electrode lengths with 200 m dipole spacing and 50 m dipole length are shown in Figure 3.7. Electrodes are included as cylinders with a length of either 100 m or 50 m, three facets and a diameter of $d = 2\,\mathrm{m}$ or as surface points electrodes. All sensitivities are calculated for a homogeneous half-space with a resistivity of $\rho = 1\,\Omega\mathrm{m}$.
The well-known sensitivity distribution for a dipole-dipole array with surface electrodes is given in Figure 3.7a. If long electrodes are used (see Figure 3.7b), the sensitivity distribution is shifted into greater depth. More importantly, the lateral variation of sensitivities is almost constant down to the electrode bottom. According to Figure 3.5a and Figure 3.5b, this can be explained by a uniform electrical field that occurs as a result of the elongated electrodes and an integrated voltage measurement over the whole electrode length. Due to high sensitivities between the electrodes, anomalies will have a strong effect on measurement. However, a correct vertical localization is not possible within the depth range of homogeneous sensitivities, as deduced by Rucker et al. (2011b) from modelling.
If several potential (or current) electrodes are shortened or even reduced to points, as shown in Figure 3.7d-e, the sensitivity distribution obtains lateral gradients between the dipoles. Obviously, some vertical resolution between the dipoles can be regained if different lengths or surface electrodes are used. In all other sensitivity distributions shown, dipoles can be observed as a superposition

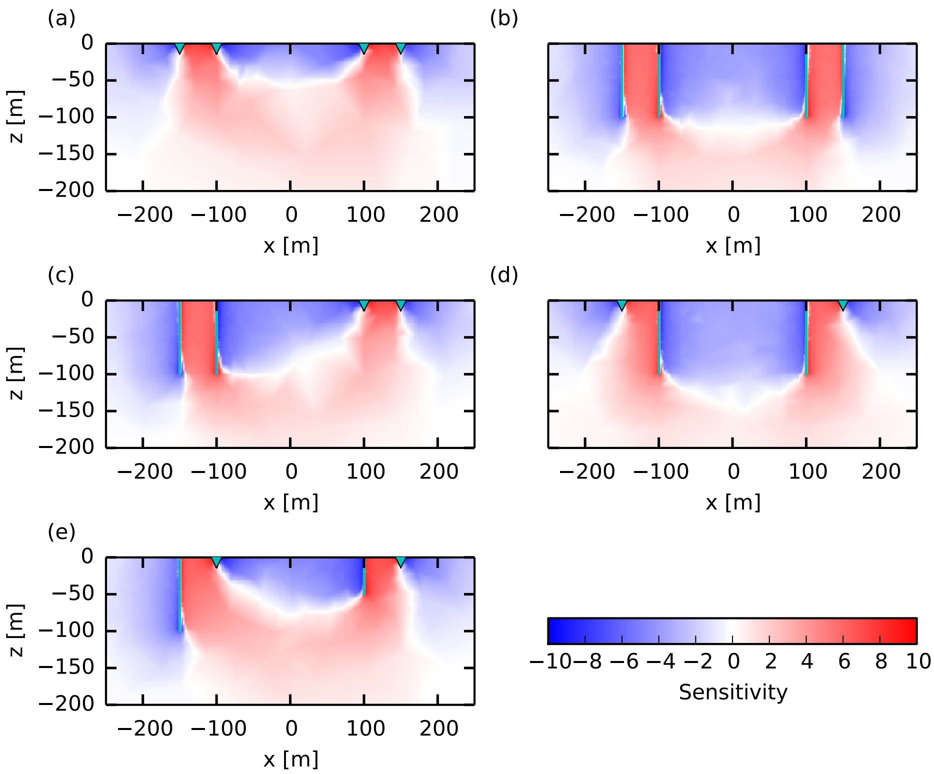

Figure 3.7: Sensitivity distributions of a dipole-dipole array for different electrode lengths. Surface electrodes are marked with triangles.

or variation of the first two (with surface electrodes and four long electrodes). For example, the region outside both dipoles in Figure 3.7d is exactly the same as in Figure 3.7a (surface electrodes), and the sensitivity distribution between current and potential dipoles corresponds to the inner part of Figure 3.7b, regardless of interpolation errors of 3D sensitivities, shown as 2D slices. In Figure 3.7e, an enhancement of vertical resolution is observable either inside or outside the electrode configuration. In general, a combination of long and short or point electrodes for current and potential dipoles is expected to increase both horizontal and vertical resolution. Ideally, long and short electrodes should be alternated to obtain the best enhancement of the vertical resolution.

3.3.1 Impact of simple resistivity models

Simple scenarios are generated to simulate a vertically and horizontally moving low resistive anomaly, e.g., a saltwater front in a homogeneous half-space. Synthetic data for different four-point arrays are calculated for inhomogeneous resistivity distributions.

We investigate the effect of a moving low resistivity edge on the apparent resistivities of radial and equatorial four-point measurements using long electrodes

and point electrodes. The electrodes are arranged in a regular grid of two rows, each consisting of seven 100 m long electrodes with a 100 m spacing each. For comparison, the same geometry is modelled using a point electrode model (PEM). For all models, the resistivity of the moving layer is set to 10 Ωm, and the homogeneous half-space has a resistivity of 100 Ωm. Geometric factors are calculated numerically for a homogeneous half-space using CEM for long electrodes. The geometry and models are schematically shown in x/z- and x/y-plane in Figures 3.8a-b and Figure 3.9a-b.
The intrusion front depicted in Figure 3.8a is located at a depth of 280 m and rises in steps of 2 m with an infinite extension in x-, y- and partially in z-direction.

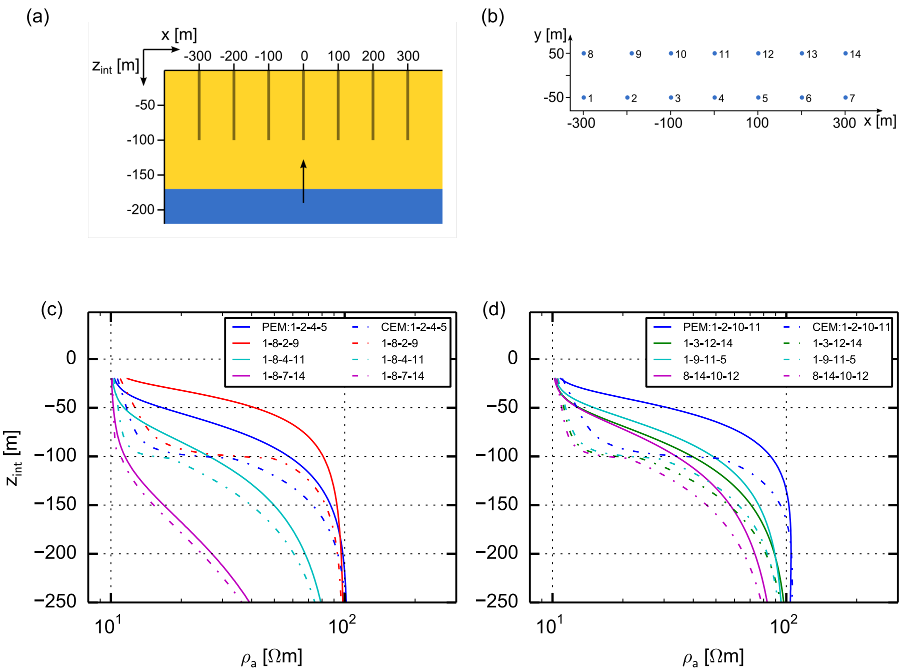

Figure 3.8: A scheme of an emerging intrusion in x/z-plane is shown in (a), with an x-y view of electrode positions in (b). Modelled apparent resistivities ρ_a for standard radial/equatorial dipoles (c) and shifted and rotated dipoles and a Wenner configuration (d), using surface electrodes (solid lines) and 100 m long electrodes (dashed lines).

The development of apparent resistivities for the vertically rising intrusion front is shown in Figure 3.8c and Figure 3.8d using point electrodes and equally long electrodes. The electrode numbering given in the legend corresponds to the numbering in Figure 3.8b using the scheme A-B-M-N, whereas the current electrodes are denoted with A, B and the potential electrodes with M, N. As expected, the apparent resistivity decreases for the rising conductive layer. In accordance with the latter simulation, the curves of long electrode measurements (dashed line) are influenced earlier than point electrode measurements (solid line) due to the enhanced investigation depth.

For small dipole distances like configuration 1-8-2-9 in Figure 3.8c, the investigation depth is more influenced by the electrode length, leading to larger ρ_a-differences between point and long electrodes. Configuration 1-8-7-14 in Figure 3.8c indicates that ρ_a-curves for point and long electrodes become more similar with an increasing dipole distance. The configuration 1-9-11-5 in Figure 3.8d is a layout variation of 1-8-4-11 in Figure 3.8c, where both dipoles are rotated in x/y-plane. The comparison between the two configurations shows that 1-9-11-5 exhibits a more slightly decreasing ρ_a as the conductive layer passes the electrode bottom. In general, if the conductive anomaly passes the electrode bottom, ρ_a decreases according to the sensitivity distributions of the individual configurations. A further rise in the anomaly leads to only small ρ_a changes for long electrodes, which is a result of the poor vertical resolution. According to sensitivity distributions shown in Figure 3.7, an enhanced vertical resolution can be obtained by using electrodes with different lengths.

Apparent resistivities for a horizontally moving conductive front are shown in Figure 3.9c and Figure 3.9d. According to the model (Figure 3.9a) the front is shifted in steps of approximately 4 m for $x_{\text{int}} \in [-502, 502]$ at a $z = -120$ m depth with an infinite extension in y- and a negative z-direction.

As the conductive front moves towards the electrode grid, the apparent resistivity decreases for all arrays. The slight increase of ρ_a at the beginning of some configurations is caused by negative sensitivities. For large x_{int}, i.e., when the conductive layer reaches the right side of the model, a constant ρ_a level appears for all arrays according to their individual sensitivity distributions.

As expected, the apparent resistivity values that form arrays with the largest dipole spread (1-8-7-14) are most affected by the conductive layer. Moreover, it exhibits the smallest differences between point and line electrodes as the depth penetration is already obtained by the large separation. In contrast, arrays with small separation and thus a small penetration show large differences between point and long electrodes. All configurations with long electrodes exhibit the same behaviour as point electrodes but are much more pronounced. This fact can be explained by the shifted sensitivity distributions into greater depth.

A rotation of one dipole (comparison between 1-2-4-5 and 1-2-4-12) does not lead to significant changes for this resistivity distribution. If both dipoles are rotated in opposite directions (1-9-11-5 compared with 1-8-4-11), the effect of the anomaly on ρ_a decreases. Nevertheless, all arrays show that the ρ_a curves

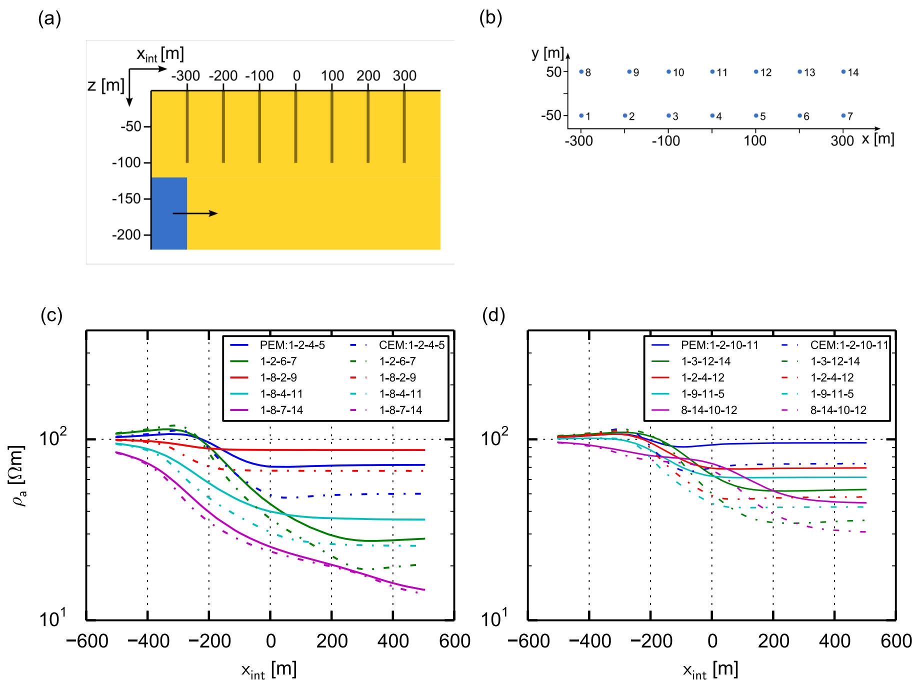

Figure 3.9: (a) x/z-plane of the resistivity model for a moving block ($x \in [-\infty, x_{\text{int}}]$, $y \in [-\infty, \infty]$, $z \in [120, \infty]$) in x-direction. Calculated apparent resistivities ρ_{a} as a function of intrusion position (x_{int}) for standard arrays radial/equatorial dipoles (b) and shifted-, rotated-dipoles and a Wenner configuration (c) using 100 m long electrodes (dashed lines) and surface electrodes (solid lines).

of long electrode measurements are more affected by the low-resistive anomaly than surface-electrode arrays. This finding verifies the assumption of increased penetration depth by the long electrode method.

3.4 Inversion and resolution of multi-electrode data

Multi-electrode data are simulated to appraise the resolution of a 3D long electrode survey on a realistic target. A model is chosen according to the typical geologic conditions for an inland saltwater intrusion (see Figure 3.10). We assume a two-layer case with an interface at a 100 m depth. The upper layer is considered an aquifer with an average resistivity of 200 Ωm, whereas the second lower layer is assigned 50 Ωm and will simulate an impervious layer. A conductive anomaly (white outline) with a thickness of 40 m lies directly on top of the second layer and is located in the lower-left corner of the electrode array with an extension of $x \in [-450, 50]$ and $y \in [-250, 50]$. Electrodes are distributed on a regular 5×3 grid with a spacing of 100 m in x- and y-direction.

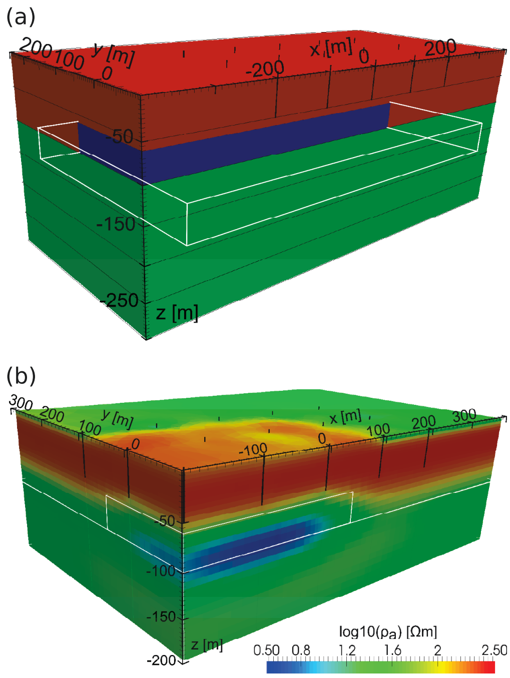

Figure 3.10: Synthetic model (a) with two layers (red, green) and a conductive anomaly (blue with white outline). A grid of 5 × 3 50 m deep boreholes is assumed (black). The inversion result using CEM is given in (b) with a white contour lines marking the anomaly and the interface between layer 1 and 2.

Standard two-inch groundwater wells are assumed to be used. Three different borehole lengths are also taken into account. The first model uses surface electrodes (PEM). In the second case, 50 m-long CEM electrodes are used, and in the third model, 50 m- and 25 m-long CEM electrodes are arranged alternating in a checkerboard style. Although a regular grid of long electrodes is realistic only for small scales, we use it because it is the most general electrode set-up. A possible application could be a monitoring of a contamination plume under known hydrological conditions. Under consideration of the accuracy results, synthetic data are generated on sufficiently fine tetrahedral meshes.
Synthetic data are calculated for all possible 4085 four-point combinations. Although the number of independent data is much smaller, we like to be independent on the specific choice of combinations and their sensitivity to noise. The simulated data are contaminated with Gaussian noise using a standard error of 2% plus a voltage error of 100 μV. Combinations with errors exceeding 5% and absolute geometric factors larger than 10^5 m are removed, resulting in approximately 3500 data.

Inversion of the synthetic data was achieved using a smoothness-constrained minimization (Günther et al., 2006) as described in chapter 2. For estimating a discretisation-independent resolution measure, Friedel (2003) suggested computing a resolution radius for each model cell using its volume V_{Cell}, resulting in the radius of an equivalent, perfectly resolved sphere

$$r_j = \left[\frac{3V_{\mathrm{Cell}}}{4R^M_{j,j}\pi}\right]^{\frac{1}{3}} \quad . \tag{3.6}$$

A triangular prism mesh was used for inversion. In all results we, used a relative vertical weight (Coscia et al., 2011) of 0.05. The parameter domain is about 50% larger than the maximal electrode spacing. It appears that a smaller parameter domain (i.e. a boundary with 20% of largest electrode spacing) leads to artefacts of the inversion, resulting in an additional vertical shift of the anomaly. This finding coincides with the findings of Maurer and Friedel (2006) that outer-space sensitivities should be taken into account. According to accuracy tests, the electrode diameter should not exceed 0.5 m for CEM, which leads to a large inversion mesh with 137 730 cells. The large number of cells is still manageable for inversion, but it restricts the computation of resolution matrices. If SEM is used, significantly less numerical effort is necessary. As the electrode diameter is neglected, a coarser horizontal and finer vertical discretisation is possible, producing an inversion mesh of 17 600 cells, and resolution matrices can be easily computed.
The inversion result using CEM is given in Figure 3.10b. For a better observation of the mapped anomaly, the inversion result is clipped at $y = -100$ m and $x = -200$ m. The interface and the anomaly of the underlying synthetic model are added as white contour lines. The anomaly can be traced up to the surface, where a considerably higher resistivity occurs, which implies a good horizontal localization. The depth level of the anomaly's top is also well resolved. A transition zone between 50 - 80 m appears until a resistivity of approximately $\rho = 6\,\Omega$m for the anomaly is reached, which leads to a slight downward shift into the second layer. In general, the inversion of synthetic data, the use of CEM leads to reasonable results and is able to resolve the interface between the two layers and the anomaly.
The resistivity images and resolution radii for three different electrode sizes in the SEM approach are compared in Figure 3.11. In all results, the interface at 100 m depth is determined well, despite a vertical shift, which is greatest for the surface electrode set-up. The 40 m thick anomaly can be resolved with a correct lower boundary but with different resistivities and extensions. The

surface-electrode array in Figure 3.11a shows the greatest difference in shape and resistivity towards the given anomaly. The depth level of the top can be determined, but due to the incorrect resistivity, a distinction of the anomaly from the second layer is not possible. This finding is validated by the corresponding resolution radii distribution in Figure 3.11b. Large radii appear for depths larger than 50 m (at the anomalies' top) and from 30 - 40 m at the boundaries of the area, indicating a poor resolution. In contrast, the depth, thickness, location and resistivity of the anomaly are better resolved if 50 m-long electrodes are used, as indicated by the result shown in Figure 3.11c. However, compensation artefacts appear below a 120 m depth. The corresponding resolution radii in Figure 3.11d show improved resolution in deeper regions, leading to a better resolved anomaly.

By using electrodes of different length, depicted in Figure 3.11e, the anomaly is resolved as well as with equally long electrodes (Figure 3.11c). Despite that, the corresponding resolution radii given in Figure 3.11f show a slightly improvement at the surface but significantly worse at depth.

The most important benefit of using electrodes with different lengths becomes clear if the conductive anomaly is shifted into the depth range of the boreholes. Therefore, the geometry of the underlying model is modified by shifting the interface up to a 70 m depth and the anomaly up to a depth range of 30 - 70 m. The inversion results for 50 m-long electrodes and an alternating arrangement of 50 m- and 25- m long electrodes using SEM is shown in Figure 3.12, including the underlying model as white outlines.

In cases of equally long electrodes (Figure 3.12a), the anomaly is not visible, although its depth range exceeds the electrode length. This finding underlines the interpretation of an almost lost vertical resolution in the depth range of the electrodes. By using 50 m- and 25 m-long electrodes alternatively arranged as in Figure 3.12b, the anomaly is well resolvable due to the enhanced vertical resolution. Although the conductive anomaly has reached the lower part of the long electrodes, a spatial characterization using electrodes with different length is possible.

3.5 Conclusions

Long electrodes can be accurately discretised by three different models. Simulations reveal that CCM and CEM lead to identical solutions for the same electrode geometry. The only difference is that CEM does not discretise the borehole interior. CEM represents the most general model for approximating

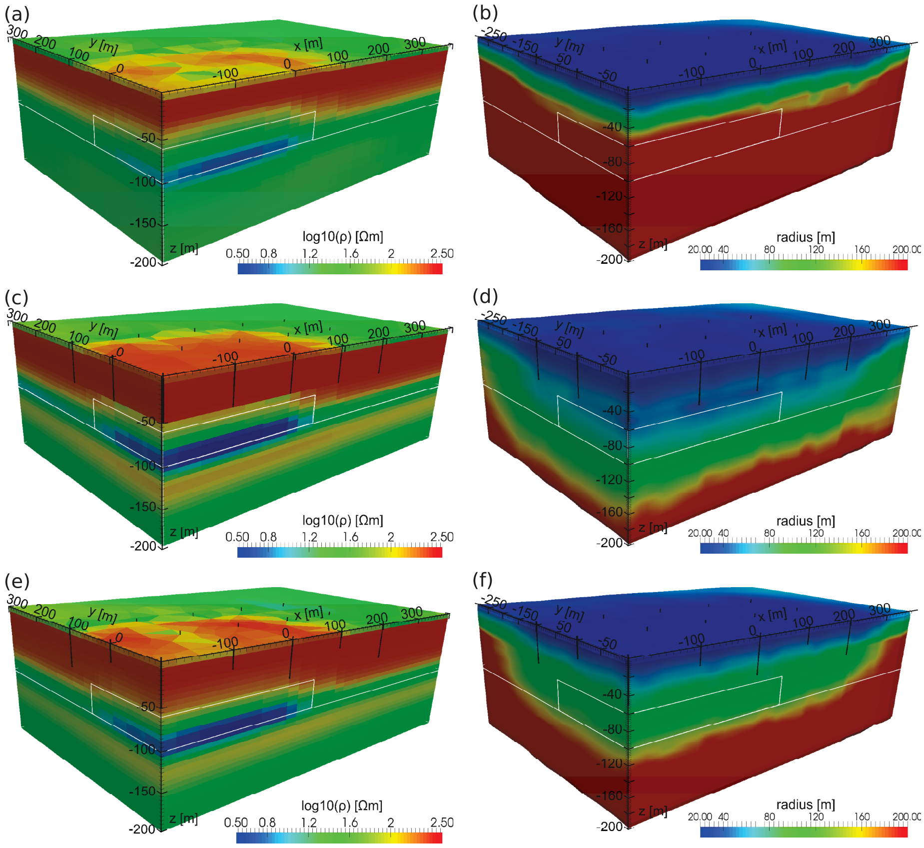

Figure 3.11: Inversion result of a two-layer case (interface at 100 m depth) with conductive anomaly at 60 - 100 m depth using (a) surface electrodes, (c) 50 m long SEM electrodes, (e) 50 m and 25 m long SEM electrodes (alternately arranged). The resolution radii for (a), (d) and (e) are shown in (b), (d) and (f), respectively.

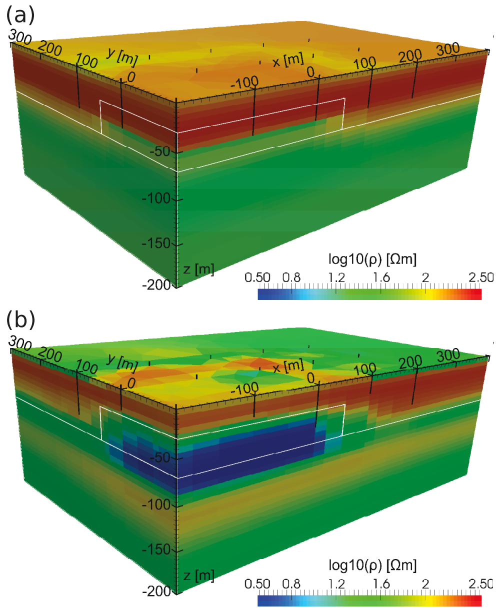

Figure 3.12: Inversion result for a two-layer case using (a) only 50 m long electrodes and (b) 50 m and 25 m electrodes (alternately arranged). The interface between the two layers was set to 70 m depth and the conductivity anomaly at 30 - 70 m depth. The underlying model is given as white contour lines in both inversion results.

reality as it describes the whole system by incorporating contact impedances. Long and thin boreholes can also be modelled using SEM with a significantly lower numerical effort. In general, finite element solutions with quadratic shape functions are recommended. In cases of CCM or CEM, the electrode diameter limits the coarseness of forward model meshes. The studies reveal that for thin electrodes, the ratio of diameter and spacing should not exceed 1% to keep the numerical error below 1%.

In most applications, contact impedances are considered negligible for LE-ERT measurements, which is not necessarily true. Varying contact values can significantly affect the potential and current distribution, leading to systematic deviations for measured voltages. However, the synthetic case of differently coupled electrode parts covering a large range of contact impedances shows that deviations rarely exceed 5%.

Sensitivity distributions are important for understanding resolution properties. In cases of equally long electrodes, the vertical resolution is almost lost in their depth range, as concluded by other researchers. However, electrodes of different lengths or long electrodes in conjunction with surface electrodes can recover a significant part of the lost resolution.

Simple resistivity models based on lateral saltwater scenarios show that conductive bodies can be detected when still far from the electrodes. Similar results can be expected for resistive anomalies, which usually lead to larger anomalies. Long electrodes significantly increase the depth of investigation for small dipole separation.
For accurate forward modelling, CEM and CCM demand small borehole diameters that lead to huge meshes, even for a small number of electrodes. In contrast, SEM leads to a coarse lateral discretisation due to the approximation of long electrodes to a number of nodes. Because it only requires a dense vertical discretisation for small electrode distances, SEM is the recommended method for incorporating long electrodes into meshes for LE-ERT data inversion, if the electrode diameter is negligible. As it reduces the degree of freedom in inversion, it enables model resolution analysis. Pure forward calculations are most efficiently conducted on fine tetrahedral meshes. For inversion in 1d-dominated settings, meshes consisting of vertically oriented triangular prisms are recommended due to their easier application of vertical constraints and the reduced numerical effort required.
Long electrode arrays significantly improve the imaging quality for deep targets compared to equivalent surface electrode arrays. Resolution radii are in the range of borehole distances and decrease rapidly with depth. Arrays with different electrode lengths improve the model resolution. The inversion results of synthetic models clearly show that resistivity anomalies within the depth range of long electrodes cannot be imaged. Only LE-ERT measurements combining electrodes of different lengths are capable of imaging these anomalies. Because the choice of casings is normally given, we recommend adding surface electrodes to measurement designs. In general, LE-ERT surveys will use only a limited number of electrodes and hence reduce the model resolution compared to common ERT surveys. Nevertheless, LE-ERT measurements with appropriate field designs are able to deliver large-scale resistivity information of the subsurface that cannot be achieved by standard ERT.

4 Laboratory experiments

4.1 Introduction

The second stage for developing a monitoring system using long electrodes are laboratory experiments under controlled conditions. The aim is to conduct time-lapse measurements to obtain (a) experiences in data processing, (b) interpretation and (c) to test arrays that are optimised to provide a maximal information content with a low effort. Two experiments were conducted that simulate different scenarios for saltwater intrusions. The first one simulates a coastal region to observe the influence of sea level fluctuations on a typical saltwater wedge. Different scenarios were monitored using a common 2D ERT set-up with surface electrodes. Photographs were taken during the whole monitoring for comparison. Time lapse data sets with a high temporal resolution were generated that map significant and visually observable resistivity changes. A second experiment was designed simulating a horizontal moving saltwater body. An ERT monitoring was conducted using a 2D surface layout with long electrodes that allows to image the 3D resistivity distribution.

4.2 Physical experiment to simulate saltwater intrusions at coastal areas (2D)

4.2.1 Experiment description

A 2D physical experiment was conducted within a 200 cm long, 50 cm high and 5 cm wide acrylic tank. A cross-section of a coastal aquifer was simulated using filter sand with a grain diameter of d $\approx$ 0.7 - 1.2 mm. The tank was filled to a height of 30 cm, whereby the slope down to the offshore part starts at about 1.5 m. Drippers and electrodes were arranged alternately. The experiments were conducted with tap water (density of 1000 kg/m^{-3}) and saltwater with a density of 1025 kg/m^3. Movements of the saltwater-freshwater interface were visualised by using different tracer dyes (e.g. Uranine and Eosine), colouring the freshwater yellow and the saltwater red. The experimental set up is shown in Figure 4.1.

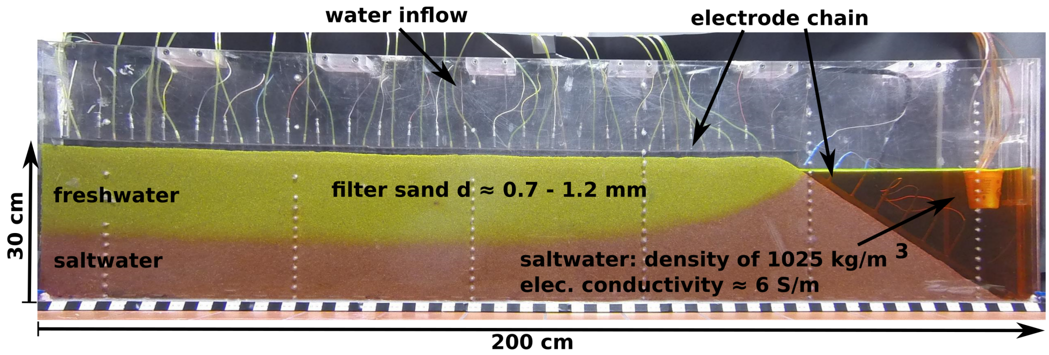

Figure 4.1: Experimental design for simulating the movement of a saltwater - freshwater interface in coastal regions. It demonstrates a slice perpendicular to a coast line, whereby the saltwater red-coloured and the freshwater yellow-coloured.

The ERT monitoring was conducted using 32 surface point electrodes with a 6 cm spacing in between. Seven electrodes were placed at the slope beneath sea level in order to increase the model resolution, because the saltwater-wedge is formed in this part that leads to important resistivity changes for the conducted experiments. At the initial state the model was saturated with saltwater to a height of 30 cm. Starting from this initial condition, three different experiments were conducted successively.

1st experiment: freshwater was recharged by drippers at the onshore part of the model until equilibrium was reached, i.e. the saltwater-freshwater wedge was in steady-state.

2nd experiment: the freshwater recharge rate was reduced, to simulate a smaller freshwater head

3rd experiment: the saltwater level was increased slightly above the top of the aquifer for about 5 minutes, simulating a saltwater inundation. After the saltwater front moved through the aquifer a steady-state was reached again.

A standard Schlumberger configuration was used for ERT monitoring. Altogether, 947 time steps were measured with 225 data points each. The measurement of a single ERT time step took about 2.5 minutes. During the monitoring photographs were taken every 30 seconds.

4.2.2 2D/3D hybrid inversion

Finite-element meshes for modelling 2D ERT data are usually three dimensional, while the inverse modelling is done on 2D meshes. This is because the current sources are always 3D and must be treated accordingly. For forward calculations, the 2D finite-element mesh used for inverse modelling is going to be extended perpendicular to the survey direction (3D).
In the case of laboratory measurements, the tank walls influence the electrical field, which has to be taken into account in the forward calculation. An unstructured 2D mesh was generated, which was extended perpendicular to the profile direction (y-axis) up to the tank dimensions. The mesh used for inversion is shown in Figure 4.2. Consecutive cells in y-direction were assigned with the same parameter, which prevents resistivity variations in y-direction in the model domain. Because the resistivity of the off-shore part of the model is assumed to be homogeneous, it is treated as a single region, which allows only one resistivity value for this part. To prevent interactions between the off- and on-shore part, marked red and grey in Figure 4.2, both regions were decoupled from each other.

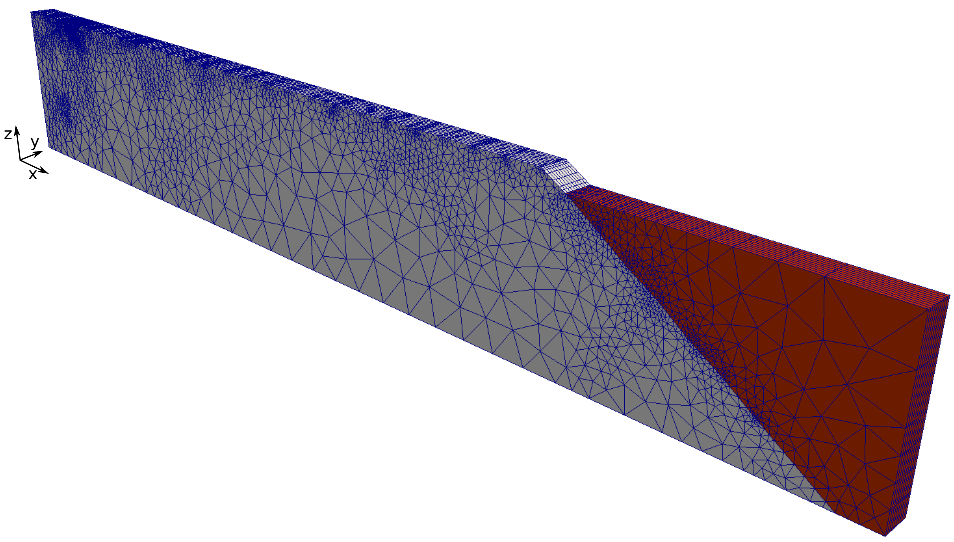

Figure 4.2: Finite-element mesh for data inversion. Cells in y-direction are assigned with the same marker to prevent resistivity variations. The red coloured part is set to a single region, allowing only one resistivity value.

4.2.3 Monitoring results

As no reciprocal measurements were available for an error estimation, an error model with 1% Gaussian noise was used. Combinations with errors exceeding 10% were removed. A smoothness-constrained time-lapse inversion was done as described in section 2.4.1.
The regularisation factor (see equation 2.23) was manually adjusted varying in the range of $100 \leq \lambda \leq 1000$ to obtain a good data fit. For quality control of the inversion the χ^2 value after equation 2.20 was used. Data are fitted within their errors if $\chi^2 \approx 1$ is reached. Best results were achieved with a temporal regularisation of $\lambda_t = 50$ between subsequent time steps. Variations in the saltwater domain were prevented by confining the model parameter to $0.16\,\Omega\text{m} \leq \|\rho\| \leq 0.17\,\Omega\text{m}$. The homogeneous resistivity distribution of the initial state and the known electrical fluid conductivity enables the determination of formation factors for the whole model domain. An average resistivity of about $\rho = 0.15\,\Omega\text{m}$ was calculated and the inverse used as bulk conductivity σ_b. The electrical fluid conductivity of $\sigma_f = 6.4\,\text{S/m}$ was measured for the saltwater. By using equation 2.3 a formation factor of $F = 5.1$ was calculated and used to convert the bulk resistivity of all following time steps into fluid conductivities σ_f. The first experiment is shown in Figure 4.3 with photographs on the left column and corresponding inversion results of the ERT monitoring at the right column. The top panel shows the initial state and the bottom panels the end of the experiment.
The emerging interface between saltwater and freshwater can be imaged correctly by the ERT monitoring results. The elapsed time to the current time step in Figure 4.3 indicate that the interface moves slower towards the end of the experiment. The depth of the interface decreases towards the left tank wall, which is caused by a poor model resolution due to a lower data density. Fluid conductivity variations occur within the saltwater body at the second time step (after 22 min are elapsed) shown in Figure 4.3. These are unexpected and appear only in this time step. The density contrast between the freshwater and saltwater in conjunction with the slow fluid movement leads to a sharp interface with a vanishing diffusive zone, which can be shown by hydraulic modelling. Thus, saltwater that is not directly at the interface (freshwater-saltwater) should not be affected by freshwater and vice versa. Furthermore, this behaviour does not appear for other time steps shown and thus is assumed to be artificial.
Although the photograph for the time step after 453 min in Figure 4.3 shows just a thin layer of saltwater at the bottom of the tank, the impact on the

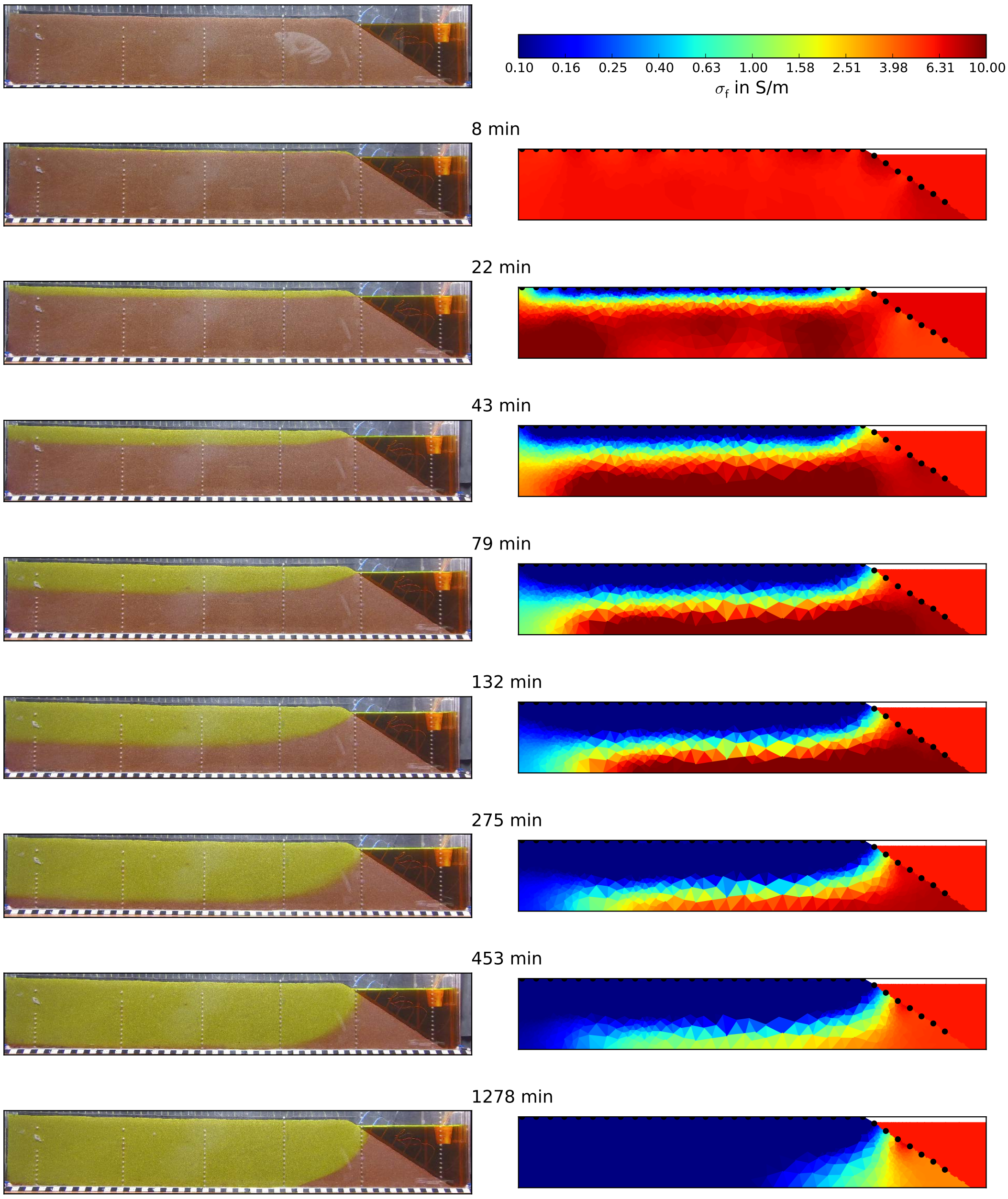

Figure 4.3: Inversion result for the irrigation of a saline aquifer with freshwater. The left column shows photographs and the right the corresponding ERT inversion result of the time steps with the elapsed given in the title. The saltwater affected part is marked with by a red tracer and the freshwater part by a yellow one (experiment 1).

fluid conductivity distribution is still large. The final time step shows the typical steady state of the saltwater wedge. The sharp interface cannot be resolved by the ERT monitoring result. Compared to earlier time-steps, the fluid conductivity decreases at the saltwater part, which is not expected. Both could possibly be explained by a worse model resolution.
The decreased freshwater recharge rate in the second experiment leads to a reduced water head, which results in the movement of the saltwater wedge as shown in Figure 4.4.

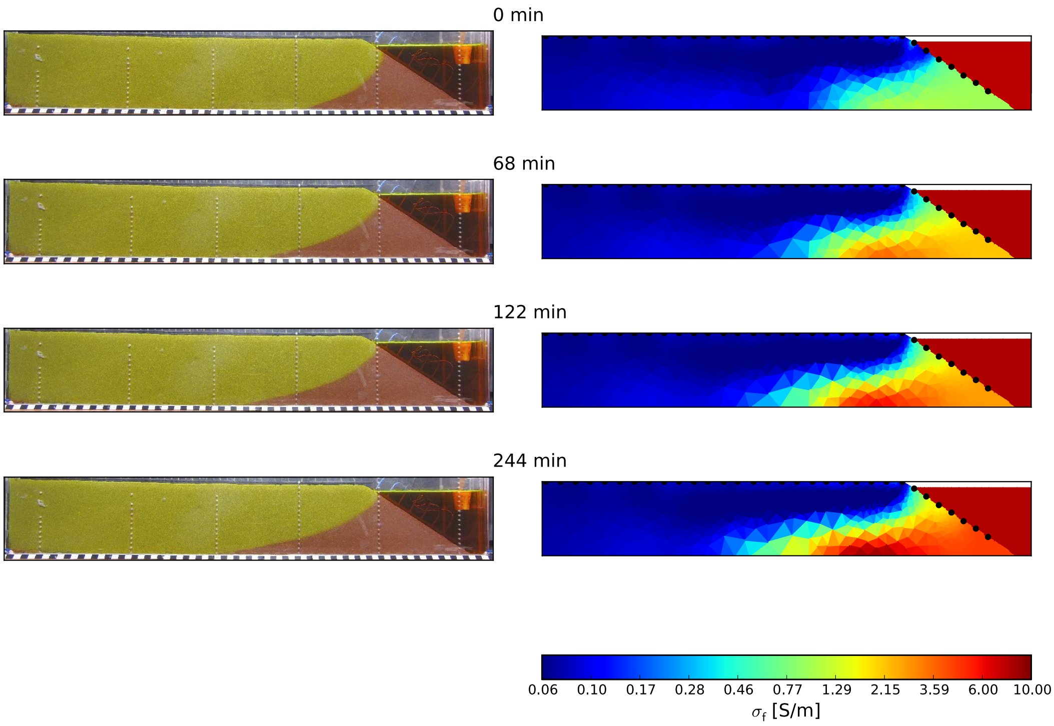

Figure 4.4: Photographs are shown on the left and corresponding inversion results on the right column for the second experiment where the freshwater recharge rate was reduced.

Although the model changes, which occur at the photographs, are rather small, the ERT monitoring is capable to image the movements of the saltwater wedge. Nevertheless, an increasing fluid conductivity of the saltwater body appears, which is again an unexpected artefact.
The results of the third experiment are shown in Figure 4.5. Due to the rising saltwater table, the model geometry is changed constantly. To take that into account, new meshes with slightly different geometries that consider the saltwater table are needed for every time step during the inundation. The used software does not consider different finite element meshes during the inversion process. Due to the wrong model geometry, strong pronounced artefacts appear in the fitted conductivity distributions. Accordingly, these time

steps were excluded from the time-lapse inversion because the artefacts lead to misinterpretations. The first time step in Figure 4.5 shows the model directly after the saltwater inundation and all following time steps the movement of infiltrated saltwater.

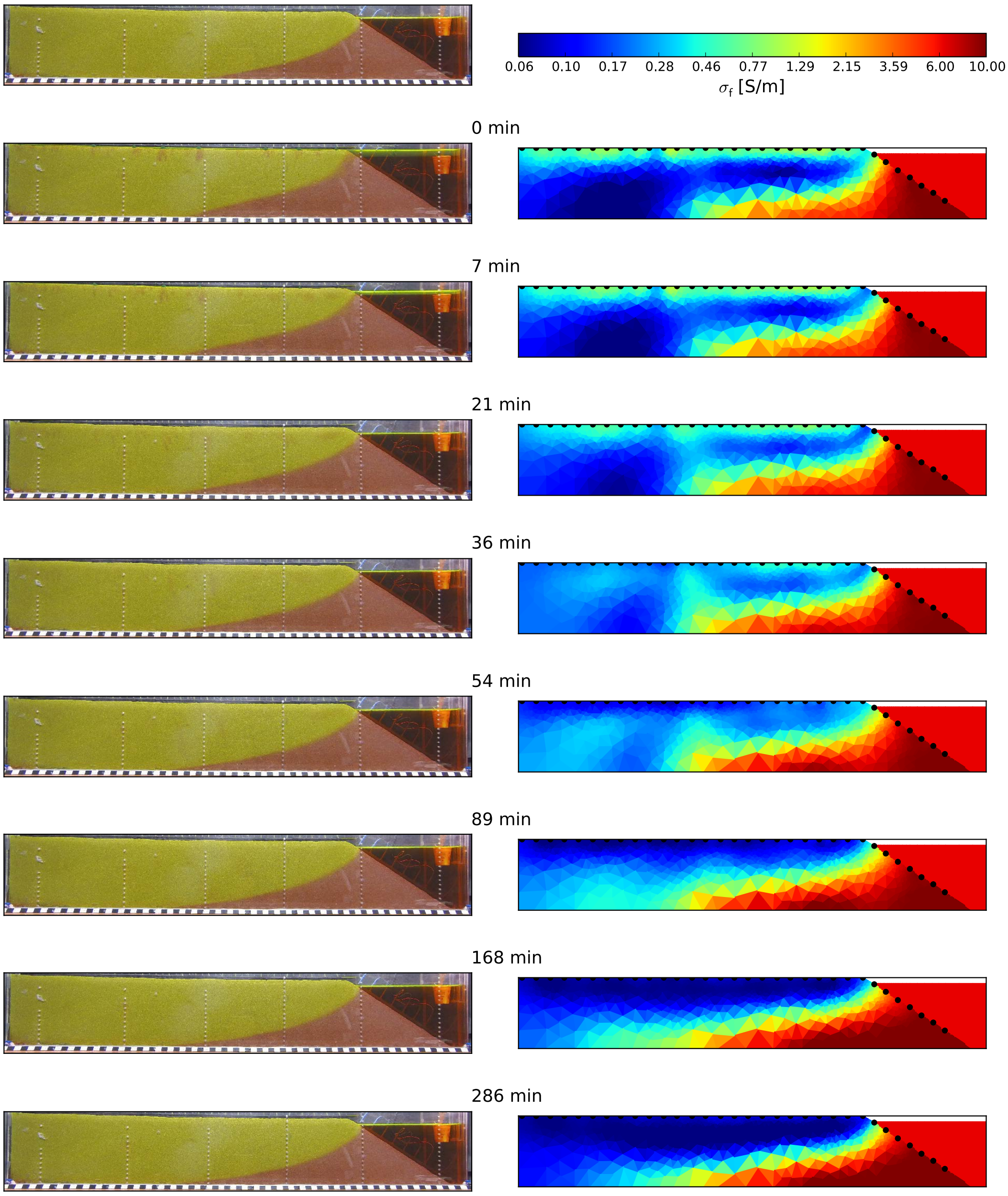

Figure 4.5: Monitoring results of the inundation experiment, with photographs at the left, corresponding ERT inversion results at the right column.

The percolating saltwater is scarcely visible in the photographs after 0 min on the left side of Figure 4.5. Preferential flow paths might be an explanation, which could be a result from the trickling water through the installed dripper.

The main part of the saltwater could migrate through these flow paths and cannot be monitored by the photographs. On the contrary, the ERT results are able to resolve the percolating saltwater. It appears more like a moving diffusive zone of higher conductivities rather than a sharp saltwater front.

4.3 Physical experiment to simulate the movement of a saltwater front (3D)

4.3.1 Experiment description

The second experiment is a 3D LE-ERT monitoring, conducted in a 90 cm long, 75 cm wide and 45 cm high tank, shown in Figure 4.6. The tank consists of three chambers. The large main chamber in the middle is detached from the small side chambers by perforated walls. Due to different pressure heads in both side chambers controlled and temporal constant fluid movements can be realised. Influences of these both side chambers on an ERT measurement were not taken into account, but could be possible. The effect on time lapse measurements are expected to be small, because the resistivity of the fluid in the side chambers is constant for the whole monitoring. The tank was filled with filter gravel with a grain diameter of d $\approx$ 0.7 - 1.2 mm of two different mining areas with differing colours. Observations revealed a different hydraulic behaviour between the upper and lower part of the tank, which is most likely caused by an increased packing density from the top to the bottom. The experiment was conducted using tap water with a fluid conductivity of about $\sigma_f = 45\,\text{mS/m}$ and saltwater with a $\sigma_f = 450\,\text{mS/m}$. The saltwater was coloured with a trace dye (Uranine) to visualize the fluid movements.
A difference of 1 cm between the water tables of the right and left chamber was adjusted to generate a pressure difference that enables fluid flow from the right to the left side in the main chamber of the tank.
For the initial state of the monitoring, the tank was fully saturated with fresh water. One experiment was conducted consisting of two different stages.

1. stage: saltwater, coloured by a yellow dye tracer, was injected into the right chamber to generate a horizontally moving saltwater front until the main chamber was saturated

2. stage: freshwater was injected on the right side to replace the saltwater.

The conducted experiment was monitored with ERT using twelve electrodes that were arranged on a regular 3×4 grid as shown in Figure 4.6b. Stainless

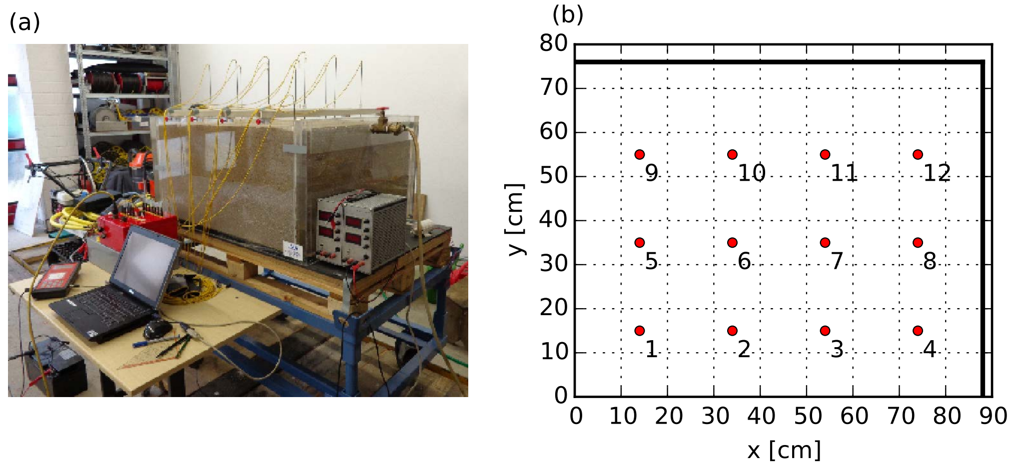

Figure 4.6: Experimental set-up for 3D ERT monitoring with long electrodes (a). The electrodes are arranged on a regular grid shown in (b).

steel rods, each with a length of 21 cm were used to simulate long electrodes. For conducting the ERT monitoring an optimised set of dipole combinations was calculated.

4.3.2 Optimisation process

If no constant resistivity distribution can be assumed for every single time step a temporal smearing with motion blur can lead to misinterpretations of the ERT monitoring results. Especially for laboratory experiments, fast resistivity changes can occur that limits the time to measure a single time step. A reduced data set has to be used in order to save time, rather than a time consuming comprehensive data set. An optimisation process was used that reduces a comprehensive data set on the base of the data resolution matrix $\mathbf{R}^D$, which is calculated according to section 2.5. By eliminating dipole combinations with a low information content, the input data set will be successively reduced. Synthetic data calculated on the base of a homogeneous half-space were used as input for the optimisation algorithm.

A truncated SVD, as explained in chapter 2, of the data-weighted Jacobian $\mathbf{J}$ was used to calculate the data resolution matrix $\mathbf{R}^D$ (described in section 2.5). The information content IC of the whole data set can be calculated by summing up the diagonal elements of $\mathbf{R}^D$ (see equation 4.1).

$$\mathrm{IC} = \sum \mathrm{diag}(\mathbf{R}^{\mathbf{D}}_{\mathbf{ii}}) \tag{4.1}$$

At the start, the Jacobian matrix for all possible 4-point combinations is used as input. Firstly, a truncated singular value decomposition was carried out. The threshold for removing the null-space (see section 2.5) was set to $0.001 \cdot s_1$, whereas s_1 is the first singular value. Afterwards, the data resolution matrix was calculated. For eliminating dipole combinations, the median of diag($\mathbf{R}^D$) was used as a threshold. All combinations with an information content below that threshold were discarded. Finally, the Jacobian matrix and the data are updated and used as the input for the next iteration step. In every iteration, the sum of the diagonal elements of $\mathbf{R}^D$ is calculated in order to obtain the information content (IC) for this set of dipole combinations. The behaviour of the IC from update to update helps to decide, which data set would be a good compromise between the loss of information content and amount of dipole combinations. A schematic sketch of the optimisation process is shown in Figure 4.7.

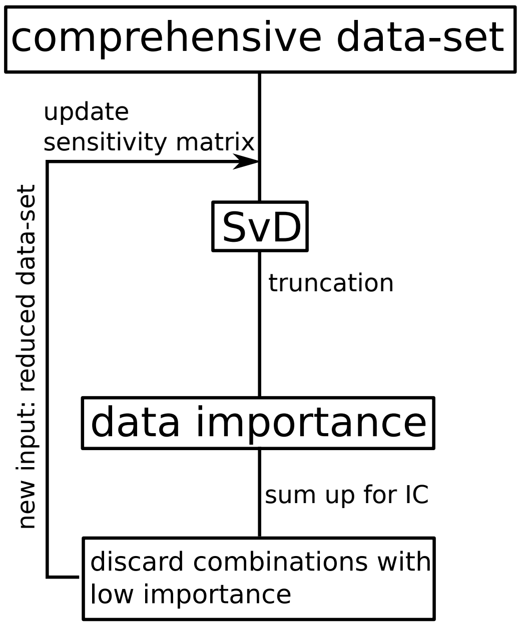

Figure 4.7: Schematic work-flow of the optimisation algorithm

A comprehensive data-set with n=12 electrodes consists of 1485 different dipole combinations. Note that only $\frac{n(n-3)}{2}$ independent four-point configurations exist (Xu and Noel, 1993), which equals the maximum information content. The result of the optimisation algorithm is shown in Figure 4.8.

The maximal information content of IC = 54 for twelve electrodes is not reached, because of the truncated SVD. With just a small loss of information content, the amount of dipole combinations can be reduced down to about 140. As Figure 4.8 shows, slightly changed curve shapes can be obtained by

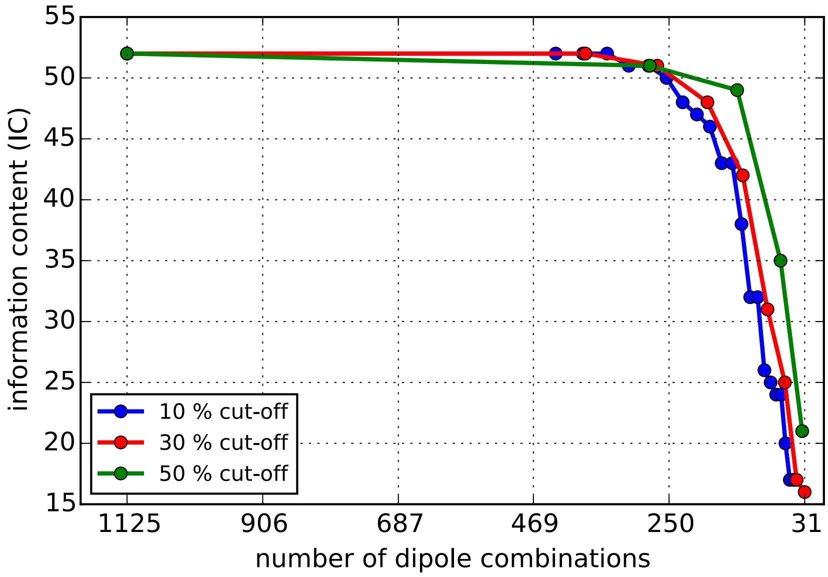

Figure 4.8: Dependence of the information content (IC) form the amount on dipole combinations. For the data cut-off 50%, 30% and 10% thresholds were used.

using different thresholds for reducing the data set. As the iteration step i is influenced by the previous one, the information content decreases slightly faster for small thresholds. Although all curves in Figure 4.8 show comparable results, it can be expected that small thresholds enable to determine a more precise location of the point of rapidly decreasing information content.

4.3.3 Raw data and data processing

To generate an optimised set of dipole combinations, the median (50%) of the information content was used as a threshold within the optimisation algorithm described above. Dipole combinations with a high geometric factor were discarded from the start. Although these combinations exhibit high importances, their significant lower voltage makes them susceptible for noise and difficult to measure. An optimised data-set with 70 dipole combinations was used, because the estimated hydraulic conductivity coefficient of K = 0.006 m/s indicates a highly permeable material that demands fast ERT measurements. A measurement of a single time step took two minutes with the given dipole set. The monitoring was conducted with the 8-channel RESECS instrument. An error model of 5% Gaussian noise was used. The observed raw-data for the whole monitoring are shown in Figure 4.9, in which every vertical line denotes a single time step.

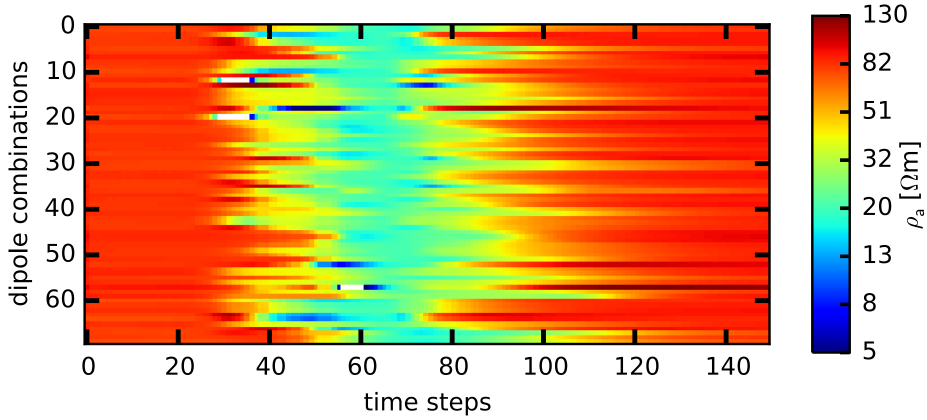

Figure 4.9: Apparent resisitivities (ρ_a) of the 3D laboratory experiment for all time steps.

The apparent resisitivities show that the intruding saltwater front starts to influence the raw-data at about time step 30. According to their position and sensitivity distribution some dipole combinations are affected earlier than others. At about time step 70, the recharge of the tank with fresh water starts, which reduces the apparent resistivites again. At late times, approximately after time step 120, the whole tank is almost filled with fresh water. Some dipole combinations still show reduced ρ_a values, which might be caused by saltwater remained at small pores. Negative ρ_a appear as white horizontal lines in Figure 4.9 and can be assigned to combinations 12, 20 and 57. As geometric factors are calculated on the base of a homogeneous half-space, the high resistivity contrast and sharp interface between fresh and saltwater distorts the electric field such that the geometric factor and measured resistances has opposite signs. These dipole combinations were discarded for data inversion, leaving 67 data as inversion input.

Systematic errors due to configuration, position and/or discretisation errors can influence time-lapse inversion results by increasing the error-level that leads to larger misfits. LaBrecque and Yang (2001) suggest a scheme based on Occam's inversion technique. The differences between the base-line and subsequent data sets is used as the inversion input, rather than data sets themselves as shown by:

$$
\begin{aligned}
&\Delta D = (d_{obs} - d^0_{obs}) - [f(m) - f(m^0)] \\
&d_{obs} \rightarrow d_{obs} - [d^0_{obs} - f(m^0)] \\
&\text{because of log-transformed ERT data:} \\
&\log(d_{obs}) \rightarrow \log\left(d_{obs} \cdot \frac{f(m^0)}{d^0_{obs}}\right)
\end{aligned} \tag{4.2}
$$

In the functional 4.2, d^0_{obs} denote the base-line data, $f(m^0)$ the forward response of the base-line and d_{obs} the data of the current time step. The key point of this approach is that noise, corrupting data, can be split up into a part ϵ_s that is correlated between temporal consecutive data-sets (systematic errors) and an uncorrelated part ϵ_n. By using differences, the systematic part ϵ_s will be removed, whereas the error-level of the uncorrelated part is eventually increased. Because ERT data are always log-transformed, the product of the observed data with the misfit of the base-line is used. For more details see LaBrecque and Yang (2001).
The finite element mesh shown in Figure 4.10 consisting of about 16,000 prism elements was used for data inversion. Long electrodes were simulated using the SEM described in section 3.2. The red spheres shown in Figure 4.10 mark the SEM nodes forming the long electrodes.

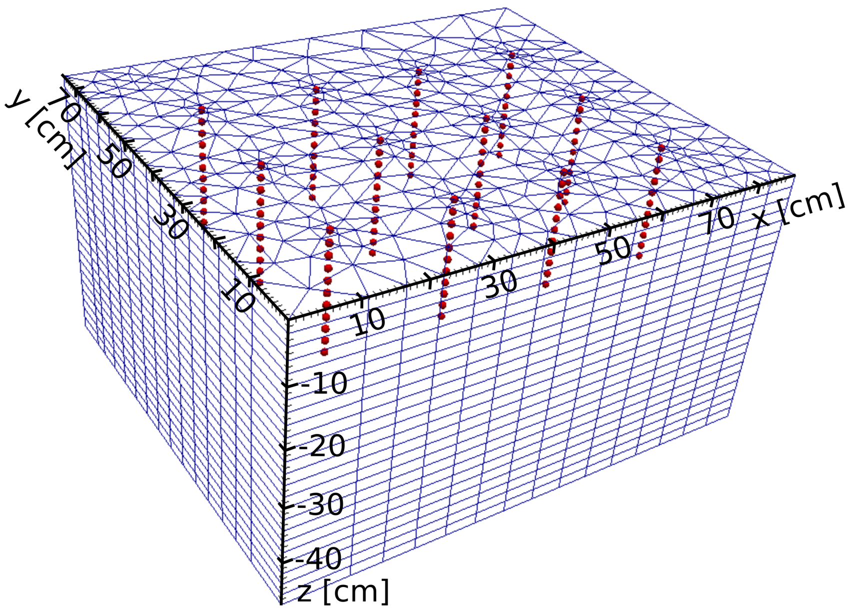

Figure 4.10: Finite-element mesh for data inversion using the tank dimensions. SEM electrodes are marked with red spheres.

Their length was approximated with eleven nodes using a 2 cm spacing in between. A geometric refinement was done by inserting an additional node

1 cm next to every electrode in x-direction. Inversion of the time-lapse data was done using a smoothness-constrained minimization (Günther et al., 2006).

4.3.4 Monitoring results

At first, the base-line was fitted separately to obtain a model that reflects the reality sufficiently well and to explain the measured data, i.e. a small misfit. As a quality criterion for the different inversion approaches shown, the error weighted misfit between the forward response $f(\mathbf{m})$ and the data $\mathbf{d}$ was used. According to equation 4.3 it is calculated for every time step k.

$$\mathsf{misfit}_k = \frac{f_k(\mathbf{m}) - \mathbf{d}_k}{\epsilon_k} \tag{4.3}$$

In case of the difference-inversion scheme, the data for subsequent time steps changes to $\log(d_{obs}) \to \log\left(d_{obs} \cdot \frac{f(m^0)}{d^0_{obs}}\right)$ (see equation 4.2). The fraction $\frac{f(m^0)}{d^0_{obs}}$ is simply the misfit of the first time step or of the base line measurement. In order to take account for the changed data input for the difference-inversion, the misfit calculation for subsequent time steps changes to

$$\mathsf{misfit}_{k,diff} = \frac{f(\mathbf{m}_k) - \mathbf{d}_k * \mathsf{misfit}(\mathbf{d}_0)}{\epsilon_k} \tag{4.4}$$

For the first time step a smooth model can be expected due to the homogeneous resistivity distribution of the freshwater saturated tank. To fit the data within their errors, an algorithm was used that changes the regularization parameter λ automatically. It conducts different inversions while λ is successively decreased, until $\chi^2 = 1$ is reached.

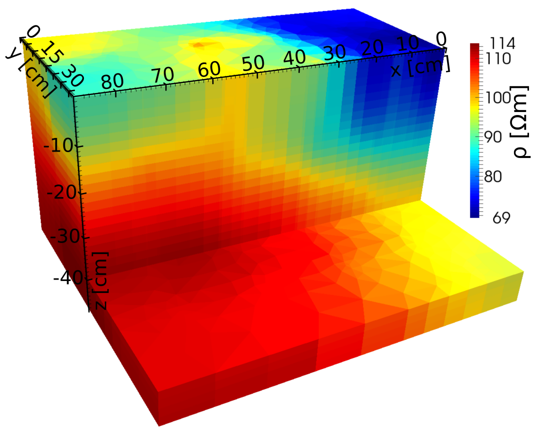

Figure 4.11: Inversion result of the first time step using a χ^2-optimised λ. A data fit of $\chi^2 = 0.94$ was reached.

The result given in Figure 4.11 is fitted with $\chi^2 = 0.94$ using $\lambda = 7.8$ resulting in a maximum misfit (calculated after equation 4.3) of 2.25. Although the data are fitted well, the obtained resistivity range of $69\,\Omega\text{m} \leq \rho \leq 113\,\Omega\text{m}$ for the model parameter is unexpected large, which is unrealistic for a freshwater saturated tank. After adjusting the regularisation factor manually, λ was fixed to 500 to fit the base-line data-set. The result is shown in Figure 4.12a.

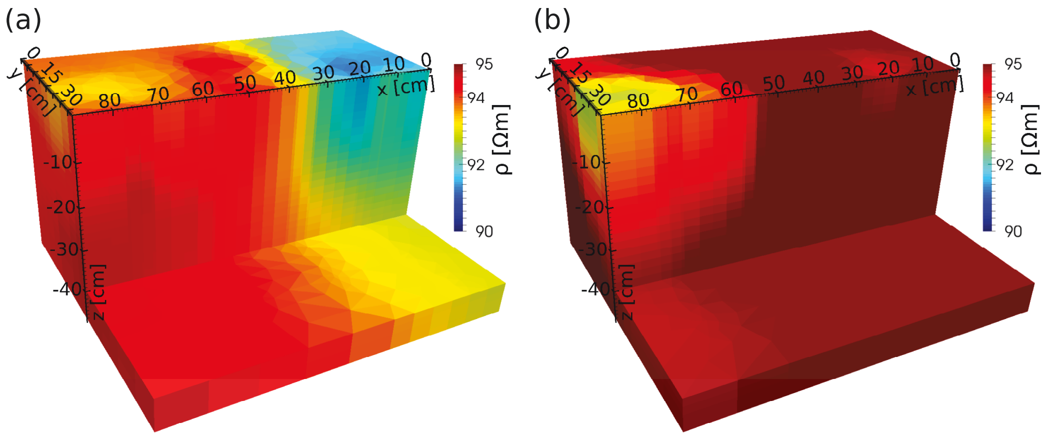

Figure 4.12: Results of the separately inverted datasets of the (a) first and (b) last time step.

With a χ^2-value of 3.2 and a maximum misfit of 5.1, this data fit is a bit worse compared to the first inversion result, which is caused by an increased regularisation factor. Nevertheless, the model shows now the nearly expected homogeneous resistivity distribution, with a ρ-range between 91-95 Ωm for a freshwater-saturated tank. According to this, the regularisation was always fixed to $\lambda = 500$ to fit the base-line in the time-lapse inversion. Additionally, the result of the last time step with the same parameter settings is given in Figure 4.12b. A comparatively equal ρ-range appears for the model of the last time step, showing slight differences between the two distributions.
The first time step (Figure 4.12a) shows lower resistivities towards x = 0, at the right side of the tank, which is most likely caused by the adjacent saltwater chamber. In comparison, the last time step (Figure 4.12b) show the lowest resistivities on the left side, where the saltwater was washed out, indicating that still some traces of saline water might be trapped or left in small pores.

Several time-lapse inversion schemes were used with different combinations of parameter settings for data fitting. The temporal regularisation λ_t to control the smoothness between the time steps (see section 2.4) was switched between a fixed and a χ^2-optimised. Furthermore, the difference and standard inversion

scheme, different base-line data-sets and the time-lapse-step (TLS) approach, described in section 2.4 were used.
Although the χ^2-optimization lead to an unrealistic model for a single-time step inversion, it can provide some benefit in time-lapse inversion, where the smoothness between the base-line and the current time step is taken into account and not the model-smoothness itself.
If the freshwater-saltwater interface moves through the tank, the fitted models need to be more structured, which was considered by fixing λ_t to 40. In addition a second inversion using an optimised λ_t was conducted that terminates the inversion if $0.75 \leq \chi^2 \leq 1.25$ is reached. The χ^2-distributions of both time-lapse inversions are shown in Figure 4.13.

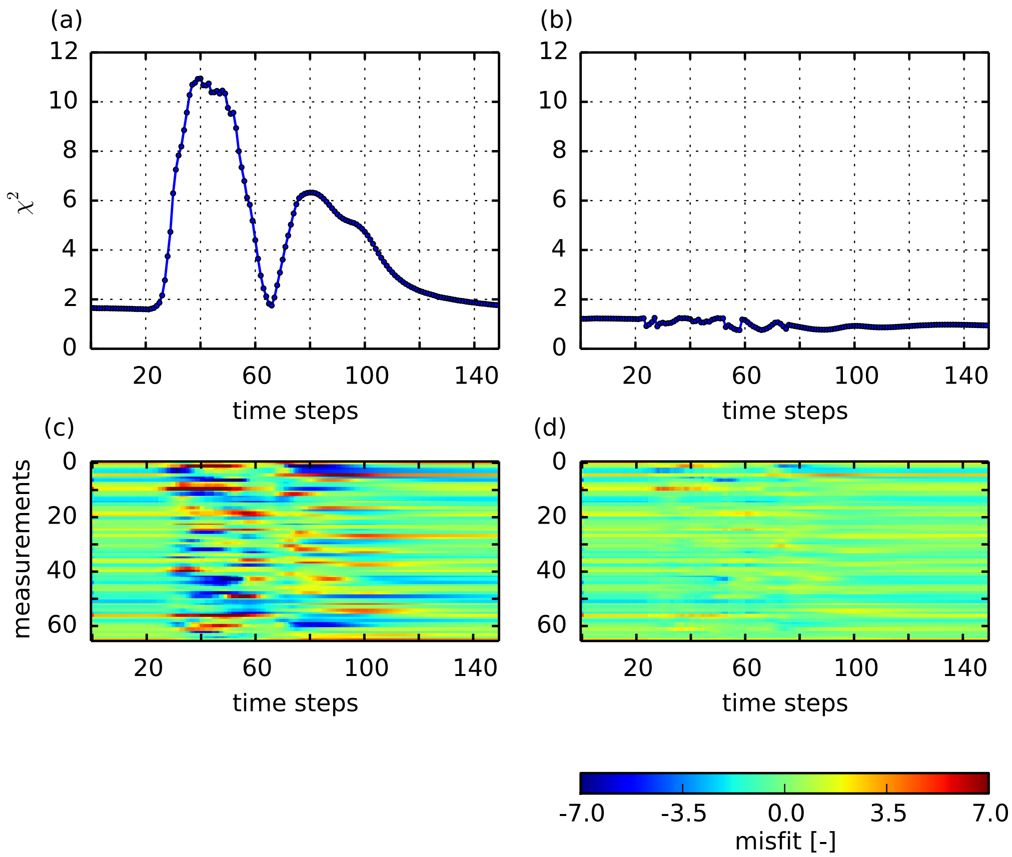

Figure 4.13: χ^2-distributions of the time-lapse inversion with the first time step as base-line using (a) a fixed λ_t, (b) a χ^2-optimisation and their corresponding misfits in (c) and (d).

The χ^2-distribution for a fixed λ_t in Figure 4.13a shows a bimodal distribution with low χ^2 values at the start. This indicates a good data fit, if no significant model changes appear. With χ^2 values up to 11 a poor data fit is reached for heterogeneous resistivity distributions, i.e. the emerging freshwater-saltwater wedge. Only the saltwater saturated state at time step 70 and time steps over

120 (mostly freshwater saturated tank) show low χ^2 values again. According to Figure 4.13c higher misfits occur for heterogeneous resistivity distributions, i.e. for the moving freshwater-saltwater interface (approx. time steps 30 - 120).
As expected, the χ^2-optimised inversion fitted the data within their errors with an optimised λ_t of about 8 - 10 for most time steps. If saltwater enters the tank (time steps 30-60) λ_t is reduced to 3. The corresponding misfits in Figure 4.13d show a more homogeneous distribution over the whole data-set with a lower misfit-level compared to Figure 4.13c.

For time-lapse inversion, a good data-fit of the base-line is vital. Larger misfits can be propagated to subsequent time steps, which may increase their misfits too. If the data-fit of the current base-line does not satisfy the requirements, a possible solution is to change the base-line to another time step. Although the fitted models of the first few time steps show all homogeneous resistivity distributions, the model of the very first time step differs slightly from the other. The variations between fitted models starting at the second time step are very small. According to the constant resistivity distributions for time steps with k ≥ 2, the time-lapse inversion was repeated with the second time step as base-line in order to reduce misfits in Figure 4.13c that might occur by using an unfavourable base line. The results of the standard- and difference-inversion using a fixed temporal regularisation of $\lambda_t = 40$ and the second time step as base line are shown in Figure 4.14.
The misfit and χ^2-distributions in Figure 4.14 show that no improvements of the data fit could be obtained. In this case, using the second time step as base-line does not necessarily lead to better results and thus does not improve the inversion results. Actually, the misfit seems to be increased. Thus, the first time step was set again for all following time-lapse inversions that use a fixed base-line.

To account for systematic errors, the difference inversion scheme was used with the first time step as base-line. Like before, a fixed and an optimised λ_t was used. Their χ^2- and misfit-distributions are shown in Figure 4.15.
Compared to the standard inversion (Figure 4.13a) lower χ^2-values appear for the first time steps in Figure 4.15a. The corresponding misfit distribution (Figure 4.15b) shows lower misfits for specific configurations over subsequent time steps (horizontal stripes), indicating that systematic errors are removed. Results of the χ^2-optimised inversion show no significant improvements due to the difference-inversion.

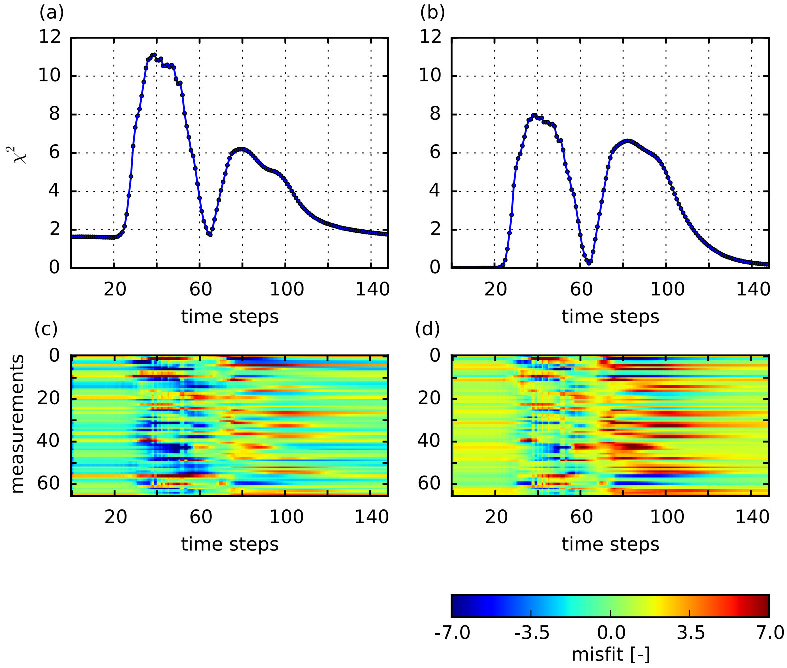

Figure 4.14: Misfit and χ^2-distribution using the second time step as base-line for a standard (a), (c) and difference (b), (d) inversion using $\lambda_t = 40$ (fixed).

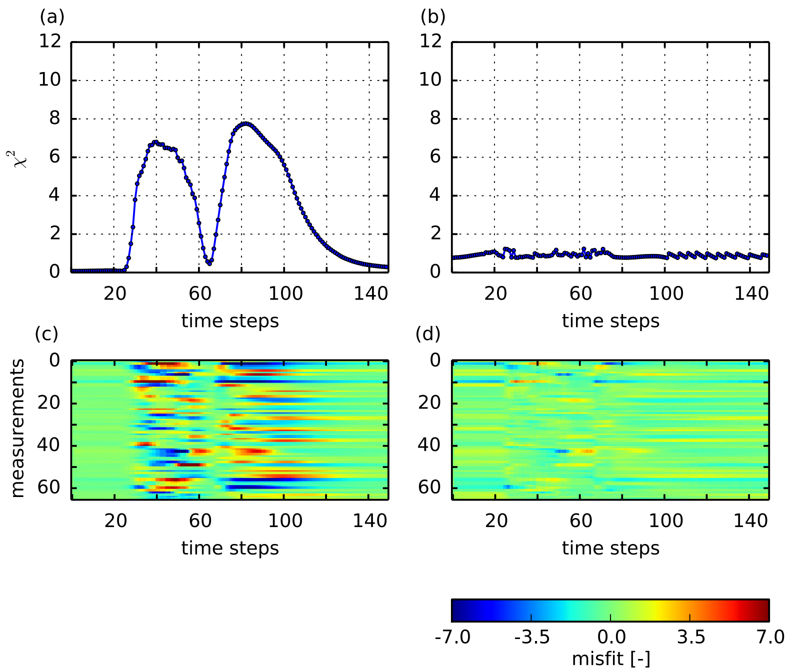

Figure 4.15: χ^2-distributions of a difference inversion scheme using the first time step as base-line with (a) a fixed and (b) a χ^2-optimised λ_t and their corresponding misfit distributions (c) and (d).

Generally, the error-weighted misfits of the difference and standard inversion show the same levels, which indicates that the systematic error part of the time-lapse data-sets is quite low.
By using the TLS approach, the previous time step is used as the base-line. If the difference inversion is applied, the misfit of the first time step is used, while the base-line changes. If misfits of subsequent time steps are used, uncorrelated errors are summed up resulting in a higher error level. Figure 4.16 shows the data fit for a standard and difference inversion with the TLS approach.

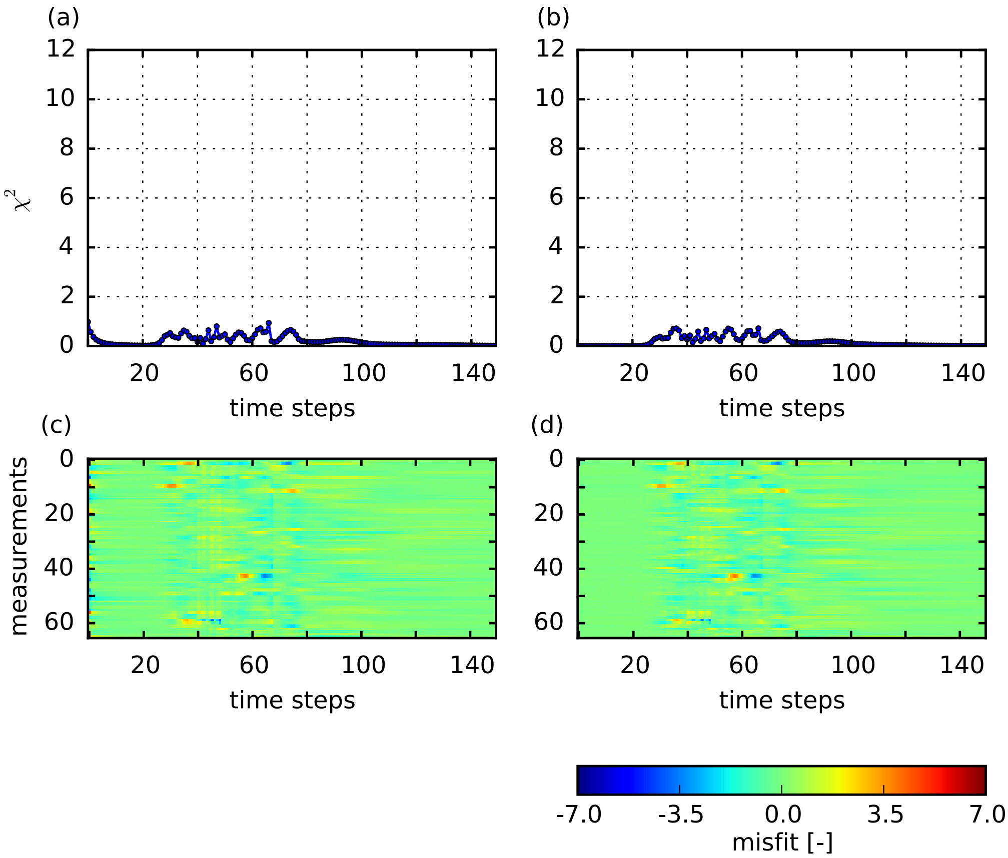

Figure 4.16: χ^2 and misfit distribution of a standard inversion (a, c) and difference inversion (b, d) using the TLS approach with a fixed λ_t.

The misfit-distribution in Figure 4.16c shows a lower level, compared to all inversions using the first time step as base-line (Figure 4.15). Furthermore, the misfit does not increase for a heterogeneous resistivity distribution, i.e. intruding saltwater. If the TLS approach is used, no further improvements can be obtained by the difference inversion shown in Figure 4.16b and d.
Several inversions were conducted in order to image the saltwater intrusion process. In the following, the fitted resistivity distributions for different inversion parameter settings shown, in order to compare their imaging properties.

According to the misfit- and χ^2-distributions for each data fit, the following sets for inversion showed the best data-fit:

(1.) standard inversion with a fixed λ_t and the TLS approach (Figure 4.16a and c),

(2.) difference inversion with a fixed λ_t and the TLS approach (Figure 4.16b and d),

(3.) difference inversion with a χ^2-optimised λ_t (Figure 4.15b and d).

Results of three different inversion approaches of the 3D laboratory experiment are shown in Figures 4.17 and 4.18, with photographs including their time-stamp in the first column. The column numbers on top of Figure 4.17 identifies the used parameter setting according to the list above. The corresponding models for the first two inversions (in the second and third column) using the TLS approach show very structured results. Unreasonable resistivity variations appear (see Figures 4.17 and 4.18) in almost every fitted time step. Time-steps between 57 min and 103 min in Figure 4.17 show decreasing resistivities in freshwater-parts of the model, which are not yet affected by the saltwater. These artefacts appear at the upper part of the model from approximately 0 - 20 cm depth, which equals the depth range of the electrodes. The low vertical resolution in this model part prevents the exact vertical localisation of anomalies as shown in chapter 3. It is possible that these artefacts could be a compensation because the estimated resistivity of the saltwater body is to low. These are, depending on the inversion scheme, more or less pronounced. The strongest artefacts appear in the second and third column, which show the results of the first and second inversion scheme, listed above.

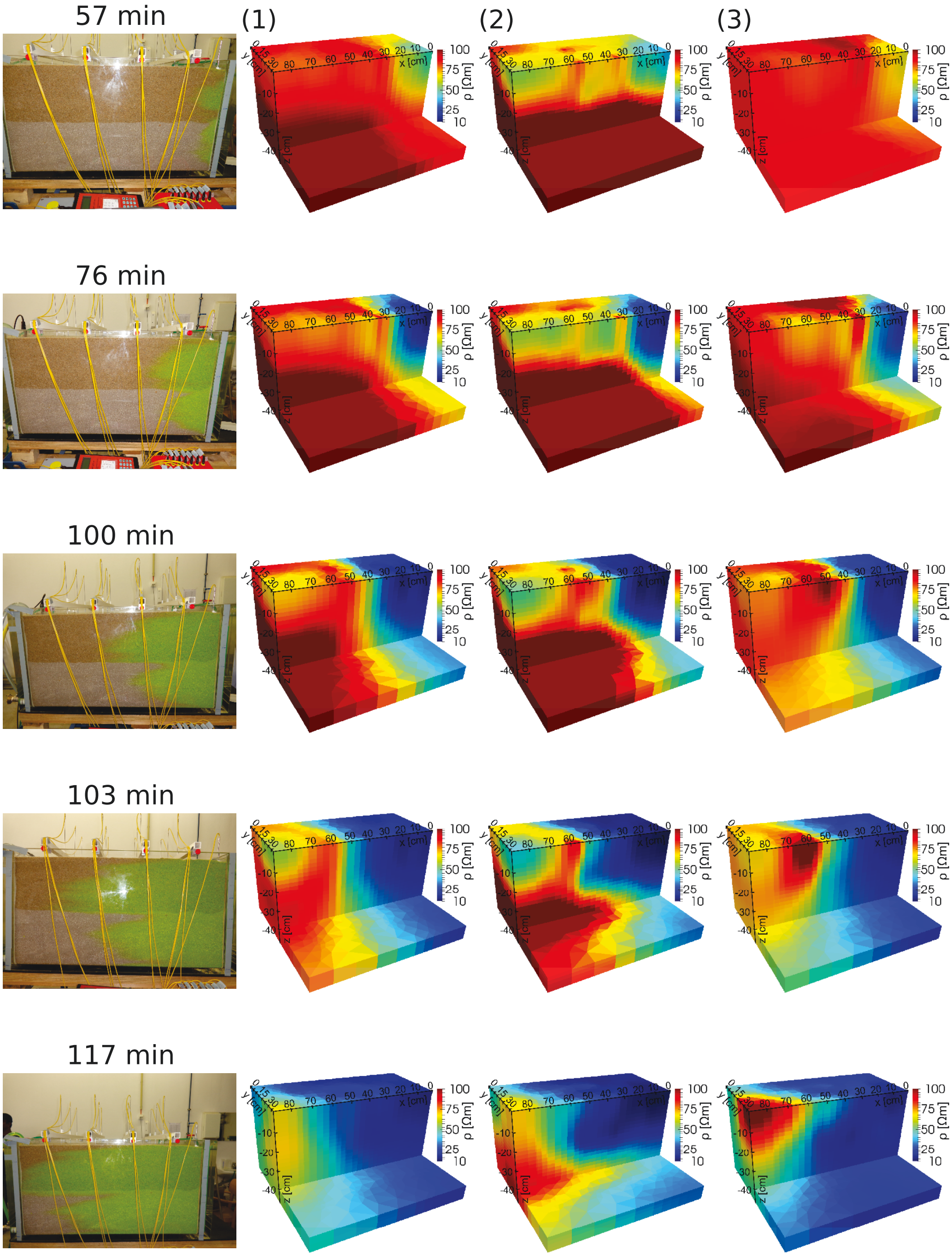

Figure 4.17: Photographs (left) and inversion results for a standard inversion (second column) and a difference inversion with the first time step as base-line (third column) for specific time steps. Results using the time-lapse-step approach and the difference inversion are given in the right column.

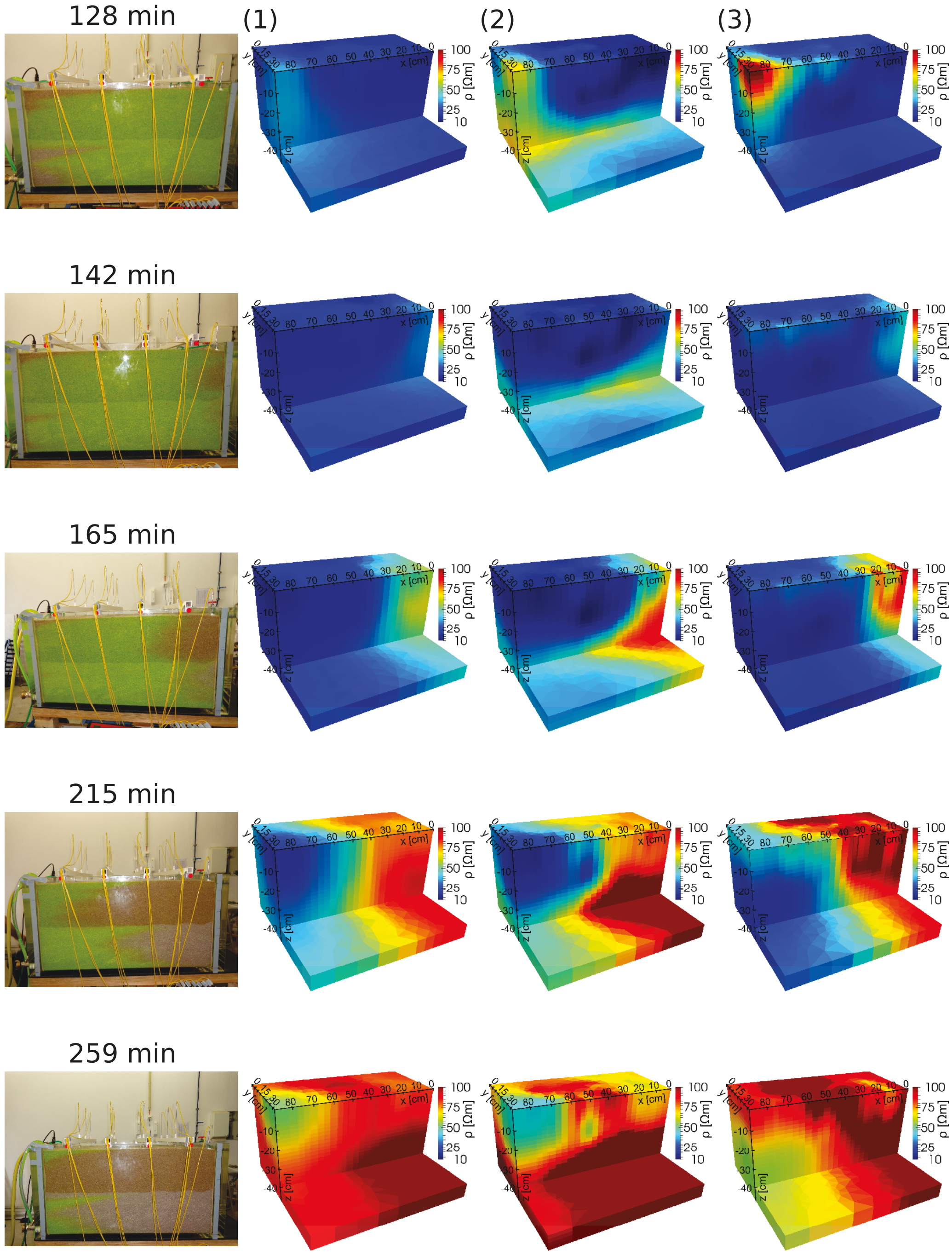

Figure 4.18: Photographs (left) and inversion results for a standard inversion (second column) and a difference inversion with the first time step as base-line (third column) for specific time steps. Results using the time-lapse-step approach and the difference inversion are given in the right column.

Although the misfit distributions give hints to decide the choice of the correct inversion scheme, two additional results are shown in Figure 4.19 and Figure 4.20 with different inversion parameter settings. The inversion result that shows least resistivity artefacts and images the saltwater front best is the third inversion scheme (last column in Figures 4.17 and 4.18) of the former results shown. Thus, it is listed again with the two additional schemes for further comparison. The parameter settings depicted in Figure 4.19 and Figure 4.20 are:

(i)	2nd column:	standard inversion with $\lambda_t = 40$ (fixed) and the first time step as base-line (misfit Figure 4.13a and c)
(ii)	3rd column:	difference inversion with a χ^2-optimised λ_t and the first time step as base-line (Figure 4.15) and
(iii)	4th column:	difference inversion with the misfit of the first time step, a χ^2-optimised λ_t and TLS-approach.

Ten representative time steps are shown with corresponding photographs and their time-stamps. The fitted models in Figure 4.19 and Figure 4.20 agree nicely with the corresponding photographs. The movement of the saltwater-freshwater interface could be imaged. Nevertheless, some weaker pronounced artefacts like slightly decreasing resistivities occur at model parts that are not yet affected by the saltwater. These artefacts appear for example at time steps taken at 76 min and 100 min in front of the saltwater body, between x = 40-80 cm in Figure 4.19.

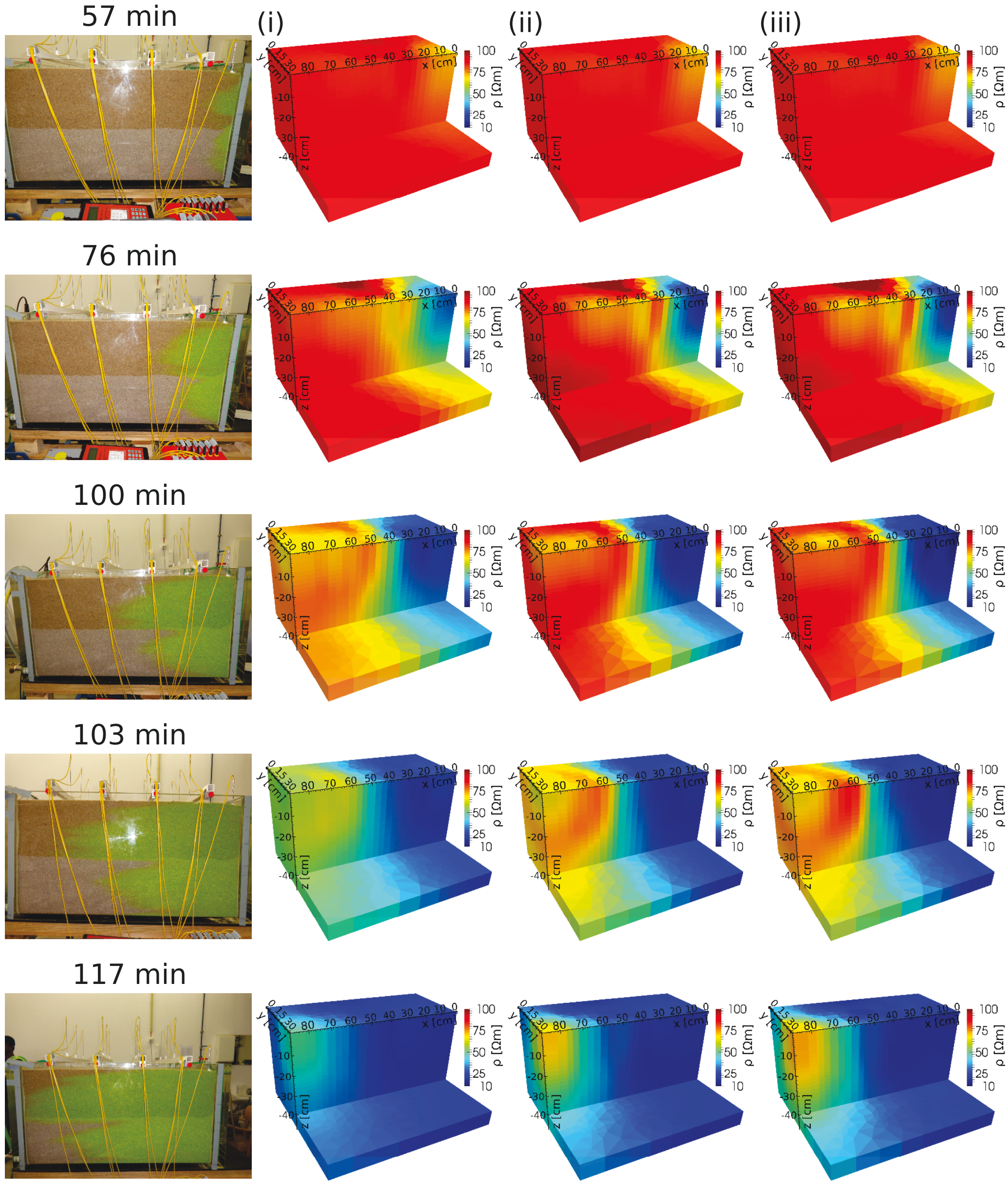

Figure 4.19: Photographs (left) and inversion results for a standard inversion (second column) and a difference inversion with the first time step as base-line (third column) for specific time steps. Results using the time-lapse-step approach and the difference inversion are given in the right column.

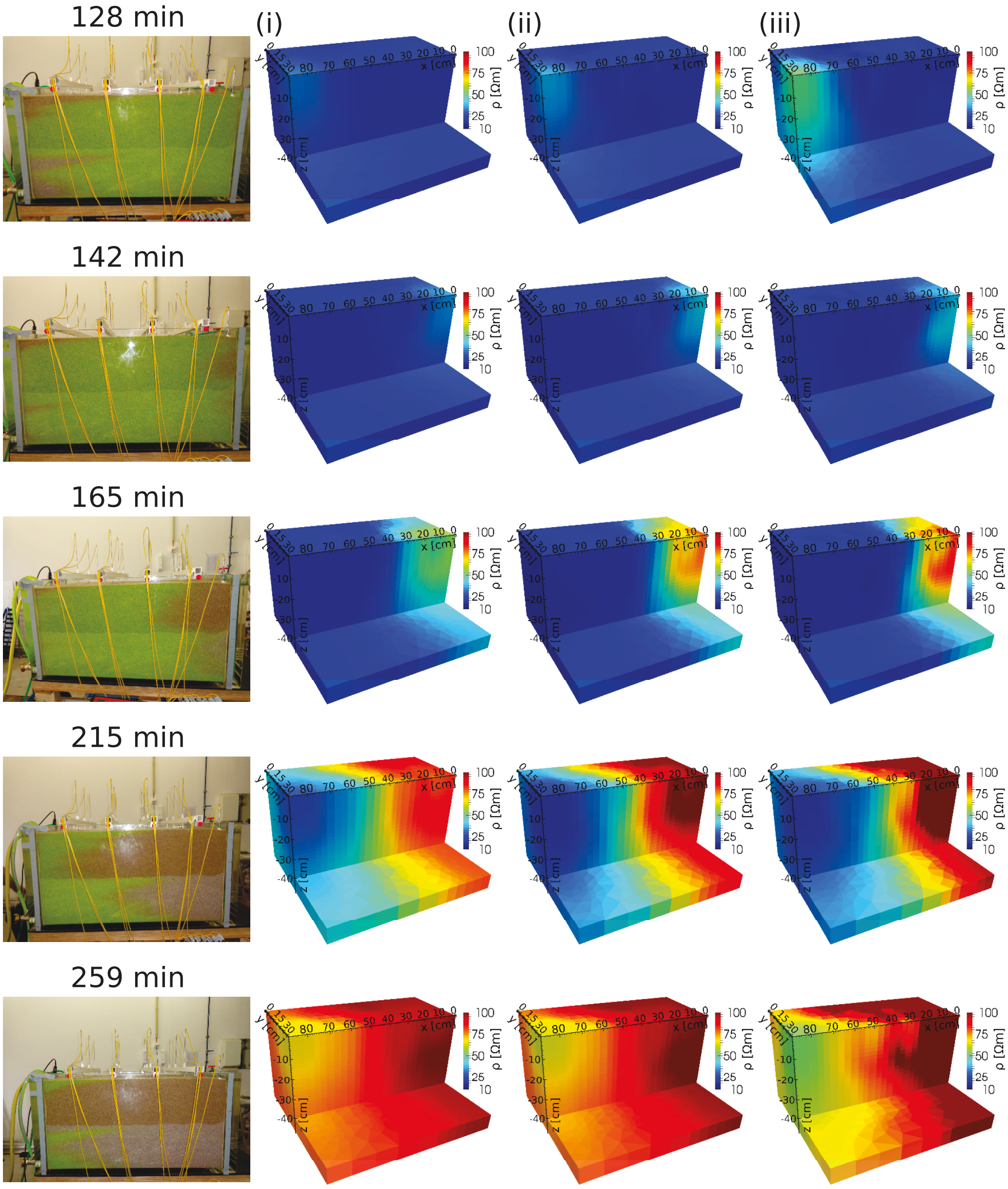

Figure 4.20: Photographs (left) and inversion results for a standard inversion (second column) and a difference inversion with the first time step as base-line (third column) for specific time steps. Results using the time-lapse-step approach and the difference inversion are given in the right column.

In general, all inversion approaches shown in Figure 4.19 and Figure 4.20 show the same behaviour. As the saltwater enters the tank, an interface emerges at the right side of the main chamber and moves to the left.
Early time steps (second to fourth row in Figure 4.19) indicate faster movements of the saltwater front at the upper part of the tank, which can be validated by photographs. The time step after 103 min in Figure 4.19 (fourth row) shows that the saltwater at the back of the tank moves faster than in the middle and reaches at first the left side of the tank. This finding could be validated by the physical experiment, indicating faster fluid transports at the walls in the front and back of the tank.
Between 128 min and 142 min in Figure 4.20 (the first two rows) the model is almost saturated with saltwater. Inversion results show that resistivities decrease down to 15 - 35 Ωm for the saltwater body. It can also be seen that the second stage, i.e. the replacement of the saltwater by freshwater starts after 142 min. This appears again for the replacement of saltwater with freshwater in Figure 4.20. After 259 min are elapsed, the photographs show that almost the whole tank is filled with freshwater again. Small portions of the tracer remain at the left side of the tank. Inversion results of the corresponding time step show lower resistivities for this part, which validates that still a small quantity of saltwater remained. Depending on the inversion scheme, the resistivity distributions are still affected up to x = 50 cm.

If the different inversion results given in the columns (i), (ii) and (iii) are compared, slight but significant differences are noticeable. The inversion results of column (i) for time steps from 100 min to 117 min in Figure 4.19 imaged the freshwater body with a lower resistivity than the inversion schemes (ii) and (iii). This trend for the freshwater body continues in Figure 4.20. For the last time step, after 259 min, inversion (iii) in column four shows a more structured result than inversion (i) and (iii), which image lower resistivities at x = 50 cm and 30 cm.
To summarize, the inversion scheme (ii) in the third column of Figure 4.19 and Figure 4.20 shows the best results. Unexpected resistivity variations are in an acceptable range and the expected resistivities for the freshwater- and saltwater-body are determined.

4.4 Conclusion

The 2D ERT monitoring results showed that the movement of the saltwater-freshwater interface can be imaged well, even if very small. The position of the interface does not correspond exactly to the photographs. Uncertainties in determining the interface occur due to a transition zone between low and high resistivities as a result of the smoothness constrained inversion.
During the formation of the saltwater wedge in the first experiment of the 2D model, the resistivity of the saltwater body (simulated seawater) decreases, which is possibly caused by a low model resolution. This could be avoided by confining the resistivity to a small range. Poor imaging properties also lead to an artificially rising freshwater-saltwater interface on the left side of the tank, which could not be prevented.
Results of the inundation-experiment (2D model) showed that fitted models of early time steps are strongly dominated by resistivity artefacts. The rise of the sea level for simulating the inundation changed the model geometry, which could not be taken into account by the mesh generation. Several solution approaches are possible to counter this problem. The easiest way is to simply discard these time steps for the time-lapse inversion. It is also possible that every time step during the inundation process is inverted with its own finite element mesh that considers the changed model geometry. New inversion approaches are able to include boundary positions in addition to resistivities as model parameters. As interface positions and resistivities are fitted, every time step has its own modified model geometry.
Directly after the inundation the resistivities can be imaged. As Figure 4.5 shows, the percolating saltwater can hardly be observed by the photographs. A reason could be preferential flow paths in the middle of the tank, which are maybe caused by the drippers. Nevertheless, ERT makes it possible to image these saltwater movements. Although the saltwater body is decoupled from the rest, some unreasonable resistivity changes occur in the saltwater region, which could only be avoided by confining the model parameter to a small resistivity range. Generally, all 2D experiments conducted could be imaged well.

Generating optimised data-sets for the 3D ERT monitoring showed that configurations exist with a high information content but low signal under noise-free conditions in a homogeneous half-space. These configurations consist of a voltage-dipole with its axis lying about an equipotential line. Some of these configurations possess high geometric factors, for example if $r_1 \approx r_3$ and $r_2 \approx r_4$ (see Figure 2.2). As suggested by Friedel (2003) those unstable combinations can be down-weighted by using the error-weighted sensitivity matrix as an input for the SVD.

Several inversion schemes were used to fit the time-lapse data. The results showed that a good misfits-distribution does not always image the resistivity distribution well, because resistivity artefacts can appear in model parts with low resolution properties. Although all results imaged the movement of the saltwater-freshwater interface well, some lead to very structured models. Lower resistivities occurring at model parts that were not yet affected by saltwater. They appear in the depth range of the electrodes (from 0 - 20 cm), i.e. in model parts with a low vertical resolution. A possible explanation is that these artefacts are a compensation of an under or overestimated resistivity of the saltwater body. In addition, the high resistivity contrast between saltwater and freshwater in conjunction with the sharp interface lead to these compensation artefacts.

Systematic errors occurring due to uncertainties of electrode positions or discretisation errors can be removed by the difference-inversion scheme suggested by LaBrecque and Yang (2001). If the TLS-approach is used, correcting the inversion input with the misfit of the previous data-set, uncorrelated errors increase from time step to time step, leading to a high error-level. Accordingly, the difference-inversion does not necessarily lead to better inversion results and has to be used carefully. Nevertheless, using the misfit of the first time step for correcting inversion inputs of all following time steps leads to acceptable misfit distributions. To summarise, the difference-inversion using the misfit of the first time step, a χ^2-optimised λ_t and the first time step as base-line gave the best inversion results. The fitted models show the expected resistivities for the freshwater and saltwater bodies. Compared to other inversion results shown, artificial resistivity variations, like decreasing resistivities within the freshwater body, are less pronounced. All time steps show a good compromise between the smoothness needed for homogeneous model-parts and more structured demands for the saltwater-freshwater interface.

5 Field application of LE-ERT on the medium scaled test site Müllrose

Main part of this chapter is published as:

Ronczka, M., T. Voss and T. Günther, 2015b, Cost-efficient imaging and monitoring of saltwater in a shallow aquifer by using long electrode ERT: Journal of Applied Geophysics, 122, 202-209

5.1 Introduction

A crucial advantage of LE-ERT compared to surface ERT is the greater investigation depth, resulting from a sensitivity shift into deeper regions of the subsurface. Synthetic studies of Daily et al. (2004) and Rucker et al. (2011b) showed that the position of resistive or conductive anomalies can be determined laterally, whereas the vertical resolution nearly vanishes if long electrodes of equal length are used. We present an application using pre-existing metal-cased boreholes of different length and additional surface electrodes to overcome the vertical resolution limits.

Different models exist for incorporating long electrodes into Finite-Element meshes. The Complete Electrode Model (CEM), introduced by Cheng et al. (1989), enables the inclusion of arbitrarily shaped electrodes. Details about the theory and the usage of CEM electrodes for LE-ERT measurements are shown in Rücker and Günther (2011). The Shunt Electrode Model (SEM) developed for medical imaging by Wang et al. (1999) simulates electrodes of negligible contact impedance. Although CEM describes the physical reality best, SEM requires less numerical effort as it does not require a fine discretisation at the boreholes (Ronczka et al., 2015a). Since SEM has been successfully used for synthetic studies (Ramirez et al., 2003) and shows discretisation advantages, SEM is used in this study for modelling and inversion.

In the following, a short synthetic study investigates model resolution properties using pre-defined electrode locations of the presented test site. Furthermore, results of a single time step and a time-lapse inversion of LE-ERT data are discussed.
The primary objective is to apply LE-ERT to image and monitor a known saltwater intrusion at a medium-scaled test site under simple geologic conditions and irregularly distributed electrodes. Comparisons with water samples at different time steps are made to verify its repeatability and derive fluid conductivities. Additionally, synthetic models are used to test the performance of the method under controlled conditions and to determine model resolution properties of a reduced data set compared to a comprehensive one.

5.2 Test site description

The test site is located near the town Müllrose in the eastern part of Brandenburg, close to Frankfurt/Oder (Figure 5.1). The test site was chosen for two reasons, i.e. the presence of a saltwater intrusion and a sufficient amount of metal-cased boreholes. Within a hydrogeological campaign 18 boreholes had been drilled between 1986 and 1988, providing detailed geological information. The site is situated within the lowlands of the Berlin-Warsaw glacial valley. The uppermost layer consists of mostly homogeneous quaternary fluvial sands with a thickness of 35-40 m. The unconfined water table in the first aquifer lies about 1.5-2 m below the surface. The quaternary sands are underlain by an uninterrupted 60 m thick Miocene silt and coal inter-bedded with thin layers of silty fine sands. A regionally important Miocene-Oligocene sandy aquifer with an average thickness of 60 m follows below ≈100 m depth (see Figure 5.1 for simplified lithology). In basins this aquifer show almost artesian behaviour with a pressure head at the surface. A more detailed geological and hydrogeological description can be found in Hotzan and Voss (2013).
In this work, we focus on a 500 × 300 m area that is bordered to the north by the Oder-Spree canal and to the south by a road. Twelve metal-cased boreholes with an average length of 35 m are distributed in the area. The boreholes BH1 and BH6 with 4 m and 4.50 m length differ from the rest, whereas BH8 with 106 m is exceptionally long, providing information about the second aquifer. Contact resistances of the first survey indicated that the metal casing of BH12 is broken and thus was replaced with a surface electrode. The given borehole distribution shows larger gaps, which were filled with surface electrodes (Figure 5.1).

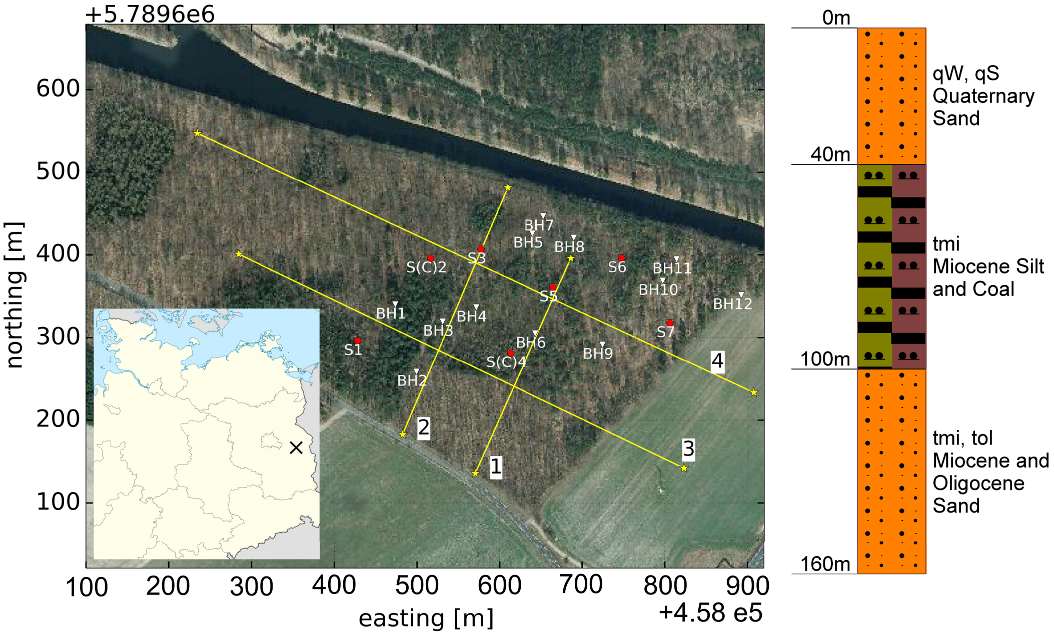

Figure 5.1: Set-up and location of test site Müllrose (left) and a simplified lithology from borehole information (right). Borehole positions are denoted by BH, surface electrodes by S or SC if they are equipped for current transmission with SC. Yellow lines mark the conducted ERT profiles. Coordinates are given in UTM zone 33N using the WGS84 ellipsoid.

Some of the wells at the test site are screened at multiple depths thus enabling depth-sensitive fluid sampling. Water sample conductivities with values up to 0.18 S/m reveal highly mineralized water at the base of the quaternary aquifer between 30-40 m, whereas the Miocene aquifer exhibits a lower mineralization. Two possible theories exist to explain the increased salinisation in the quaternary aquifer. One possible origin is solution processes of a salt dome about 10 km north-west, which is already risen to a depth of about 150 m below surface. The second theory involves mainly vertical flow patterns. It states that deep saline aquifers are connected with near-surface freshwater aquifers by the Fürstenwalde-Guben fault zone, striking about 5 km west of the test site. Upward pointing hydraulic gradients and weakness zones at impervious layers are necessary for the migration of high-density saltwater into near surface freshwater bearing aquifers. Different groundwater flow directions in the aquifers might lead to the observed salinity variations between the quaternary and Miocene aquifer at the test site.

Four 2D-ERT profiles (location see Figure 3.4) were conducted for comparison purposes. A Wenner-α configuration with an electrode spacing of 5 m was measured using the standard ERT instrument *4point light 10W* with an active

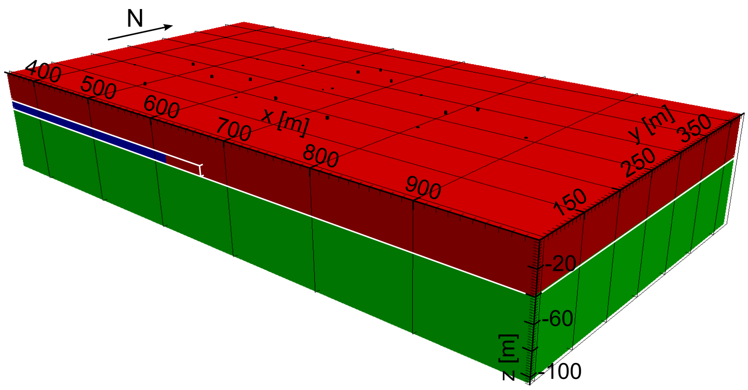

Figure 5.2: Underlying 3D model for generating synthetic data. The blue body marks the saltwater intrusion for the first model (M_1) and white contour lines for the second (M_2).

electrode chain (*ActEle*) by LGM electronics. Profile lengths of 500 to 800 m were measured in a roll-along mode.

5.3 Synthetic modelling and inversion

Synthetic models were generated using the borehole setting and a simplified geology of the test site Müllrose. The aim of the part of the study is to investigate model resolution properties and performance of a reduced data-set for efficient monitoring purposes.

5.3.1 Model description

A simple two-layer case was constructed with a 40 m thick top layer followed by a second layer of infinite depth. The first layer was assigned with a resistivity of ρ=100 Ωm representing a sandy aquifer, whereas the resistivity of the second layer was set to ρ=25 Ωm representing silt, respectively. A possible saltwater intrusion was placed at the bottom of the first layer with a thickness of 10 m and a resistivity of ρ=5 Ωm.
Two models were taken into account with different lateral extensions of the saltwater intrusion. In the first model (M_1), the right boundary of the intrusion was set to x_{max}=614 m and subsequently moved to x_{max}=664 m for the second model (M_2). A schematic sketch is shown in Figure 5.2.
The mesh for generating synthetic data has an extension of $3.7 \times 2.6 \times 2.8$ km to avoid influences of the boundaries on the calculated potential field. The parameter domain of the inversion mesh is extended to $927 \times 652 \times 106$ m, leading to a mesh with about 20,000 cells for the parameter domain. Long

electrodes are approximated using the shunt electrode model (SEM) as described in chapter 3.

5.3.2 Inversion of synthetic data

To obtain a maximum information content, a full data set with 11,626 possible four-point combinations out of 19 electrodes was calculated. Data were contaminated with Gaussian noise using a standard deviation consisting of 2% relative error and a voltage error of 100 μV. Synthetic data were filtered, discarding those with geometric factors exceeding ± 30 km and errors above 10%, resulting in about 10,900 data points as inversion input. In the parameter domain, the resistivities were confined to $3 \leq \rho \leq 200\,\Omega$m. A smoothness constrained inversion was done as described in section 2.4.
The inversion result of M_1 in Figure 5.3a shows that the resistivities of the upper and lower layers are well determined with ranges of 80-120 Ωm and 15-30 Ωm, respectively. The interface at 40 m depth is generally resolvable, but appears as a smooth transition zone with $\approx$ 10-15 m thickness. The conductive anomaly is indicated by a sharper transition zone, but its shape and resistivity is poorly resolved. The mapped anomaly penetrates the lower layer, which might lead to misinterpretations when locating saltwater intrusions.
To image sharper resistivity contrasts, structural prior informations can be incorporated in the mesh by setting the weight of the known boundaries to zero (Doetsch et al., 2012). The cost function 2.23 that has to be minimised is given in section 2.4. After Günther and Rücker (2006), the model roughness Φ_m that controls the variability of the model parameter $\mathbf{m}$ can be extended to

$$\Phi_m = \lambda \parallel \mathbf{W}^c \mathbf{C} \mathbf{W}^m (\mathbf{m} - \mathbf{m^0}) \parallel_2^2 \, . \tag{5.1}$$

Here, the boundary control $\mathbf{W}^c = diag(w_i^c)$ is a diagonal matrix with weighting factors for the different cell boundaries. It can be used to include anisotropic constrains or even sharp boundaries like geologic interfaces by setting $w_i^c = 0$ for affected boundaries. Individual regularisations for different model parts, or fixed model parameters can be realised by the model control $\mathbf{W}^m = diag(w_i^m)$. The interface at 40 m depth was included into the mesh, thus separating two regions. A significant improvement is achieved, resulting in a sharpened mapping of the conductive anomaly on top of the layer interface (see Figure 3.6b). The resistivity of the anomaly is well resolved, but artefacts appear at the surface, although the resolution radii distribution (Figure 3.6c) shows good imaging properties. In general, well-resolved parts reach almost down to 40 m depth.

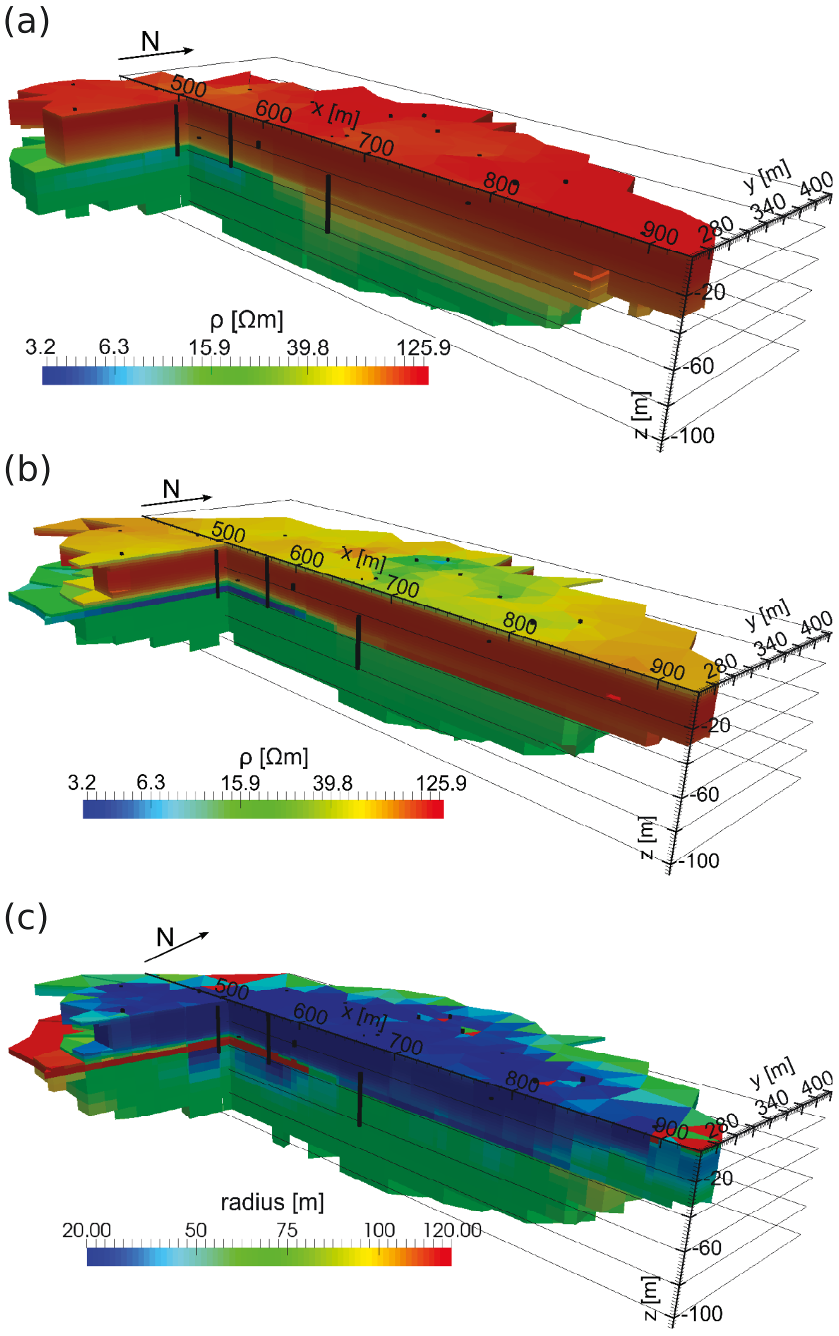

Figure 5.3: Inversion results of the first model without and with a-priori information are given in (a) and (b). The corresponding resolution radii are shown in (c).

Note the large radii, i.e. a poor resolution for the anomaly resulting from the low resistivity. Due to a decreasing coverage, the resolution deceases towards the boundaries.
The main task of LE-ERT monitoring is to resolve resistivity changes in the subsurface. Therefore, the ratio between the two models M_1 and M_2, representing different time steps, is presented in Figure 5.4.

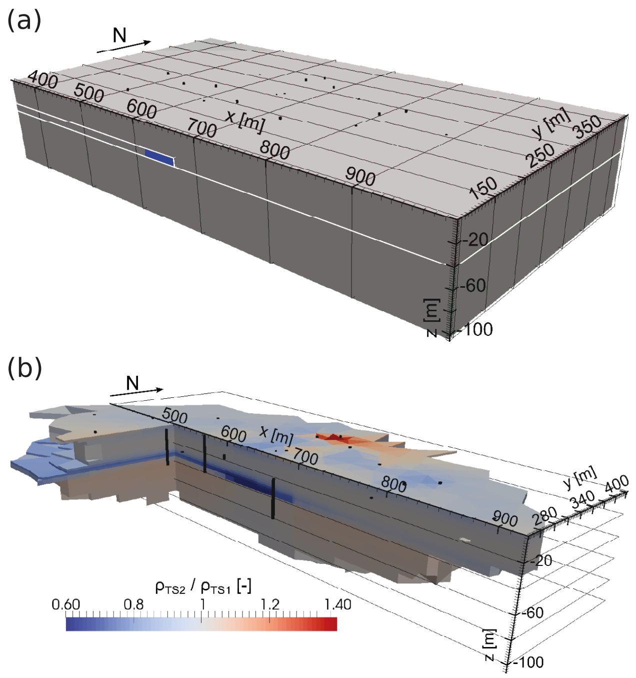

Figure 5.4: Resistivity ratio between the two synthetic models M_2 and M_1 (a). White outlines denote boundaries between synthetic model units. The blue body marks the difference between M_1 and M_2. The resistivity ratio of the corresponding inversion result are shown in (b).

The anomaly movement is well resolved, occurring as a large resistivity decrease of the 50 m wide zone. Artificial resistivity changes occur at the surface, similar to the inversion result shown in Figure5.3b.

5.4 Reduced field set-up

A main task, regardless of the given test site, is to develop a scale-independent LE-ERT methodology that can also be applied to larger areas. Logistic, cost and time aspects does not allow LE-ERT surveys with several thousand dipole combinations. Thus, a reduced field set-up was applied on the test site. For field measurements a decentralised approach is needed, in which 3-channel data logger are distributed over the test site and connected to electrodes for recording voltages as time series. Possible positions for the data logger for potential measurements were defined, marked as coloured rectangles in Figure 5.5a. By connecting these to three adjacent electrodes, a net of potential dipoles is built, which is fixed for the whole LE-ERT monitoring. Next, current dipoles are generated under different aspects as logistic questions or maximum information content with minimum effort. For this test site, the transmission dipoles were chosen after logistic aspects like accessibility and minimum number of stations for the current source. The dipole set for current transmission used in this study is shown in Figure 5.5b. The reduced data set was tested on the synthetic case M_1 (Figure 5.2). The same filter routine used for the complete data set was applied, leading to 322 remaining data points for inversion. Note that only 152 independent data exist for 19 electrodes (Xu and Noel, 1993). However, a slight redundancy is considered a robust choice in case of realistic noise.

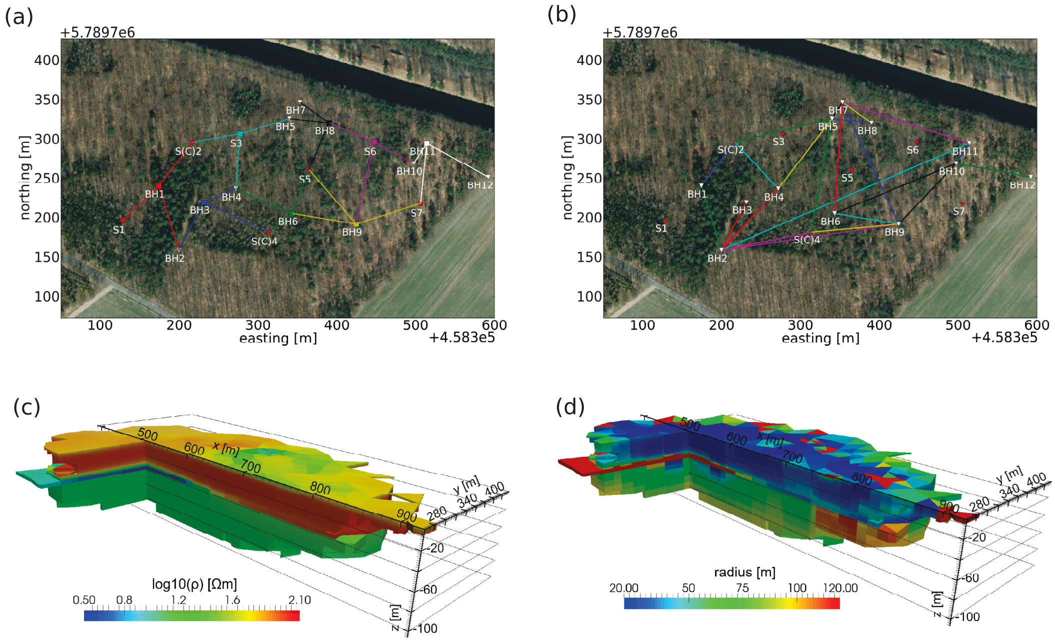

Figure 5.5: The distribution of potential dipoles is given in (a) with the corresponding current dipoles in (b) for the reduced data-set. The inversion result using the synthetic case M_1 is given in (c). The distribution of resolution radii is shown in (d). See Figure 3.4 for description.

The inversion result of the reduced data set and its resolution radii distribution is given in Figure 5.5c-d. Shape and resistivity of the anomaly and the resistivities of the upper and lower layer are resolved as good as the inversion result of the complete data-set in Figure 5.3b does. The resolution radii distribution in Figure 5.5c shows medium radii lower than 40 m down to 80-100 m depth, excluding the anomaly, which is only a slight decrease for the first 40 m compared to Figure 5.3d. Larger radii appear for deeper regions and at the boundaries, indicating worse resolution compared to the complete data-set. In general, the minimum resolution radius is given by the electrode distances of the pre-defined electrode distribution.

5.5 Field measurements

5.5.1 3D Long Electrode ERT

Experiments at the test site started in November 2012 and ended in December 2014. After installation of a centralized cabling the measurement of one time step lasted only 30 minutes. All LE-ERT measurements were conducted with the dipole setting depicted in Figure 5.5a and Figure 5.5b. A total amount of 446 data points was gathered for each survey. An error model consisting of 4% and a voltage error of 10 μV was assumed. Geometric factors were calculated numerically on a fine tetrahedral mesh. Prior to inversion, data exhibiting errors of more than 10% or geometric factors of $\mid K \mid > 30$ km were discarded. Inversion was done on a triangular prism mesh with 20,000 cells. The interface between the quaternary and Miocene layer was included as a-priori information. Borehole informations indicate a small rise from 40 m at the western part up to 37 m depth (eastern part), which was considered in the model by a linear trend between the easting coordinates 458600 and 458770 m (utm). Subsurface resistivity was confined to $5 \leq \rho \leq 200$ for the quaternary and to $15 \leq \rho \leq 200$ for the Miocene layer using logarithmic transformations (Kim et al., 1999).
The determined apparent resistivities (ρ_a), geometric factors and the misfit of the LE-ERT measurement, conducted in December 2014, are shown in Figure 5.6. Since the current and voltage dipoles are irregularly arranged, a matrix plot for the raw data was used with electrode numbers indicating current and voltage dipoles on both axes.
Figure 5.6a shows a narrow ρ_a-distribution around 20-50 Ωm with just a few outliers, as a result of the poor resolution at the surface and the bypass of near-surface high resistive zones due to the current transmission into the aquifer by metal casings. The error-weighted misfit follows a Gaussian normal distribution (Figure 5.6d), i.e. data are fitted statistically within the error model. According to Figure 5.6c, large misfits can not be assigned to a specific dipole or electrode, indicating that all connections at the metal casings and wires are intact. A comparison with Figure 5.6b shows that large misfits do also not correspond to high geometric factors, i.e. unstable potential readings. The corresponding

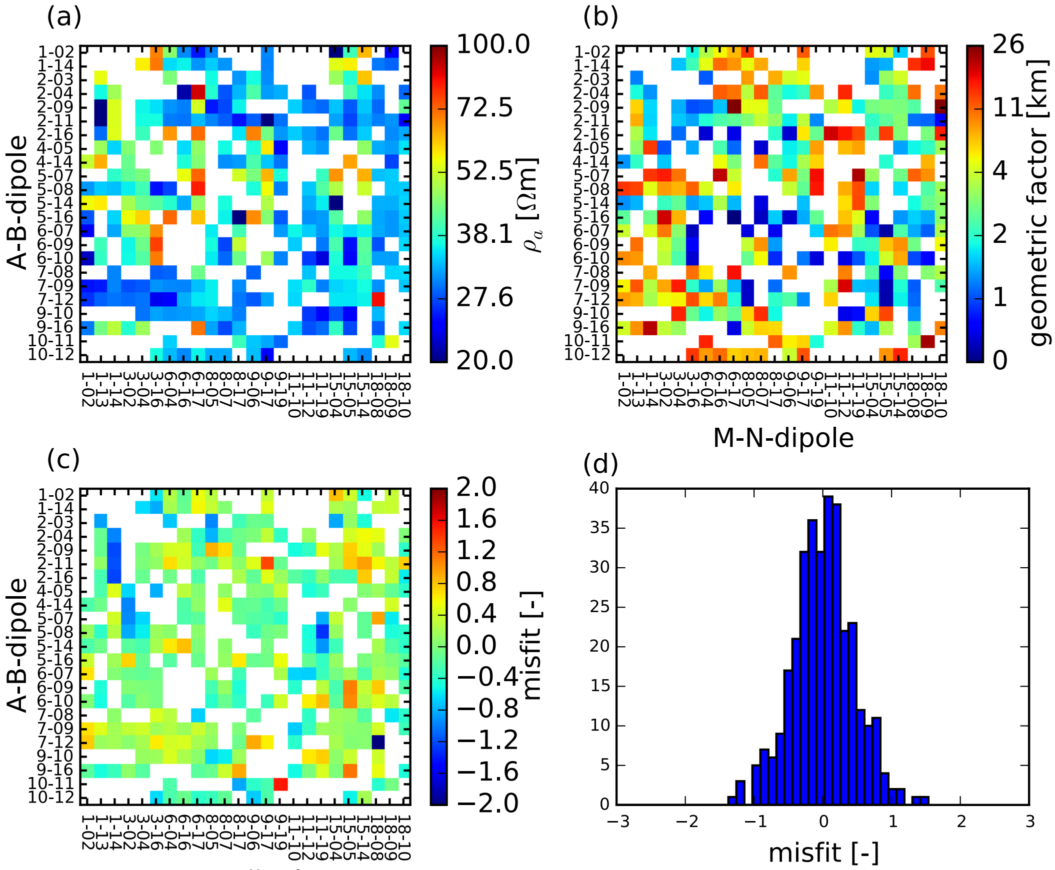

Figure 5.6: Raw data (a) and geometric factors (b) of the LE-ERT measurement in December 2014. Distribution (c) and histogram (d) between data and forward response. In (a)-(c), current and potential electrode numbers are given as axes labels.

inversion results of the LE-ERT survey conducted in 12/2014 and the 2D-ERT profile 4 (Figure 5.1) are displayed in Figure 5.7.

In general, the 2D slice of the LE-ERT result (Figure 5.7b) is in good agreement with the 2D-ERT result (Figure 5.7a). According to the a-priori information used, a two layer case appears with resistivities of about 100 Ωm for the upper and about 30 Ωm for the lower layer. The result of the 2D-ERT profile (Figure 5.7a) shows decreasing resistivities within the upper layer from west to east. The slice of the LE-ERT result in Figure 5.7b shows the same behaviour, but less pronounced. Contrary to Figure 5.7a, the LE-ERT slice show smaller resistivities about 50 Ωm near the surface, which decrease to 15 Ωm in some parts (Figure 5.7c). All results in Figure 5.7 show a conductive anomaly at the eastern part of the test site at the bottom of the upper layer.

Since borehole information indicate constant geologic conditions for the upper layer, higher mineralised ground water is a probable explanation. The three-

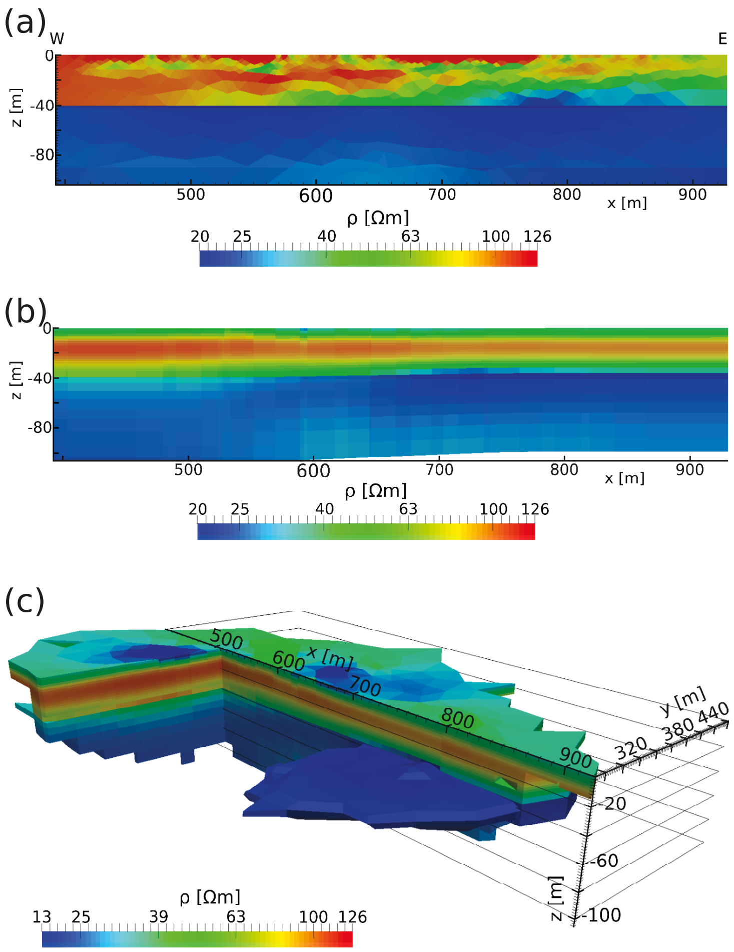

Figure 5.7: (a) Inversion result of the ERT profile 4 (location see Figure 5.1). (b) the corresponding 2D slice of the LE-ERT result. (c) Inversion result with added a-priori information showing the spreading of the low resistive anomaly. The ρ-iso-surface body describes resistivities lower than 20 Ωm. The LE-ERT survey was conducted in 12/2014.

dimensional resistivity distribution of the LE-ERT result is given in Figure 5.7c. The body with resistivities lower than 20 Ωm shows the spatial extent of the low resistive anomaly, mainly in the eastern part.

For verification of the inverted resistivity distribution, fluid samples were taken from all available filter screens. To relate bulk resistivities and fluid conductivities, a modified Archie equation after Waxman and Smits (1986) was used:

$$\sigma_{\text{bulk}} = \frac{1}{F}\sigma_{\text{f}} + \sigma_{\text{s}} \tag{5.2}$$

In-situ fluid conductivities taken from all available filter screens and their corresponding σ_{bulk} from the inversion result were used to estimate the formation factor F and the surface conductivity σ_s. As F is constant for a homogeneous material only σ_f from the quaternary layer were used. A formation factor of $F = 4.5$ was estimated, which lies within the acceptable range for unconsolidated medium sand given in Schön (2004). The determined surface conductivity of $\sigma_s = 4.77\,\mathrm{mS/m}$ has, as expected, a negligible influence on the bulk conductivity. As F and σ_s are material-dependent, only bulk conductivities of the quaternary layer can be converted into fluid conductivities. In Figure 5.8 measured (red) and calculated σ_f are plotted for the boreholes BH2, BH3, BH7 and BH9 (see location in Figure 5.1).

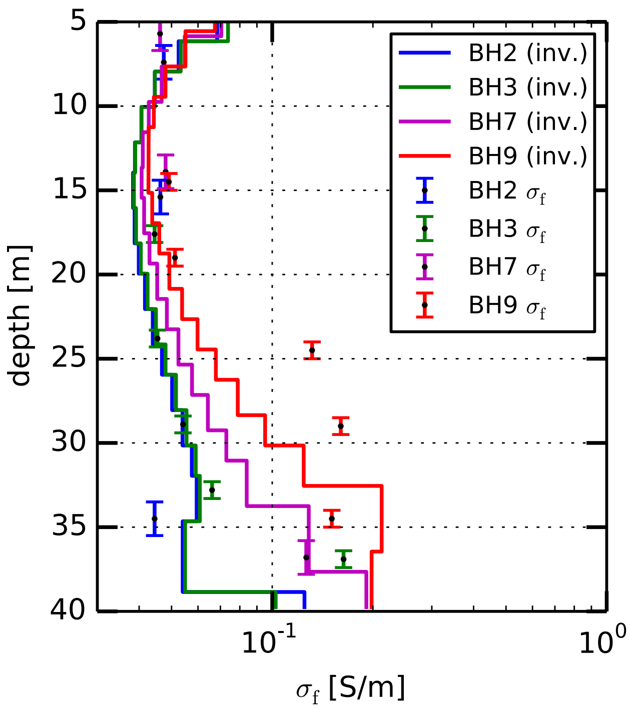

Figure 5.8: Measured (vertical bars marking the filter screens) and calculated fluid conductivities at four different borehole locations.

The curves in Figure 5.8 match quite well with measured fluid conductivities supporting the quality of the LE-ERT inversion result. The increased fluid conductivities of about 0.1-0.15 S/m in the depth range of 25-40 m at BH7 and BH9 validates the assumption of higher mineralised ground water at the bottom of the quaternary layer, predominantly in the eastern part. The fluid conductivities from BH2 and BH3 show no significant increase down to 35 m depth, indicating that the saltwater intrusion disappears gradually towards west. The sharp increase of σ_f between the second and third filter screen of BH9 (20-25 m depth) is not resolved in detail. The leap towards the last filter screen (37 m depth) at BH3 is shifted about 2 m downwards but still visible in the inversion result. Both reflect the limitations of resolution properties of an ERT measurement conducted with only 19 electrodes.

5.5.2 Time lapse LE-ERT

For observing resistivity changes due to possible saltwater movements at the test site, LE-ERT measurements were repeated every three months between November 2012 and December 2014. Fluid conductivities at borehole BH3 were measured to validate the temporal trend given by ERT. Constant two-point resistances between the long electrodes indicated that the influence of varying contact impedances on this LE-ERT survey is negligible.
Data were filtered using the same parameter settings and with the same error model as for the static inversion above. The mesh and a-priori constrains remained the same. A time-lapse inversion was done as described by equation (2.25) with a constant temporal regularisation of $\lambda_t = 100$. Inversion results and the monitored fluid conductivities indicates only slight changes in the observed period. For visualizing resistivity changes, five time steps were used to generate four ratios shown in Figure 5.9. As the base line, the measurement conducted in December 2014 was chosen as this is the only time step with fluid conductivities measured in all boreholes. The largest possible data set of σ_f is needed to predict the formation factor F with greater confidence, in order to convert σ_bulk of the LE-ERT result into σ_f. Therefore, the order of the time steps was reversed for the time-lapse inversion. However, the shown ratios, i.e. the later resistivity by the former, are calculated in the correct temporal order, starting with the ratio 11/2012 - 09/2013 in Figure 5.9a to ratio 06/2014 - 12/2014 in Figure 5.9d.
With just a few per cent, the overall changes are rather small, which is validated by measured fluid conductivities of BH3 shown in Figure 5.10. Most of the images indicate changes at the surface, which probably results from a changing water content due to seasonal variations or near-surface artefacts in the individual time steps.
Almost no resistivity changes appear, as expected, for the Miocene layer except the first and last resistivity ratio. Mostly, the ratios indicate a slightly decreasing resistivity in the upper parts of the quaternary layer. In the lower part, at the saline zone, positive ratios indicate a slightly increasing resistivity in all time steps, which can be caused by a successive reduction of mineralized ground water due to freshwater inflow. Fluid conductivities from the filter screen at 32-33 m depth validate this observation. Shallow parts, which are not affected by saltwater show a constant behaviour. A strongly increased

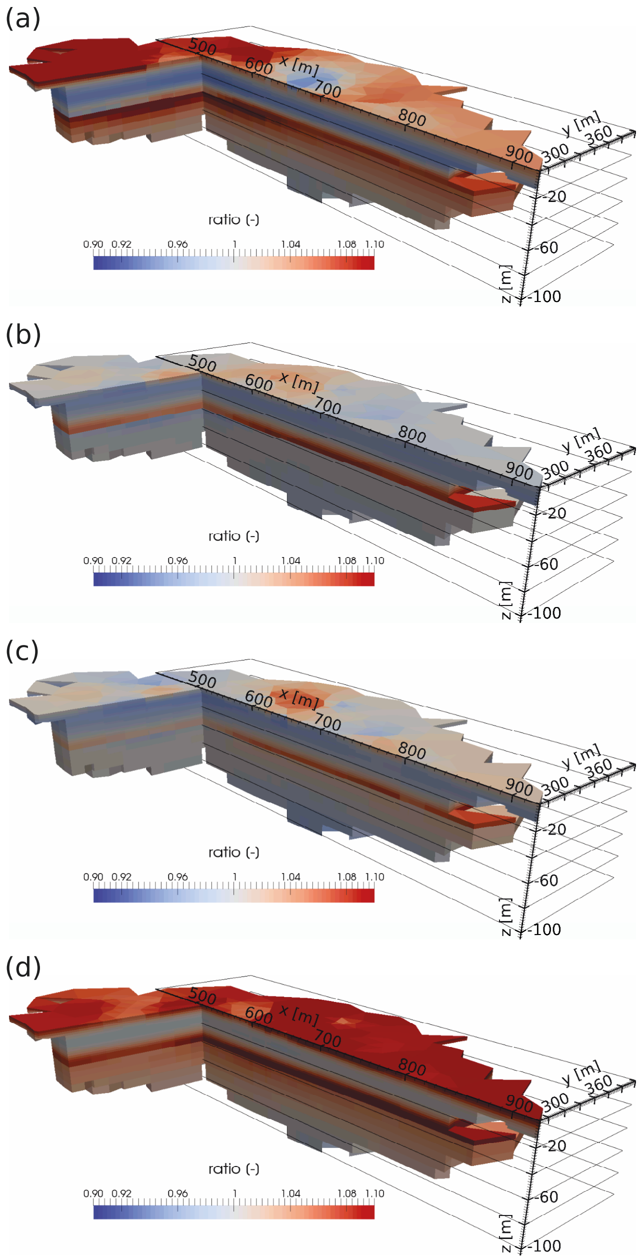

Figure 5.9: Resistivity ratios of inversion result for subsequent datasets from (a) 11/2012 to 09/2013, (b) 09/2013 to 12/2013, (c) 12/2013 to 06/2014 and (d) 06/2014 to 12/2014

resistivity appears at the last ratio shown in Figure 5.9c. Nevertheless, the general trend shown by σ_f measurements and the LE-ERT monitoring indicates that the saltwater contamination seems to disappear. Figure 5.10 shows the measured fluid conductivities at BH3 in comparison with values calculated from time-lapse inversion results.

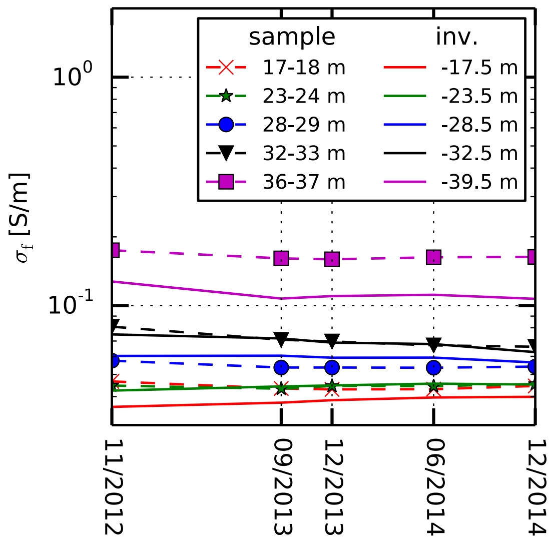

Figure 5.10: Temporal change of measured fluid conductivities for samples from filter screens (symbols, dashed line) in BH3 along with estimated fluid conductivities from the time-lapse inversion (solid lines).

The general trend, although showing only small σ_f-changes, can be reproduced by the LE-ERT time-lapse inversion results. The absolute σ_f value of the filter screen at about 37 m depth does not match well at BH3 as already seen in Figure 5.9. This results from a low model resolution, which is obviously not sufficient for imaging the exact depth of the conductivity contrast. Nevertheless, despite artificial near-surface conductivity changes, Figure 5.10 shows that the fluid conductivity samples validate the ERT results. But it has to be taken into account that electrical fluid conductivities of all filter screens were used to calculate fluid conductivities from the inverted resistivity distribution, which is kind of circular.

5.6 Conclusions

Long Electrode ERT (LE-ERT) measurements with steel-cased boreholes are able to reconstruct 3D resistivity distributions. Inversion of synthetic data showed that the lateral extension of a thin conductive anomaly can be determined correctly, while its thickness is not well resolvable. By adding structural a-priori information to the static inversion, thickness and depth of the simulated anomaly are well determined. The LE-ERT monitoring of a lateral saltwater intrusion was simulated. Inversion results show that the given electrode layout provides a sufficient model resolution for the corresponding resistivity changes. Simulations with a reduced number of data, i.e. dipole combinations based on the distribution of three-channel data loggers, show comparable resolution compared to a comprehensive data set. This approach can be applied to larger test sites.

The inversion result of a single LE-ERT time step agrees with resistivity distributions based on 2D-ERT profiles. However, small-scaled near-surface variations cannot be mapped as good as with 2D-ERT due to the reduced vertical resolution of LE-ERT. Results for both data sets show mainly a two-layer case and indicate a conductive anomaly in the eastern part of the test site. In-situ fluid conductivities taken along with the LE-ERT survey validate the occurrence of saltwater and thus the mapped anomaly at the bottom of the quaternary aquifer.

A Waxman-Smits type equation (see section 2.1) was used to convert the LE-ERT resistivity distribution into fluid conductivities. The comparison between inverted and measured fluid conductivities shows good agreement, proving that LE-ERT maps the hydrogeological conditions at the test site correctly. The location of the conductive body supports the theory of regional authorities presuming that saltwater is intruding from North.

A permanent wiring was installed, allowing fast and cost-efficient long-term monitoring. Observed resistivity changes over the monitoring period of two years were small, but resolvable. Resistivity variations at the surface are most likely explainable with seasonal effects. The slightly increasing resistivities at the bottom of the quaternary layer indicate a decreasing mineralisation of the ground water. A comparison of measured fluid conductivities with the time-lapse inversion results showed that both data sets yield to the same temporal conductivity changes. Monitoring over a longer periods is needed to predict whether a saltwater intrusion or dilution is currently occurring at the site.

6 Field application of LE-ERT on the large-scaled test site Briesen

The feasibility of the LE-ERT method for a large-scaled application was tested on the second test site next to the village Briesen, which is also located in south-east Brandenburg (see Figure 1.1). A large number of about 80 boreholes, a known saltwater intrusion and the presence of a water works facility that could possibly provide further information about the test site made it well suited for LE-ERT surveys. Besides extrapolating the punctual information given by groundwater wells to a greater scale, another main task was to appraise human, material and the temporal effort needed for a LE-ERT survey that covers several square kilometres. Two surveys were conducted that cover the whole area. Due to the limited time of the project, no time-lapse measurements could be designed and conducted.
After a short test-site description, the design of optimised dipole combinations to maximise the information content is explained. Following this, recently developed data logger used for the surveys is presented followed by the description of the Lock-In approach for estimating amplitudes of noise-corrupted time series. Finally, inversion results of the two conducted field surveys and their combination is shown with concluding comments.

6.1 Test site description

Regional geological conditions as described in chapter 1 lead to a comparatively shallow groundwater level in the whole region. The loosely packed sands of the upper unprotected aquifer lead to a high groundwater recharge rate. The area represents an important groundwater resource that has been used since the 1960s as a drinking water supply for Frankfurt/Oder and nearby villages.
Currently, some wells of the water works at test-site Briesen show higher NaCl-concentrations. The first possible explanation is provided by a local Zechstein salt diapir in the western part of the test-site. Borehole logs indicate its cap at about 150 m depth. The quartz- and mica-sand aquifer, which is

already penetrated by the salt diapir, can dissolve NaCl that leads to a higher mineralisation of the groundwater. Nevertheless, a freshwater bearing zone was found in 70-120 m depth. It lies directly on top of the quartz- and mica-sand aquifer and below the known saltwater intrusion. Hence, its presence indicates no vertical fluid movements within the test-site.
A second possible source for saltwater intrusions are the earlier mentioned gaps in the Rupelian clay somewhere outside of the test site, in conjunction with lateral inflow of saltwater in the test site. Investigations of Kempka et al. (2015) and Hotzan and Voss (2013) support this theory. Their assumption is that the source of the saltwater intrusion appears south-east of the test site, directly above the FGFZ (see Figure 1.1). Three main factors support this assumption:

1. gaps in the Rupelian clay caused by the FGFZ,
2. Pleistocene erosion channels which eroded the Rupelian clay and
3. the morphological low position of this area, which acts as a pump due to a lower hydraulic pressure.

Water samples taken at several positions between 20–30 m depth show a salt content that equals an equivalent concentration of $\sim$2-5 g/l NaCl, which is by far larger then the threshold for drinking water in Germany (0.25 g/l). Higher mineralised groundwater was coarsely located at the southern and western part of the test site. LE-ERT surveys were planed to verify the punctual information of the water samples and to image the three dimensional resistivity distribution in order to estimate the shape of the possible saltwater intrusion.

6.2 Optimizing dipole combinations

An enormous effort in time and material to install a complete cabling for a LE-ERT survey can be assumed, due to the large scale of the test-site (about 7×7 km). Field surveys on this scale were conducted using a decentralised approach, in which 3 channel data logger for recording voltages are equally distributed at the test site. Each data logger connects a central electrode with three electrodes in the vicinity. In that manner, a net of potential dipoles is defined for measuring voltages simultaneously at all positions for a current transmission. The first objective is to find a suitable set of current dipoles in order to minimise the effort for conducting the field survey and keep the information content high. This can be described simply by "information content versus effort" task. The algorithm described in section 4.3.2 using the data

resolution matrix ($\mathbf{R}^D$) was modified according to the test site conditions and chosen approach. The singular value decomposition (SVD) described in section 2.5 was used to calculate $\mathbf{R}^D$.
For covering large areas, a decentralised set-up has to be used, i.e. data logger are uniformly distributed over the test-site that define positions of the voltage dipoles, recording the time-series. The algorithm was modified to find the optimal set of current dipoles for the pre-defined potential dipoles, rather than using a comprehensive data set. The 'quasi-'comprehensive data-set consists of all possible current dipoles for the given set of potential dipoles, which lead to a maximum number of about 7400 dipole combinations. As before, the data resolution matrix is calculated on the basis of an SVD using the sensitivity matrix $\mathbf{J}$ (see section 2.4) as input. As suggested by Friedel (2000) the sensitivities were weighted with an error in order to down weight dipole combinations with a low signal to noise ratio. Due to the simultaneous measurement at all potential dipoles for one current transmission, the cumulative importances of all potential dipoles with one current dipole were taken into account, rather than importances for every dipole combination. The median of the information contents of all dipole combinations was determined and used as a threshold for discarding combinations with a low information content. Discarding 50% by the median has proven to be useful in the laboratory experiments shown in section 4.3. The updated data set and sensitivity matrix is then used as a new input for calculating the resolution matrix in the next run. Thus the data-set will be successively reduced until a manageable amount of current transmissions are left with an acceptable loss of information content.
For both surveys the pre-defined distribution of potential dipoles and corresponding calculated current transmissions is shown in Figures 6.1 and 6.2. The optimisation process led to about 680 dipole combinations for both surveys using 31 current transmissions each. Two surface electrodes were added to the surveys to close gaps within the given electrode distribution, which are marked with S in Figures 6.1 and 6.2. The electrodes 5 and 19 are PVC cased wells and cannot be used as long electrodes. Cable with lead weights were lowered down to the filter screen of the wells to use the ground water for the electrical coupling towards the subsurface.

(a)

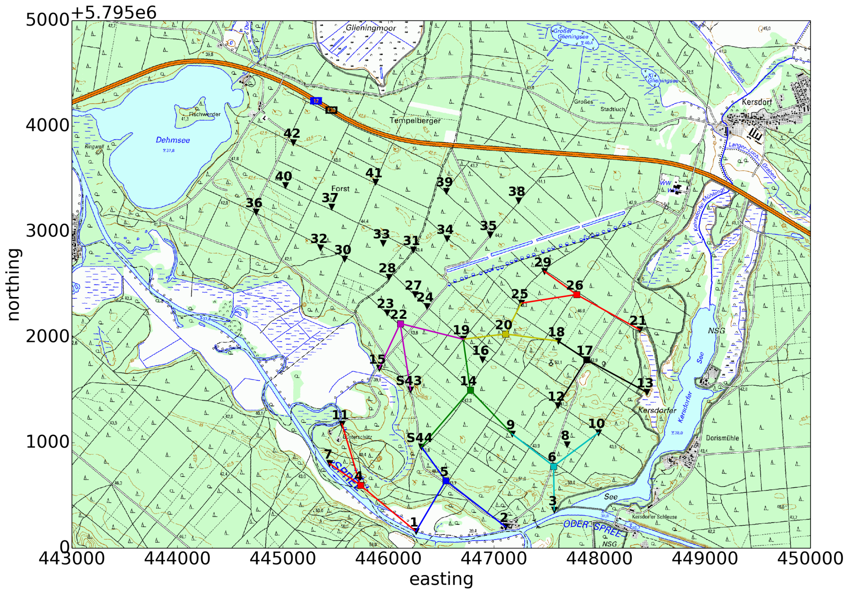

(b)

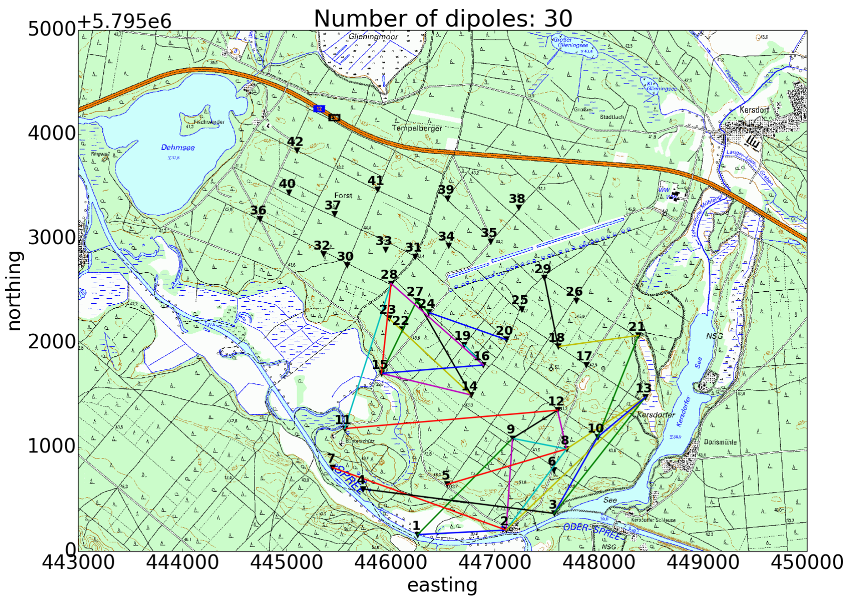

Figure 6.1: Layout for potential dipoles (a) and corresponding current dipoles (b) for the first survey. Two surface electrodes were used, which are marked with S.

(a)

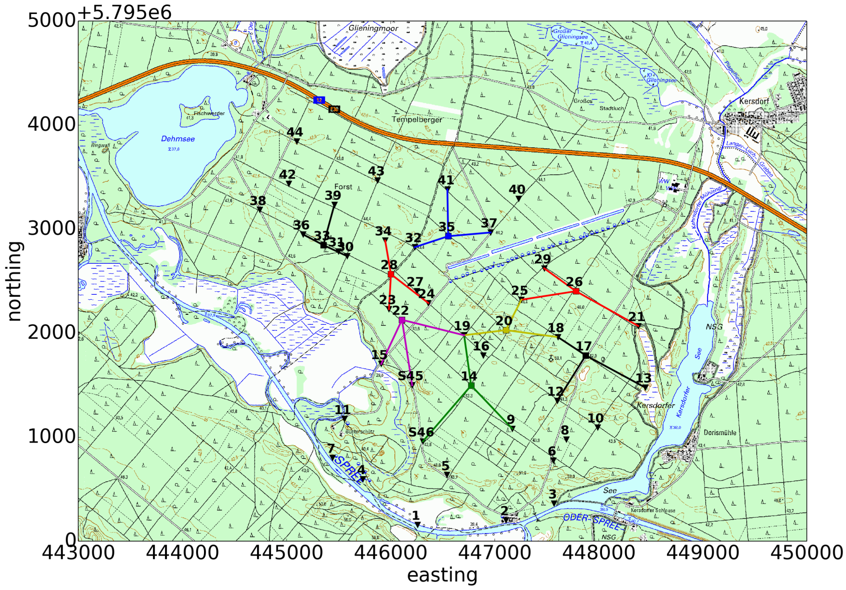

(b)

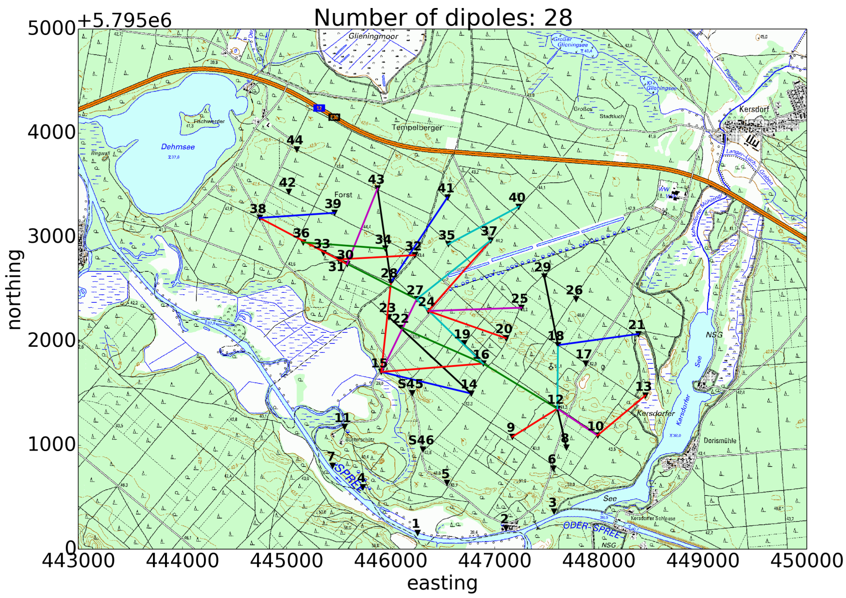

Figure 6.2: Layout for potential dipoles (a) and corresponding current dipoles (b) for the second survey (surface electrodes are marked with S).

6.3 Field measurements

6.3.1 Data logger and current source

Three-channel data loggers developed and optimised for large-scaled test sites and monitoring purposes were used for data acquisition. Figure 6.3 shows the interior of the data logger.

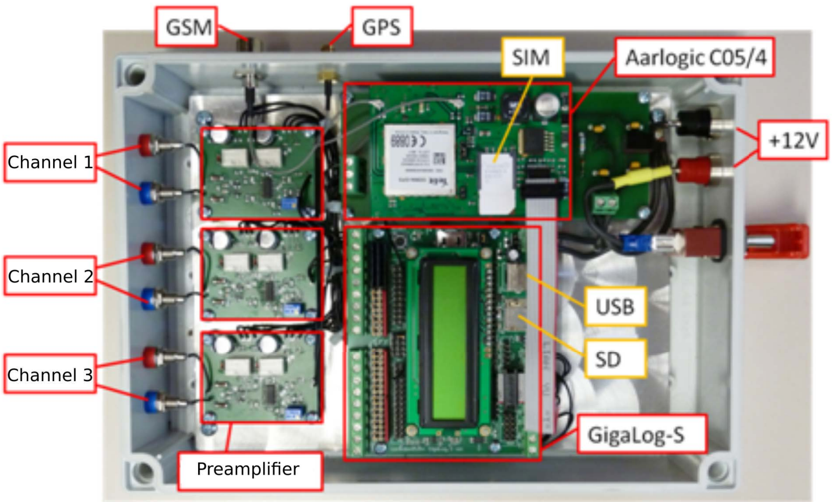

Figure 6.3: Data logger used for signal detection.

All three inputs of the data logger can be amplified by the factors 2, 10, 20 or 100. A sampling frequency between 1 Hz - 1000 Hz can be selected, which is suitable for ERT measurements. Although they are called DC (direct current) measurements, a low signal frequency is used to avoid polarisation effects at the electrodes. For downloading the recorded signals a USB port can be used. In addition GPRS is available to read small amounts of data ‘on the fly ’on or check the power status. This has proved to be very useful for quality control during the measurement, in order to adjust the amplifier if some signals near the current transmission are overdriven. A power saving mode is implemented that automatically shuts down the data logger during the night. A wake-up time can be programmed such that the data logger terminates the power saving mode to be ready for a measurement that allows the user to leave the data logger in the field for the whole survey. Time is synchronised by means of GPS sensors to ensure an equal time basis for every data logger.
For current transmission, a high current source developed by IE-Power was used, shown together with the power supply in Figure 6.4. A special modification, demanded for scientific applications, enables a freely programmable shape of the current function with frequencies up to 100 Hz. The current source is controlled

(a)

(b)

Figure 6.4: High current source used for current transmission (a) and the corresponding power supply (b).

via a laptop. A LabView program is used to set the parameters for the current transmission like the period, amplitude or width of the zero-amplitude range. The latter is needed for hardware reasons when switching from positive to negative amplitudes. The current signal with the corresponding GPS time is recorded for the whole transmission. A maximum power output of 40 kW with a maximum current of ±50 A or voltage of ±1500 V can be realised.
For this survey, a signal with 90 % duty cycle and a maximum amplitude of 15 A was used with a frequency of $\frac{1}{5}$ Hz.

6.3.2 Lock-In approach for estimating amplitudes of noise corrupted time-series

The current signal and voltages are recorded as time-series. For estimating the amplitude of a noise corrupted time-series a phase sensitive method known as the Lock-In approach is used, which has proven to be a stable approach that leads to reliable results. The advantage is that signals with frequencies different from the transmitted one can be filtered effectively. The procedure is shown schematically in Figure 6.5 for a synthetic rectangular shaped signal. Generally, the Lock-In approach rectifies the signal by flipping negative into positive parts. A synthetic mask signal is needed, which can be either gripped at a reference input or it can be calculated, because the transmitted signal is usually well known.
The mask signal M(t) is assigned with the amplitudes 1, 0 and -1. In this case, it has the shape of a rectangular transmission signal. The recorded signal U(t) (the red curve in Figure 6.5a) is convolved with the mask signal M(t) (blue curve in Figure 6.5a) for all possible phases. The resulting normalised

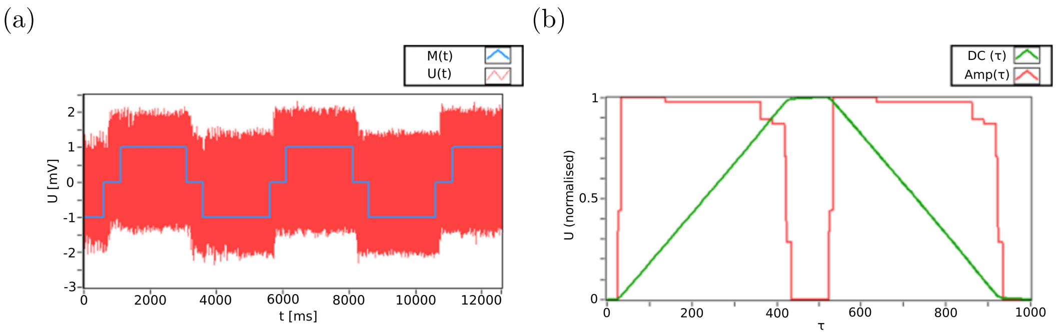

Figure 6.5: Lock-In principle for estimating the amplitude of a time-series. The red curve in (a) shows the noisy time-series U(t) with the blue synthetic mask signal M(t). The result of the convolution between U(t) and M(t) is shown in (b).

amplitude function Amp(τ) and DC-function DC(τ) are shown in Figure 6.5b. Synchronous phases of U(t) and M(t) corresponds to a rectification of the positive and negative half-wave of the signal. The maximum accordance between U(t) and M(t) is reached at the operating point, where DC(τ) = 1 and Amp(τ) = 0 which is used to determine the amplitude of U(t). Due to IP effects at the long electrodes, peaks can appear, where the signal amplitude switches from positive to negative and vice versa. This can make it difficult to determine the operating point.

6.4 3D LE-ERT results

The first survey conducted in August 2013 focused on the southern part of the test-site, while the second one conducted in May 2014 was shifted in the north-west direction relative to the first. A time span of two weeks for the first and one week for the second survey was scheduled, which includes the installation and measurement. Fast progress during both surveys meant that the data base could be extended by a few additional current transmissions. As shown in Figure 6.2, a set of equal dipole combinations in the centre of the test-site was planed for comparison purposes between both surveys. The dipoles used for current transmission of survey one and two are given in Figure 6.2a and Figure 6.2c. 2D ERT profiles were not scheduled as additional data sets due to several reasons. First, metallic fences parallel to almost every path would have led to artefacts in the resistivity distribution. Secondly, the available equipment for measuring 2D ERT profiles allows a maximal electrode spacing of 5 m with about 100 electrodes. The resulting investigation depth is not sufficient for comparison purposes with the LE-ERT surveys.

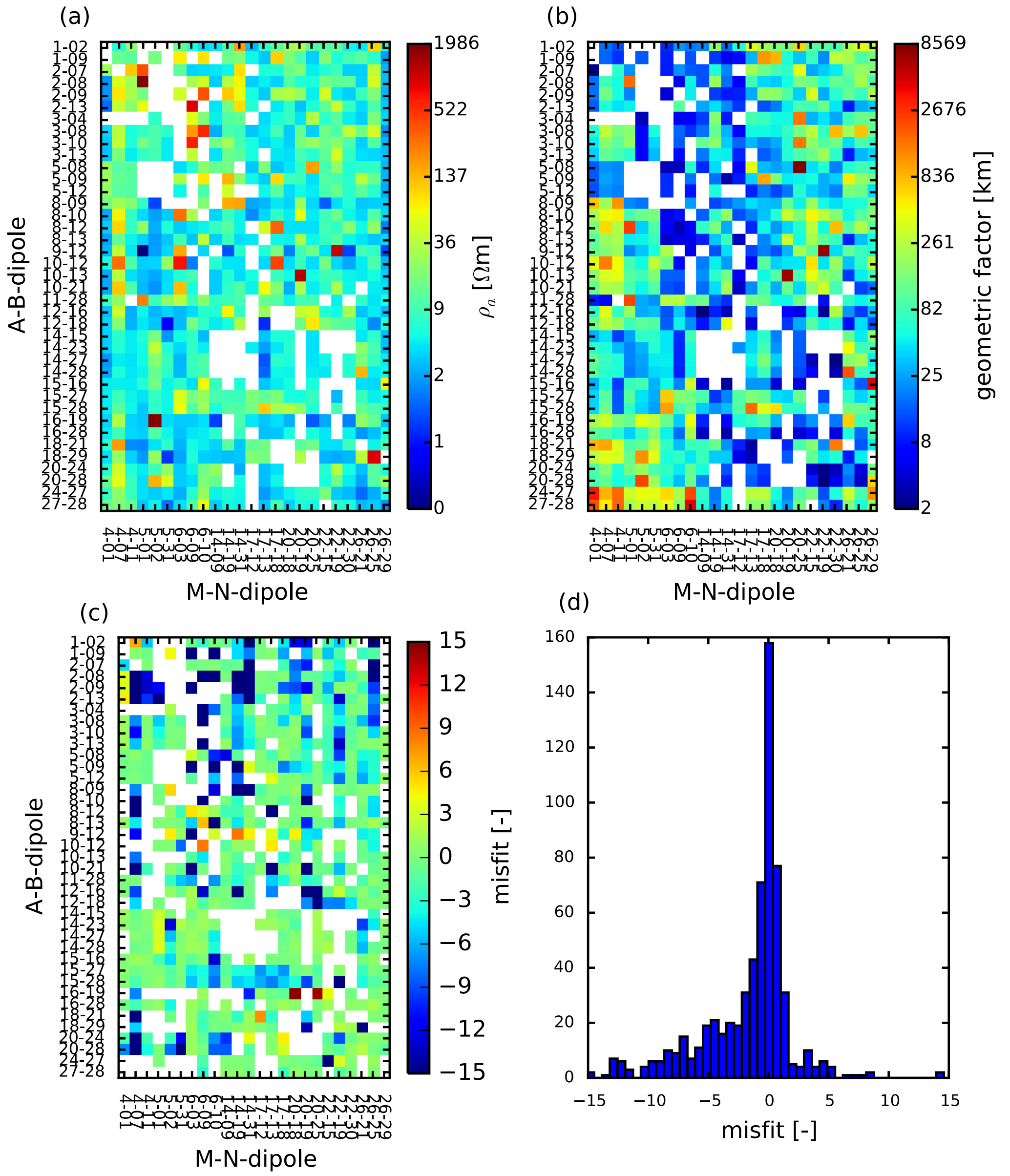

Figure 6.6: Matrix plot of (a) apparent resistivities and (b) geometric factors of the first survey with electrode numbers forming current- and potential-dipoles as axes labels. Misfit distributions of the data fit are given in (c) and (d).

After processing the time series, a total amount of about 837 data points for the first and 718 for the second survey could be used as an input for further filter processes. An error model was assumed with a constant level of 4% and an additional voltage error of 0.1 mV. Geometric factors were calculated numerically on fine tetrahedral meshes using CEM (see section 3.2) to approximate boreholes as long electrodes. Prior to inversion, filters were applied that discard data points with geometric factors $|K| \geq 5000\,\mathrm{km}$ and/or errors exceeding 20% using the described error model. A total amount of approximately 680 data points for the first and 600 data points for the second survey were used for inversion. The apparent resistivities and geometric factors are shown as matrix plots in Figure 6.6. The electrode numbering corresponds to those given in Figure 6.2a and Figure 6.2c. Single measurements that appear in the raw data plot (Figure 6.6a) but not in the misfit distribution in Figure 6.6c were deleted prior to inversion by the applied filters described above.

According to Figure 6.6a, most of the estimated apparent resistivities are below $\sim 35\,\Omega\mathrm{m}$. Just a few outliers occur with ρ_a values above $1000\,\Omega\mathrm{m}$ or below $1\,\Omega\mathrm{m}$. Exceptionally high ρ_a values about $2000\,\Omega\mathrm{m}$ appear for combinations with the potential electrode 5, which is a subsurface point electrode in 15 m depth. The corresponding combinations are 2-8-5-1 and 16-19-5-2 for high ρ_a values and 9-12-5-1 for a low ρ_a value, using the scheme A-B-M-N. Cable or connection issues would appear as a row or column of high or low resistivities, because all current transmissions or potential measurements with a disconnected electrode were affected.

The error weighted misfits in Figure 6.6c and Figure 6.6d show that most data could be fitted well. The potential dipole 4-7 located directly in the vicinity of the Spree river shows higher misfits for most current dipoles. As not all combinations for this potential dipole exhibit large misfits, an unfavourable dipole arrangement is most likely responsible for this. In the misfit distribution, no systematic errors, which may arise due to discretisation errors or uncertainties of electrode positions or lengths, can be noticed for further dipole combinations. Figure 6.6b shows that only a few measurements possess exceptionally high geometric factors (K) like combination 9-12-22-19 or 10-13-20-19 (after the scheme A-B-M-N), which might indicate instable measurements that exhibit low voltages.

The finite element meshes used for data inversion consist of prism elements. Long electrodes were incorporated with the SEM, because of the lesser numerical effort, and additional surface electrodes as nodes. The parameter domain for the first survey was extended to $6.0 \times 5.5 \times 0.5\,\mathrm{km}$ with about 33700 cells. The second survey was slightly larger with a parameter domain consisting of about 38200 cells and an extension of $7.4 \times 6.2 \times 0.5$ km. The regularisation factor was set to $\lambda = 1$ for the inversion of both data sets, in order to reach $\chi^2 = 1$ for the data fit. The result of the first survey is shown in Figure 6.7.

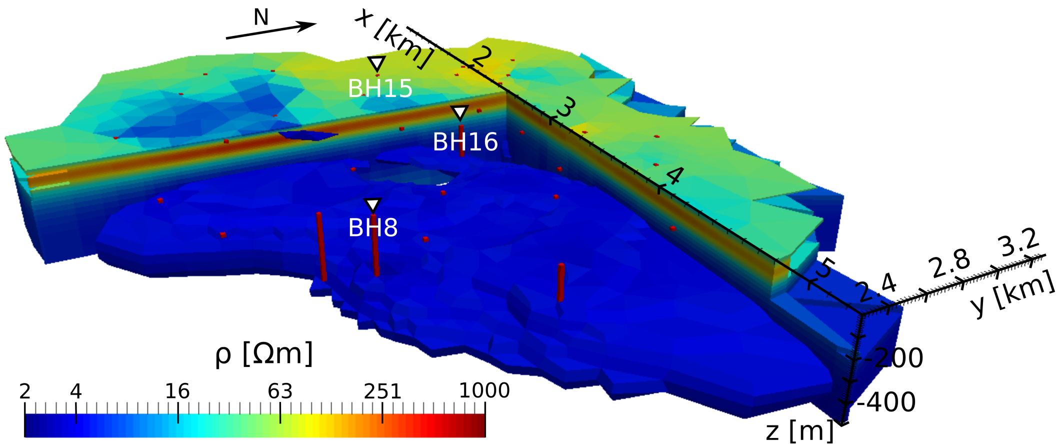

Figure 6.7: Inversion result of the first survey conducted in 08/2013 with boreholes included as red bodies. The blue extracted surface shows resistivities below 5 Ωm. Used electrodes are marked with red cylinders.

The fitted resistivity distribution shows mainly a two layer case. In the first 200 m, resistivities larger than 100 Ωm appear, followed by a highly conductive zone. A low resistive body follows below with $\rho < 5\,\Omega$m. Although borehole logs are only sparsely available, three representative electro-logs were used for comparison. The standard electro-log is a simple 4-point measurement conducted in an open hole. A small or a large electrode separation is used, whereas the measured resistivity is assigned to the centre of the array. By moving the 4-point array to the bottom of the borehole, a depth profile of the subsurface resistivity is obtained. A special variation of this is the latero-log. Due to a specific arrangement of several current electrodes, the equipotential lines are compressed in the centre of the electrode array to focus the voltage measurement. The resistivity measured by latero-logs is affected least by the well fluid. The latero- and electro-log of the boreholes BH16, BH15 and BH8 are shown in Figure 6.8 together with the vertical resistivity distribution extracted from the LE-ERT result at the borehole positions. All logs shown were measured in 1986/87 with a depth resolution of 5 cm. Depending on the length of the conductor pipe, the logs start at different depth levels.

The latero- and electro-logs are almost identical, except for BH15 in Figure 6.8b, in which both logs show differences at depths from 15 m to 70 m and from 200 m to 300 m. The sensitivity of the latero-log reaches deeper into the undisturbed

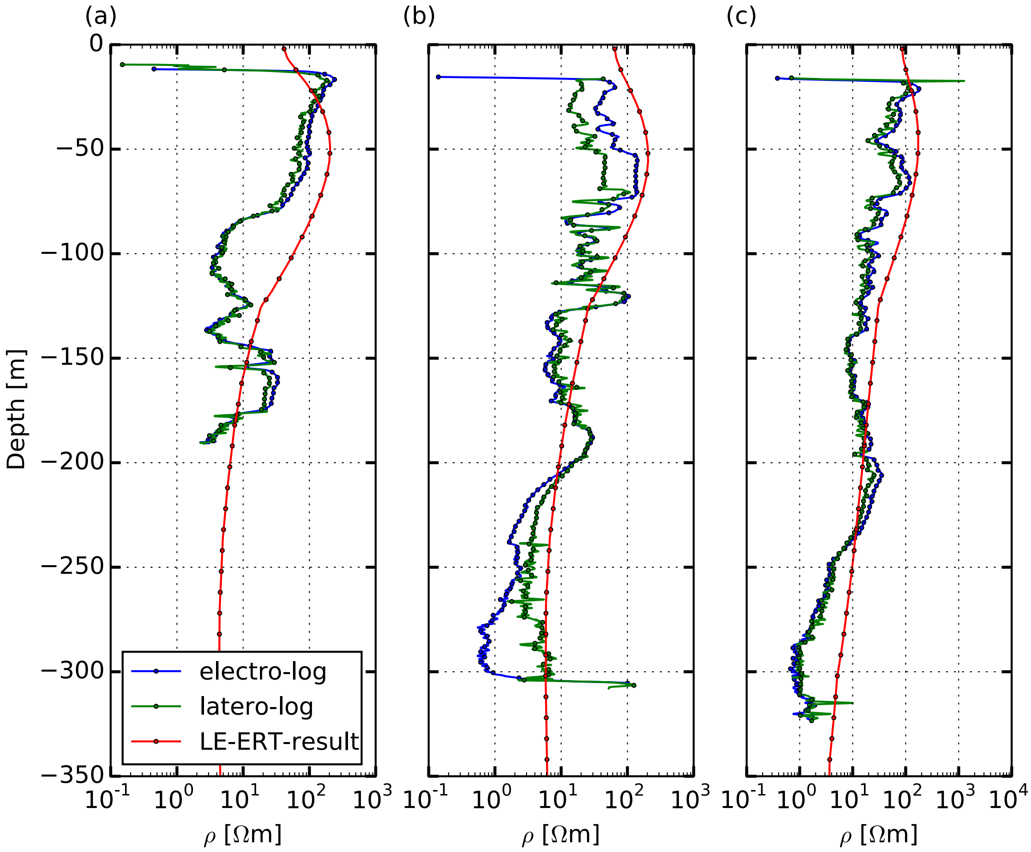

Figure 6.8: Latero-Logs and the corresponding vertical resistivity distribution for (a) BH16, (b) BH15 and (c) BH8.

formation than the electro-log. A reason for the difference could be a larger hole caliper due to collapses of the borehole wall during drilling. This leads to a larger disturbed zone around the borehole and influences measurements with a shallow penetrations depth.
However, the general trend of the electro- and latero-log is reproduced by LE-ERT for all three boreholes. Small-scaled resistivity variations of the logs cannot be resolved. Higher resistivities at about 50 m depth are overestimated by LE-ERT. The decreasing resistivity with increasing depth could be validated in all logs. Even the differently pronounced resistivity decrease is reproduced by LE-ERT. For example the logs at BH16 show a sharper slope than at BH8, which appears also in the LE-ERT results.

The raw data, geometric factors and the misfit between measured data and forward response of the inversion result for the second survey is shown in Figure 6.9.
Most of the estimated apparent resistivities shown are below 20 Ωm, which is a slightly lower level compared to the first survey. Just one outlier with very large ρ_a values appears with a maximum of about 22000 Ωm, which does not correspond to large geometric factors. Higher misfits appear for a few dipole combinations. Almost all combinations with the potential dipole 14-07 exhibit larger misfits. According to the histogram in Figure 6.9d, most of the misfits are below 5%.
The inversion result of the second survey in Figure 6.10 shows the same overall resistivity distribution than the first survey. At the first few meters the inversion result shows a structured zone with high and low resistivities. Down to approximately 100 m depth, resistivities larger than 125 Ωm occur. They decrease to $\rho \approx 25\,\Omega$m for depths larger than 200 m, with a low resistive zone of $\rho < 8\,\Omega$m. Slight ρ variations appear in the conductive zone (below 200 m), which is illustrated by the blue body in Figure 6.10 showing resistivities lower than 5 Ωm. The comparison with electro- and latero-logs for three boreholes is shown in Figure 6.11.
The decreasing resistivities with increasing depth of the LE-ERT result are confirmed by the borehole logs. The resistivities for depth down to 100 m are higher compared to the first survey. As a result, LE-ERT overestimates the resistivities compared to the borehole logs. The purpose of the second survey was to extend the first one in order to cover the whole area. It was designed such that some dipole combinations (A-B-M-N) are identical to the first one, allowing a comparison between both data sets.

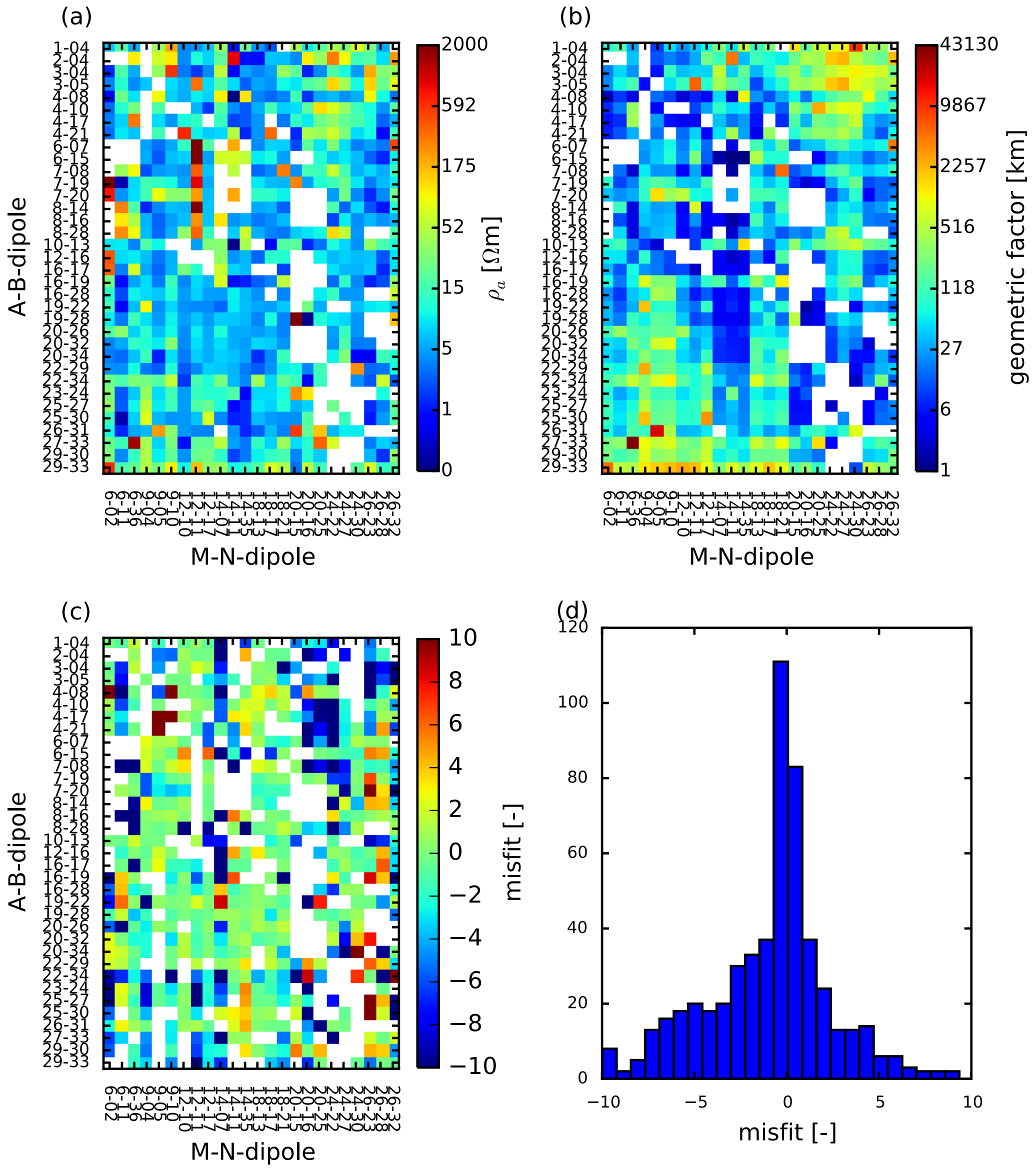

Figure 6.9: Matrix plot of (a) apparent resistivities and (b) geometric factors of the second survey, with electrode numbers forming current- and potential-dipole as axes labels.

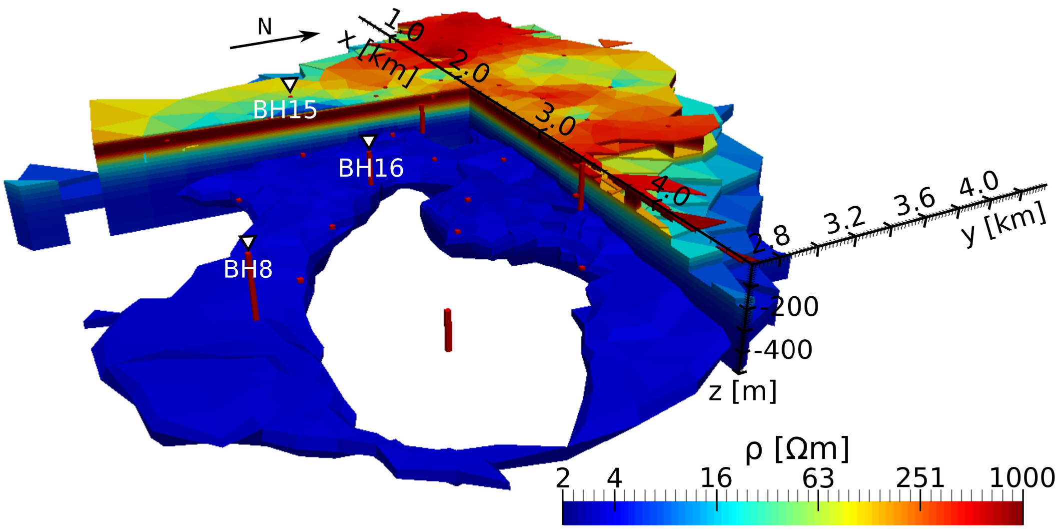

Figure 6.10: Inversion result of the second survey conducted in 05/2014 with boreholes included as red bodies. The blue coloured extracted surface shows resistivities below 5 Ωm.

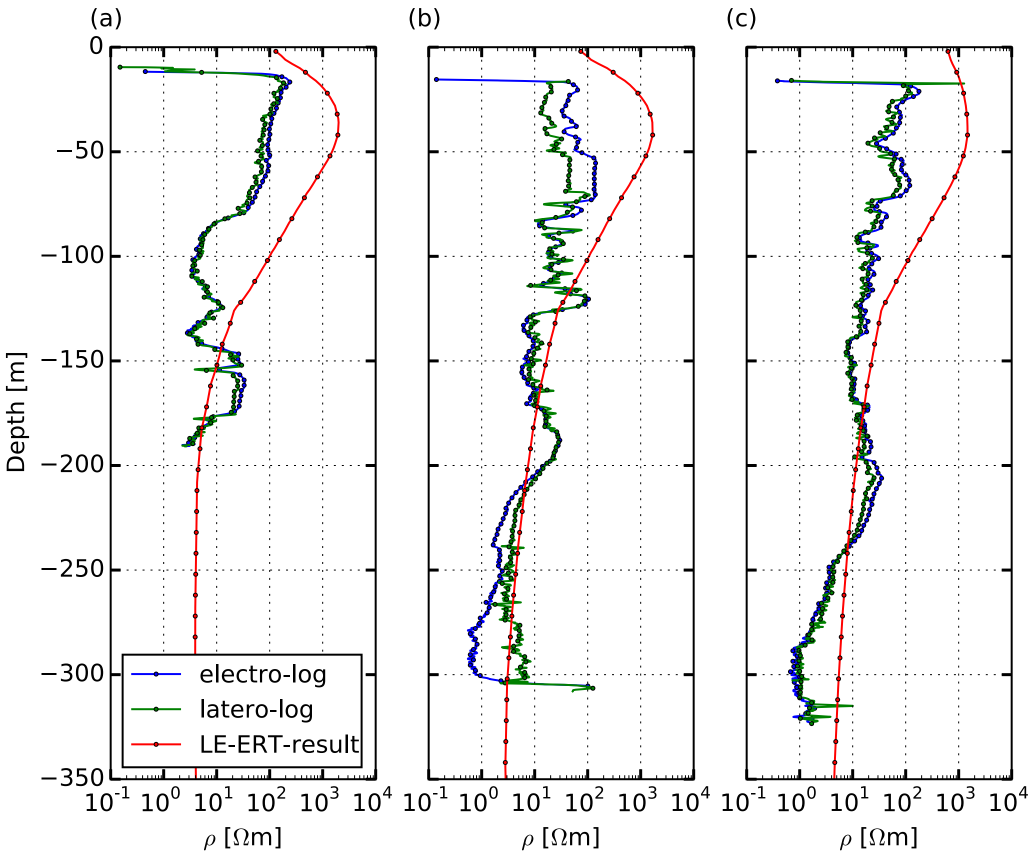

Figure 6.11: Latero-Logs and the corresponding vertical resistivity distribution of the LE-ERT result from the second survey for (a) BH16, (b) BH15 and (c) BH8.

6.4.1 Comparison and combination of the first and second survey

By combining both data sets, the catchment area of the water works at this test site can be covered. Approximately one year lies between the two data sets. As the sensitivities of LE-ERT measurements is shifted into larger depth, it can be assumed that the resistivities of both data sets are not influenced by seasonal variations. If no significant changes of electrical fluid conductivities occur, both surveys should provide more or less the same data. The ratio between apparent resistivities for both surveys was calculated for identical dipole combinations in order to investigate the reproducibility. The resistivity ratio of these combinations is shown in Figure 6.12.

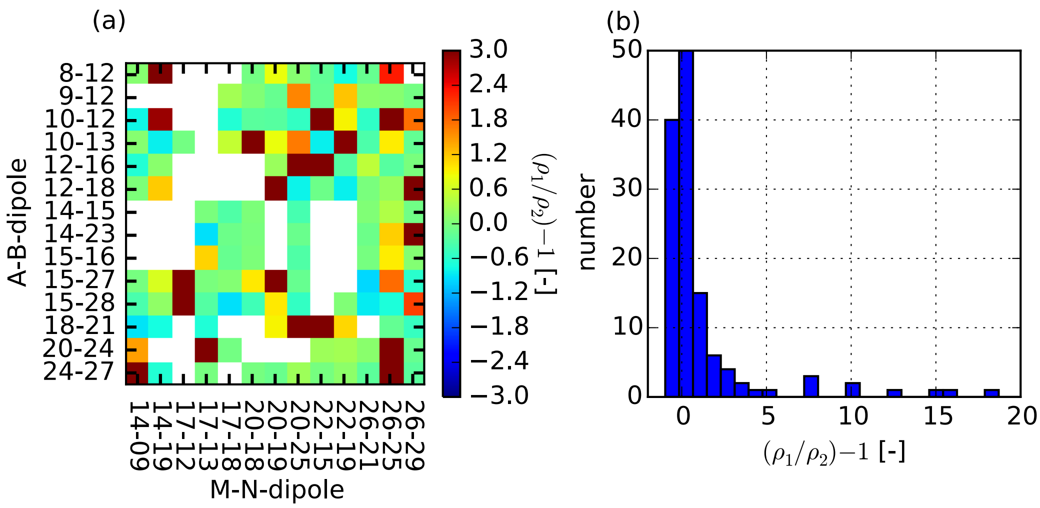

Figure 6.12: Matrix plot (a) and histogram (b) of the ρ_a ratio of equal dipole combinations for the first and second survey.

The matrix plot shows that a few combinations are almost equal. The histogram in Figure 6.12b shows that approximately 90 of 130 data points have a ratio of about 1. A few combinations show exceptionally large ratios. The reason for this is not yet clear. The combined data-set consists of 1500 data points measured with 46 electrodes. An error model of 4% and a voltage error of 10 μV was assumed for the data set. Filter were applied that discard combinations with a geometric factor exceeding $\pm$ 5000 km or an error above 20%.

A finite element mesh was used with prism elements. The lateral extension of the parameter domain was set to 7.4 km in x- and y-direction with a depth of 500 m leading to approximately 43700 cells. The regularisation parameter was set to $\lambda = 1$. As a layered subsurface could be assumed according to borehole information, a vertical weighting of 0.25 was used. To fit the data within their errors the L_1-norm (see section 2.4) was used. The result of the smoothness-constrained inversion is shown in Figure 6.13.

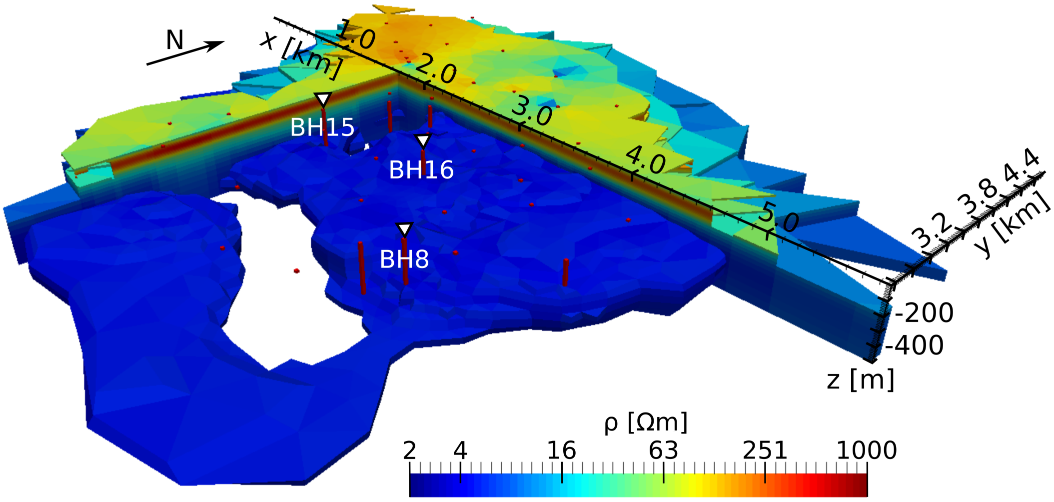

Figure 6.13: Inversion result for combined data-set with clips in E-W and N-S direction with a low-resistive body of $\rho \leq 5\,\Omega$m.

The overall resistivity distribution derived from the combined data set is similar to the inversion results of the single surveys. Along the N-S slice it can be seen that the resistivities in the highly resistive zone at about 100 m depth decrease from south to north. The resistivities below 200 m depth does not exceed 10 Ωm and show slight lateral variations. The blue body shows only resistivities lower than 5 Ωm. It is interrupted in the middle part with slightly higher resistivities. The reason for this can not be clearly identified, but possible explanations could be a low data coverage or changing fluid conductivities. The last possibility cannot be confirmed due to missing boreholes at this part. The comparison of the LE-ERT result of the combined data set with latero- and electro-logs of three boreholes is shown in Figure 6.14.

As expected, the comparison between the borehole logs and the LE-ERT result at corresponding positions is equal to that of the separated inversion. The general trend of decreasing resistivities with increasing depth is reproduced by LE-ERT, but not small scale variations. Nonetheless, Figures 6.13 and 6.14 confirm that the combined data set and the separated inversion of both surveys lead to similar results.

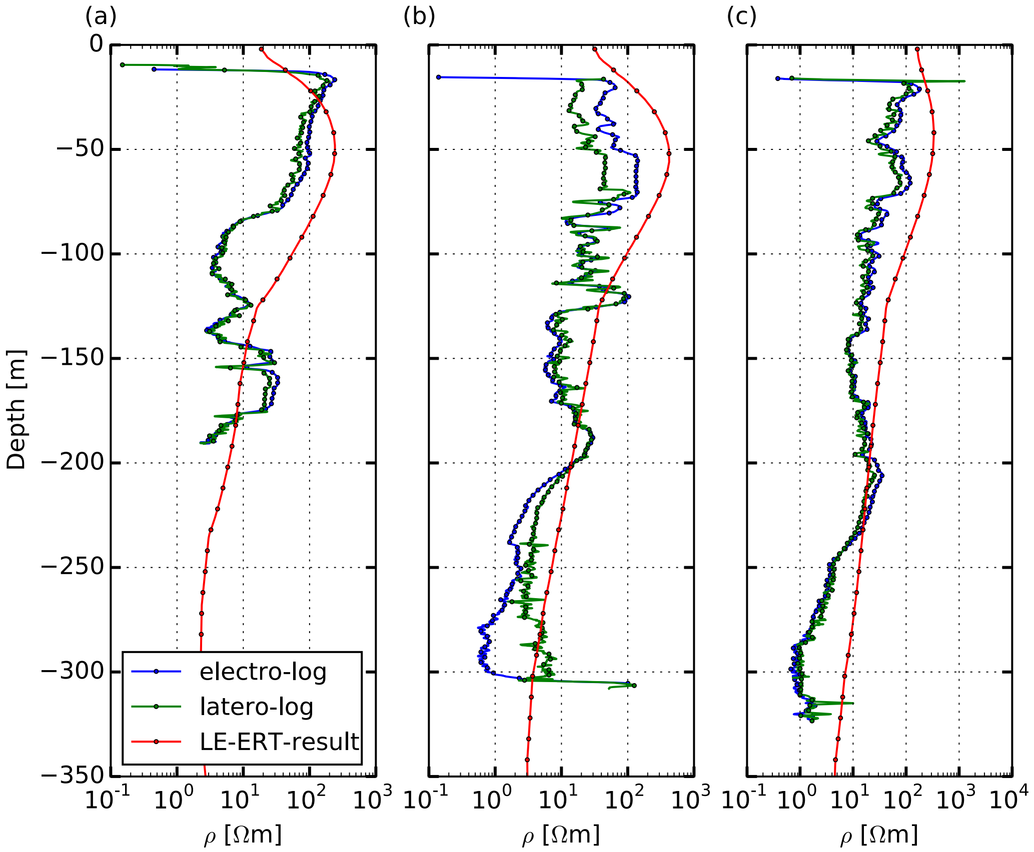

Figure 6.14: Latero- and electro-logs for (a) BH16, (b) BH15 and (c) BH8 with the corresponding vertical resistivity distribution of the LE-ERT result from the combined surveys.

6.5 Conclusion

The data optimisation algorithm was successfully adapted to the special circumstances that had to be taken into account for LE-ERT measurements at large scale sites, i.e. pre-defined potential dipole layouts. The calculation of about 30 current transmissions for given potential dipoles was an acceptable trade-off between loss of information content and necessary effort for conducting both surveys at the test site Briesen. It could be shown that an experienced team can conduct a survey with about 30 current transmissions and 24 potential dipoles within one week. The Lock-In approach was used for estimating amplitudes of noise corrupted time series, which provides stable and reliable results. Nonetheless, peaks within the time series and low frequency effects makes it difficult to estimate correct amplitudes. Only a semi automated time series processing could be applied on the raw data. Peaks at the beginning and the end of the transmitted rectangular and low frequency variations within some time series demanded extra processing efforts.
Due to the current transmission and measurement by long electrodes, the shallow unsaturated, highly resistive zone down to a depth of a few metres has no significant influence on the data. Another positive aspect is the good coupling of long electrodes, which enables high current strengths. The SEM reduced the numerical effort compared to the CEM by approximating the electrode shape with nodes. Inversion results image a quite smooth resistivity distribution that resolves only the general trend, which results from the relatively low amount of data for this survey size. The comparison of latero- and electro-logs from three representative boreholes with LE-ERT inversion results validated the reproducibility of the general resistivity trend. Small scaled resistivity variations could not be imaged. The combination of both survey leads to a data set that covers a large area of several km^2. The comparison with the same borehole logs showed similar results than the separated data sets. It could be shown that LE-ERT measurements on a scale of some square kilometres is possible and leads to results, which are in good agreement with reference data.

7 Summary and conclusion

Summary

Extensive numerical simulations, laboratory measurements and field surveys were conducted to investigate the possibility of using metal casings of boreholes as long electrodes for ERT surveys in order to image and monitor inland saltwater intrusions.
At first synthetic studies were done to compare different approaches for incorporating long electrodes in FEM meshes. Three methods were tested and compared on simple benchmark models. Investigations on the accuracy were made to evaluate how fine long electrodes have to be discretised to prevent numerical errors. Investigations concerning the model resolution of long electrode ERT (LE-ERT) measurements were made. This includes the comparison of sensitivity distributions for different electrode combinations and the calculation of resolution radii distributions for synthetic cases. The effect of vertically or horizontally moving low resistive intrusion fronts on four point measurements with different dipole lengths, radial, equatorial and shifted (mix of radial and equatorial) dipoles was modelled. Finally, a simple two layer case with a conductive anomaly was modelled using point electrodes, long electrodes of equal length and long electrodes of different length. Synthetic data were generated, inverted and the results compared.

Secondly, 2D and 3D laboratory experiments simulating several saltwater intrusion scenarios were conducted. A vertical slice of a coastal region was simulated to observe the movement of the typical saltwater wedge by alternating the freshwater recharge rate or inundating the model with saltwater. The ERT monitoring was conducted with a 2D profile that used surface and underwater point electrodes. The second experiment was installed in a tank using a regular grid of 4×3 electrodes of 20 cm length that enabled the imaging of a 3D resistivity distribution. Horizontal movement of a saltwater front was monitored using a data set that was optimised to obtain a maximum information content with the smallest possible number of dipole combinations. Different inversion

approaches were applied to the time lapse data set and the inversion results were compared to find the most reasonable model with the best data fit.

Finally, field surveys were designed for two test sites of medium and large scale. Monitoring measurements were scheduled for the first test site with a size of 500×400 m. Comparisons of LE-ERT measurements with ERT profiles and water samples taken at several groundwater wells were made to appraise the quality of the new approach. A decentralised set-up was tested in the first field measurement and replaced with a centralised complete cabling that enables fast and cost efficient monitoring measurements. A set of dipole combinations was generated that optimises the information content using the smallest possible amount of current transmissions to reduce the effort for one survey. Two LE-ERT surveys were conducted with a temporal separation of about one year. Both data sets could be combined to cover an area of 7×7 km.

Conclusions

Three models exist, which are capable of simulating long electrodes. The complete electrode model (CEM) and conductive cell model (CCM) lead to the same results, due to a similar discretisation. As CEM represents the physical reality best, it is recommended for calculations that demand high accuracy like the numerical estimation of geometric factors for long electrode measurements. The main advantage of the shunt electrode model (SEM) lies in the significantly reduced numerical effort, which leads to FEM meshes with a comparatively small number of cells. When performing LE-ERT surveys, the low amount of electrodes and the large spacing in between leads to a lower model resolution, which is considered by a coarse discretisation. Consequently, it enables conducting inversions on common computers. Nevertheless, simulations showed that a mesh refinement with quadratic shape functions is always needed. In the case of CEM, the electrode diameter is of special interest. Real borehole diameters cannot be used for FEM meshes, because a large number of elements are needed for discretising thin electrodes. It can be shown that the diameter of long electrodes should not be larger than 1% of the electrode spacing in order to keep the numerical errors below 1%. Thus, if CEM was used for calculating geometric factors, the smallest possible borehole diameter was used to avoid numerical errors.
Simulations showed that varying contact impedance along electrodes could affect the potential field significantly. Nonetheless, large variations of several orders of magnitude lead to deviations that rarely exceed 5 %. As it is very

difficult to estimate a varying contact impedance along an electrode and their impact is of minor importance, it was considered constant for every electrode using a standard value of about 1e-5 Ωm^2.
Simulations confirmed that the vertical resolution in the depth range of the electrode length almost vanishes, if electrodes of equal lengths are used. If resistivity changes within the depth range of the electrodes can be assumed, it is recommended to add surface electrodes or to use electrodes of different length in order to regain a significant part of the vertical resolution.
Simulations of simple resistivity distributions showed that the larger penetration depth of LE-ERT compared to surface point electrode measurements is only given for small dipole distances. The larger the dipole length and distances between dipoles, the more similar are the results of point and long electrodes.
Inversion of synthetic data showed that meshes consisting of vertically oriented triangular prisms are recommended due to an easier application of vertical constraints and a reduced numerical effort. In conjunction with SEM, the degree of freedom is reduced in inversion and additionally it enables model resolution analysis.

Instable measurements, for example with a potential dipole perpendicular to the current dipole possess a high data importance. While calculating optimised data sets to obtain a large information content these combinations have to be considered seriously in the optimisation process. Due to a very low voltage, the resulting high error level prevents recording those signals. Either these measurements are excluded from the comprehensive data set or error weighted sensitivities are used to calculate data importances.
To fit the time lapse data of the 3D laboratory experiment the difference-inversion scheme to suppress systematic errors, a χ^2-optimised λ_t and the first time step as a base-line gave best inversion results. Regardless of the data set, using the difference inversion to eliminate systematic errors caused by imprecise electrode positions or discretisation errors is always worth a consideration, especially for small electrode layouts with an electrode spacing of a few centimetres (for example laboratory experiments).

LE-ERT measurements have a low resolution at the surface due to the small number of electrodes and general resolution losses due to the long vertical electrodes. If only deeper targets are of focus, this is of minor importance.
The feasibility of LE-ERT for monitoring saltwater intrusions could be shown on the medium scale test site Müllrose. For a survey size of about $500 \times 500\,\text{m}$,

a complete cabling is possible and recommended, as it speeds up the time lapse measurements significantly.
The monitoring results of the test site Müllrose match remarkably well to measured water conductivity data, validating that even small resistivity changes could be resolved. Time lapse inversions show that a well determined base-line is very important for the quality of the results.
The large-scaled application of LE-ERT was shown at the test site Briesen. Only a decentralised set-up could be used due to the lateral extent of several square kilometres. An enormous material effort of more than 20 km cable was necessary. The comparison of LE-ERT results with electric borehole logs of three representative boreholes showed that the general resistivity trend can be imaged, while small scaled resistivity variations are not resolvable. The combination of both surveys conducted at Briesen covered an area of about 7×7 km, which is comparable to the catchment area of the water works at the site.
LE-ERT gives an interesting geophysical alternative to image resistivity distributions on medium- and large-scaled test sites down to about 600 m depth. It has been shown that single measurements as well as monitoring lead to reasonable results. Due to the small amount of electrodes used, a lower vertical and horizontal resolution appears for LE-ERT surveys compared to 2D ERT profiles. Nonetheless, the surveys could sufficiently resolve the targets.

Outlook

Several aspects of LE-ERT need further investigation. For example, improvements of the array optimisation algorithm can be reached by using a resistivity distribution that represents the test site conditions rather than a homogeneous half space. Further investigations for layouts using different combinations with long electrodes have to be done, taking into account that sometimes only a few metal cased boreholes are available. The position of additional surface electrodes could be optimised as well.
Regarding inversion, LE-ERT results showed structured resistivity distribution for the near surface zone. An increased regularisation strength only for shallow model parts could take the lower model resolution properties due to a large electrode spacing into account.
So far, the influence of the length and inclination of boreholes on the geometric factor was not taken into account. A study to estimate systematic errors Beside the DC part of the signal, the IP part could be analysed as well to estimate additional parameters that enable a more accurate distinction of lithologic

units or pore fluid properties. EM signals could be transmitted and used for a joint interpretation or inversion. That could lead to a better characterisation of deep anomalies due to the large investigation depth. No monitoring concepts regarding field set ups exist for the large-scaled application of LE-ERT because of the enormous material effort required. The partitioning into several smaller surveys located in areas of special interest could be a possible alternative.
Finally, completely new applications of the long electrode approach are possible. For example by conducting a vertical electrical profiling by using the drilling equipment as a long electrode and surface electrodes for the potential measurement. By replacing point electrodes of common 2D ERT monitoring profiles with long metal-rods possible seasonal effects that might affect the resistivity distributions could be reduced.

References

Archie, G. E., 1942, The electrical resistivity log as an aid in determining some reservoir characteristics: Trans. Am. Inst. Min., Met & Petr. Eng., **146**, 54–62.

Aster, R. C., B. Borchers, and C. Thurber, 2005, Parameter Estimation and Inverse Problems: Elsevier Academic Press. International geophysics series.

Cheng, K.-S., D. Isaacson, J. Newell, and D. Gisser, 1989, Electrode models for electric current computed tomography: Biomedical Engineering, IEEE Transactions on, **36**, 918–924.

Coggon, J. H., 1971, Electromagnetic and electrical modeling by the Finite Element Method: Geophysics, **36**, 132–155.

Coscia, I., S. Greenhalgh, N. Linde, J. Doetsch, L. Marescot, T. Günther, and A. Green, 2011, 3D crosshole apparent resistivity static inversion and monitoring of a coupled river-aquifer system: Geophysics, **76**, G49–59.

Daily, W., A. Ramirez, R. Newmark, and K. Masica, 2004, Low-cost reservoir tomographs of electrical resistivity: The Leading Edge, **23**, 472–480.

Dey, A., and H. Morrison, 1979, Resistivity modeling for arbitrarily shaped three-dimensional structures: Geophysics, **44**, 753–780.

Doetsch, J., N. Linde, M. Pessognelli, A. Green, and T. Günther, 2012, Constraining 3-D electrical resistance tomography with GPR reflection data for improved aquifer characterization: Journal of Applied Geophysics, **78**, 68 – 76.

Friedel, S., 2000, Über die Abbildungseigenschaften der geoelektrischen Impedanztomographie unter Berücksichtigung von endlicher Anzahl und endlicher Genauigkeit der Meßdaten: PhD thesis, Universität Leipzig.

———, 2003, Resolution, stability and efficiency of resistivity tomography estimated from a generalized inverse approach: Geophysical Journal International, **153**, 305–316.

Günther, T., 2004, Inversion Methods and Resolution Analysis for the 2D/3D Reconstruction of Resistivity Structures from DC Measurements: PhD thesis, TU Bergakademie Freiberg.

Günther, T., and C. Rücker, 2006, A general approach for introducing information into inversion and examples from dc resistivity inversion: Presented at the Ext. Abstract, EAGE Near Surface Geophysics Workshop. 4.-6.9.06, Helsinki(Finland).

Günther, T., C. Rücker, and K. Spitzer, 2006, Three-dimensional modeling and inversion of dc resistivity data incorporating topography – Part II: Inversion: Geophysical Journal International, **166**, 506–517.

Hotzan, G., and T. Voss, 2013, Komplexe hydrogeochemisch-genetische Kartierung zur Einschätzung der Salzwassergefährdung pleistozäner und tertiärer Grundwasserleiter im Raum Storkow-Frankfurt (Oder)-Eisenhüttenstadt: Brandenburg. geowiss. Beitr., **20**, 63–82.

Igel, J., 2007, On the Small-Scale Variability of Electrical Soil Properties and its Influence on Geophysical Measurements: PhD thesis, Johann Wolfgang Goethe University of Frankfurt am Main.

Kemna, A., J. Vanderborght, B. Kulessa, and H. Vereecken, 2002, Imaging and characterisation of subsurface solute transport using electrical resistivity tomography (ERT) and equivalent transport models: Journal of Hydrology, **267**, 125–146.

Kempka, T., R. Herd, E. Huenges, R. Endler, C. Jahnke, S. Janetz, E. Jolie, M. Kühn, F. Magri, P. Meinert, I. Moeck, M. Möller, G. Munoz, O. Ritter, W. Schafrik, C. Schmidt-Hattenberger, E. Tillner, H. J. Voigt, and G. Zimmermann, 2015, Joint Research Project Brine: Carbon Dioxide Storage in Eastern Brandenburg: Implications for Synergetic Geothermal Heat Recovery and Conceptualization of an Early Warning System Against Freshwater Salinization, *in* Advanced Technologies in Earth Sciences: Springer Science + Business Media, 183–208.

Kim, H. J., Y. Song, and K. H. Lee, 1999, Inequality constraint in least-squares inversion of geophysical data: Earth Planets Space, **51**, 255–259.

Kuras, O., J. Pritchard, P. I. Meldrum, J. E. Chambers, P. B. Wilkinson, R. D. Ogilvy, and G. P. Wealthall, 2009, Monitoring hydraulic processes with Automated time-Lapse Electrical Resistivity Tomography (ALERT): Compte Rendus Geosciences - Special issue on Hydrogeophysics, **341**, 868–885.

LaBrecque, D., A. Ramirez, W. D. Daily, A. Binley, and A. Schima, 1996, ERT monitoring of environmental remediation processes: Measurement Science & Technology, **7**, 375–383.

LaBrecque, D., and X. Yang, 2001, Difference Inversion of ERT Data: a Fast Inversion Method for 3-D In Situ Monitoring: Journal of Environmental And Engineering Geophysics, **6**, 83–89.

Lange, G., 2005, Gleichstromgeoelektrik, *in* Handbuch zur Erkundung des Untergrundes von Deponien und Altlasten: Band 3: Geophysik: Springer, 5.3, 128–173.

Loke, M. H., J. E. Chambers, D. F. Rucker, O. Kuras, and P. B. Wilkinson, 2013, Recent developments in the direct-current geoelectrical imaging method: Journal of Applied Geophysics, **95**, 135–156.

Maurer, H., and S. Friedel, 2006, Outer-space sensitivities in geoelectrical tomography: Geophysics, **71**, G93–96.

Menke, W., 1989, Geophysical Data Analysis: Discrete Inverse Theory: Academic Press, inc., volume **45** *of* International Geophysics Series.

Nguyen, F., A. Kemna, A. Antonsson, P. Engesgaard, O. Kuras, R. Ogilvy, J. Gisbert, S. Jorreto, and A. Pulido-Bosch, 2009, Characterization of seawater intrusion using 2D electrical imaging: Near Surface Geophysics, **7**, 377–390.

Ogilvy, R. D., P. I. Meldrum, O. Kuras, P. B. Wilkinson, J. E. Chambers, M. Sen, A. Pulido-Bosch, J. Gisbert, S. Jorreto, I. Frances, and P. Tsourlos, 2009, Automated monitoring of coastal aquifers with electrical resistivity tomography: Near Surface Geophysics, **7**, 367–375.

Pridmore, D. F., G. W. Hohmann, S. H. Ward, and W. R. Sill, 1981, An investigation of finite-element modeling for electrical and electromagnetic data in three dimensions: Geophysics, **46**, 1009–1024.

Radic, T., and A. Weller, 2007, Induzierte Polarisation, *in* Handbuch zur Erkundung des Untergrundes von Deponien und Altlasten: Band 3: Geophysik: Springer, 5.4, 174–214.

Ramirez, A., W. Daily, A. Binley, D. LaBrecque, and D. Roelant, 1996, Detection of Leaks in Underground Storage Tanks Using Electrical Resistance Methods: Journal of Environmental and Engineering Geophysics, **1**, 189–203.

Ramirez, A., R. Newmark, and W. Daily, 2003, Monitoring Carbon Dioxide Floods Using Electrical Resistance Tomography (ERT): Sensitivity Studies: Journal of Environmental and Engineering Geophysics, **8**, 187–208.

Rocroi, J. P., and A. Koulikov, 1985, The use of vertical line sources in electrical prospecting for hydrocarbon: Geophysical Prospecting, **33**, 138–152.

Ronczka, M., C. Rücker, and T. Günther, 2015a, Numerical study of long-electrode electric resistivity tomography - Accuracy, sensitivity and resolution: Geophysics, **80**, E317–E328.

Ronczka, M., T. Voß, and T. Günther, 2015b, Cost-efficient imaging and monitoring of saltwater in a shallow aquifer by using long electrode ERT: Journal of Applied Geophysics, **122**, 202–209.

Rücker, C., and T. Günther, 2011, The simulation of finite ERT electrodes using the complete electrode model: Geophysics, **76**, F227–F238.

Rücker, C., T. Günther, and K. Spitzer, 2006, 3-d modeling and inversion of DC resistivity data incorporating topography - Part I: Modeling: Geophysical Journal International, **166**, 495–505.

Rucker, D. F., 2012, Enhanced resolution for long electrode ERT: Geophysical Journal International, **191**, 101–111.

Rucker, D. F., N. Crook, D. Glaser, and M. H. Loke, 2011a, Pilot-scale field validation of the long electrode electrical resistivity tomography method: Geophysical Prospecting, 1 – 17.

Rucker, D. F., J. B. Fink, and M. H. Loke, 2011b, Environmental monitoring of leaks using time-lapsed long electrode electrical resistivity: Journal of Applied Geophysics, **74**, 242–254.

Rucker, D. F., M. H. Loke, M. T. Levitt, and G. E. Noonan, 2010, Electrical-resistivity characterization of an industrial site using long electrodes: Geophysics, **75**, WA95–WA104.

Schön, J., 2004, Physical Properties of Rocks: Fundamentals and Principles of Petrophysics: Pergamon press.

Seidel, K., and G. Lange, 2007, Direct Current Resistivity Methods, *in* Environmental Geology: Handbook of Field Methods and Case Studies: Springer, 4.3, 205–237.

Shi, L., L. Cui, N. Park, and P. Huyakorn, 2011, Applicability of a sharp-inverface model for estimating steady-state salinity at pumping wells-validation against sand tank experiments: Journal of Contaminant Hydrology, **124**, 35–42.

Si, H., 2002-2008, TetGen - a quality-constrained tetrahedral mesh generator. Weierstrass institute, Berlin, www.tetgen.org.

Slater, L., A. Binley, R. Versteeg, G. Cassiani, R. Birken, and S. Sandberg, 2002, A 3D ERT study of solute transport in a large experimental tank: Journal of Applied Geophysics, **49**.

Slater, L., A. M. Binley, W. Daily, and R. Johnson, 2000, Cross-hole electrical imaging of a controlled saline tracer injection: Journal of Applied Geophysics, **44**, 85–102.

Sommerfeld, A., 1967, Vorlesungen über Theoretische Physik, Band III: Elektrodynamik, 4 ed.: Akademische Verlagsgesellschaft Geest & Portig.

Sulzbacher, H., H. Wiederhold, B. Siemon, M. Grinat, J. Igel, T. Burschil, T. Günther, and K. Hinsby, 2012, Numerical modelling of climate change impacts on freshwater lenses on the North Sea Island of Borkum using hydrological and geophysical methods: Hydrology and Earth System Sciences, **16**, 3621–3643.

Tan, H.-Q., J. Shen, C. Zhou, H. Dong, X. Fang, and F. Zhang, 2004, Borehole-to-surface electrical imaging technique and its application to residual oil distribution analysis of the eighth section in Gudong Oil field: Journal of University of Petroleum, **28(2)**, 31–37.

Ushijima, K., H. Mizunaga, and T. Tanaka, 1999, Reservoir monitoring by a 4-D electrical technique: The Leading Edge, **18**, 1422–1424.

Wang, M., F. Dickin, and R. Mann, 1999, Electrical Resistance Tomographic Sensing System for Industrial Applications: Chem. Eng. Comm., **175**, 49–70.

Waxman, M. H., and L. J. M. Smits, 1986, Electrical conductivities in oil-bearing shaly sands: Trans. Am. Inst. Min., Met & Petr. Eng., **243**, 107–122.

Wenner, F., 1916, A method of measuring earth resistivity: Bulletin of the Bureau of Standards, **12**, 469–478. (Scientific Paper 258).

Werner, A., D. Jakovovic, and C. Simmons, 2009, Experimental observations of saltwater up-coning: Journal of Hydrology, **373**, 230–241.

Wiederhold, H., H. Sulzbacher, M. Grinat, T. Günther, J. Igel, T. Burschil, and B. Siemon, 2013, Hydrogeophysical characterization of freshwater/saltwater systems - case study: Borkum Island, Germany: First Break, **31**.

Xu, B., and M. Noel, 1993, On the completeness of data sets with multielectrode systems for electrical resistivity surveys: Geophysical Prospecting, **72**, F57–F64.

Zhang, J., R. Mackie, and T. Madden, 1995, 3-D resistivity forward modeling and inversion using conjugate gradients: Geophysics, **60**, 1313–1325.

Zhang, Y.-Y., D.-J. Liu, Q.-H. Ai, and M.-J. Qin, 2014, 3D modeling and inversion of the electrical resistivity tomography using steel cased boreholes as long electrodes: Journal of Applied Geophysics, **109**, 292–300.

Zhu, T., and R. Feng, 2010, Resistivity tomography with a vertical line current source and its applications to the evaluation of residual oil saturation: Journal of Applied Geophysics, **73**, 155–163.

Zienkiewicz, O. C., 1977, The Finite Element Method: McGraw-Hill, **3**.

List of Figures

List of Tables

Acknowledgements

While completing this thesis, I was supported by many people, who I want to express my thanks at this point. I also want to apologize in advance to those people and/or institutions that are not mentioned.

The Federal ministry of education and research (BMBF) for the funding of the project (grant 03G0774B) which lead to this thesis.

Prof. Yaramancy for the support of the project at the LIAG and for acting as an examiner of the thesis.

Prof. Binley for reviewing the thesis and acting as an examiner at the defence.

Special thanks to Dr. Günther for his support in the project, the thesis, countless discussions about ERT, modelling and inversion and several other topics that brought my knowledge of modelling and inversion to a whole new level.

I also want to thank the technical team, Wolfgang Südekum, Robert Meyer and Dieter Epping for their most valuable support prior, during and after the conducted field surveys.

The project partner Blm Storkow for their support concerning administrative processes and additional measurements at the test sites.

Thanks to my colleagues Jan Igel, Mike Müller-Petke and Marion Miensopust for reviewing and improving my thesis.

At last, I want to thank my family for their support.